INVESTIGATION OF DYNAMICS OF PARTICULATE TRANSPORT UNDER VARYING CLIMATE CONDITIONS

A thesis submitted to the Committee of Graduate Studies in partial fulfillment of the requirements for the Degree of Master of Science in the Faculty of Arts and Science

TRENT UNIVERSITY

Peterborough, Ontario, Canada

Environmental and Life Sciences M.Sc. Graduate Program

May 2024

ABSTRACT

Investigation of Dynamics of Particulate Transport under Varying Climate Conditions

Christopher John Schweighofer

A key knowledge gap in aeolian transport research concerns the adjustment of saltation processes to the extreme conditions found within high-latitude regions. A series of wind tunnel experiments were carried out under full climate control and over a wide range in humidity. Particle entrainment and transport within shearing flows of varied wind speed were monitored over beds of varied temperature, and ice content to determine their affect on 1) particle trajectory, 2) saltation cloud height, 3) particle velocity, 4) surface erosivity, 5) mass transport rate and 6) vertical dust flux. Particles were found to have higher velocities over cold beds than dry beds. With a 3% increase in bed moisture content, a significant increase in particle velocity was measured. Fewer particles are ejected from a bed with moisture than a dry bed. The mass transport rate was measured to be 23% higher at -10ºC compared to 30ºC.

Keywords: sand transport, dust emission, boundary layer processes, wind tunnel, high-latitude, cold environments

Acknowledgments

I would like to thank my supervisor, Dr. Cheryl McKenna Neuman. Her unwavering commitment to excellence, immense knowledge, and insightful guidance have been instrumental in shaping the direction and quality of this research. I am truly grateful for her continuous support, encouragement, and the trust she placed in me.

I would like to extend my sincere appreciation to Patrick O'Brien for his technical expertise and assistance. His invaluable insights and support in handling some of the technical aspects of this study have been invaluable.

Furthermore, I would like to thank Gianna Saarenvirta and Lukas Meldau for their assistance in setting up and executing the experiments and for generously sharing their knowledge. Their contributions and their humour have made the work easier and my time in the wind tunnel lab enjoyable.

I would especially like to express my deepest gratitude to my fiancée, Marta. Her unwavering emotional support, encouragement, and belief in my abilities have been a great motivation for me. I am truly grateful for her unwavering presence and steadfast encouragement.

Lastly, I would like to extend my gratitude to all my friends and family members who have provided their support and love throughout my time here at Trent University for which I am truly grateful.

Table of Contents

List of Figures

List of Tables

List of Abbreviations and Symbols

A	Cross-sectional area of a particle
AH	Absolute Humidity
C_d	Drag coefficient
CV	Coefficient of Variation
d	Particle diameter
F_d	Drag force
F_i	Interparticle force
g	Gravitational acceleration
GMC	Gravimetric Moisture Content
k	von Karman Constant
LDA	Laser Doppler Anemometer
PM_{10}	Concentration of particulate matter under 10 microns in diameter
PTV	Particle Tracking Velocimetry
Q	Mass transport rate
R_e	Reynolds number
R_{e*t}	Shear Reynolds number
RH	Relative Humidity
T	Temperature
T_a	Air Temperature
TEWT	Trent Environmental Wind Tunnel
u	Freestream wind speed
u_p	Particle velocity
u_{pv}	Vertical component of particle velocity
u_*	Shear velocity
$u_{p\uparrow}$	Velocity of ascending particles
$u_{p\downarrow}$	Velocity of descending particles
V_f	Vertical dust flux
v_w	Molar volume of water
z	Height above the surface
ε	Erosivity index
μ	Dynamic viscosity
ν	Kinematic viscosity
ρ	Air density
σ	Particle density
ψ_m	Matric potential

Chapter One: Introduction and Literature Review

Temperature and moisture content are both key environmental conditions that govern particle motion in air. Observational and experimental studies conducted by scientists around the world have contributed to our understanding of these factors (McKenna Neuman, 2003, 2004: Mckenna Neuman & O'Brien, 2023; Shao 2008; Wiggs et al., 2003; Yang 2013, 2017; Xiao 2020). The vast majority of research on this subject matter occurs in humid, temperate, and arid regions (Bullard et al., 2016; McKenna Neuman, 2003) where sediment sources are readily available for monitoring and the climate is suitable for long-term monitoring. High-latitude, Arctic, and Antarctic regions, however, are less accessible to researchers and their instruments due to low temperatures, seasonal darkness, and remoteness (McKenna Neuman, 1993). Such regions are often windy because of large thermal gradients and have an abundant particle supply tied to glacial and glacial-fluvial processes, and in the absence of a forest canopy or shrubs, they lie relatively unsheltered. In winter, drifting sand and snow create extensive sediment deposits mixed with or on top of snow and ice (McKenna Neuman, 2004). In high-latitude regions, glacial recession is responsible for the deposition of fine to coarse-grained glacial till which is highly susceptible to transport (McGowan & Sturman, 1997; Nakashima & Dagsson-Waldhauserová, 2019; Szczuciński et al., 2009). The climate conditions and physical features of high-latitude, periglacial environments increase the ability of wind to initiate saltation as compared to warm or humid environments (Bullard et al., 2016; Mckenna Neuman, 1993). In cold, periglacial regions, understanding the effects of temperature and soil moisture on saltation is key to understanding the

geomorphology of these remote, aeolian environments as well as other transport events that occur there. (Kok et al., 2012; Yaping Shao, 2008).

This thesis addresses the knowledge gaps associated with the dynamics of saltation at and below freezing temperatures, employing a novel methodology that requires the use of technology that is not designed to operate under these conditions. Wind tunnel simulations of transport events were conducted under varying temperatures, wind speed, and gravimetric moisture content. Their influence on the mass transport rate and particle velocity was measured while particle trajectories and surface abrasion were observed. This thesis is aimed at expanding our knowledge of the environmental conditions that govern saltation.

1.1 Climate characteristics that determine sediment transport

1.1.1 Wind speed

The initiation of saltation occurs when multiple particles are lifted from the surface due to the forces of fluid drag and lift. The fluid threshold is the windspeed that needs to be exceeded for particles to be entrained and is calculated using Equation 1 (Bagnold, 1941). For any stationary particle, there are four main forces in balance: the interparticle force, the force of gravity keeping the particle on the surface, and the force of lift and drag, imparted by the wind, acting perpendicular to the surface and parallel to the surface respectively (Figure 1.1). When the forces of lift and drag exceed the interparticle force and the force of gravity, the particle becomes entrained.

A = constant
σ = particle density
ρ = air density
g = gravitational acceleration
d = particle diameter

$$u_{*t} = A\sqrt{\frac{\sigma - \rho}{\rho} g d} \qquad \text{(Equation 1)}$$

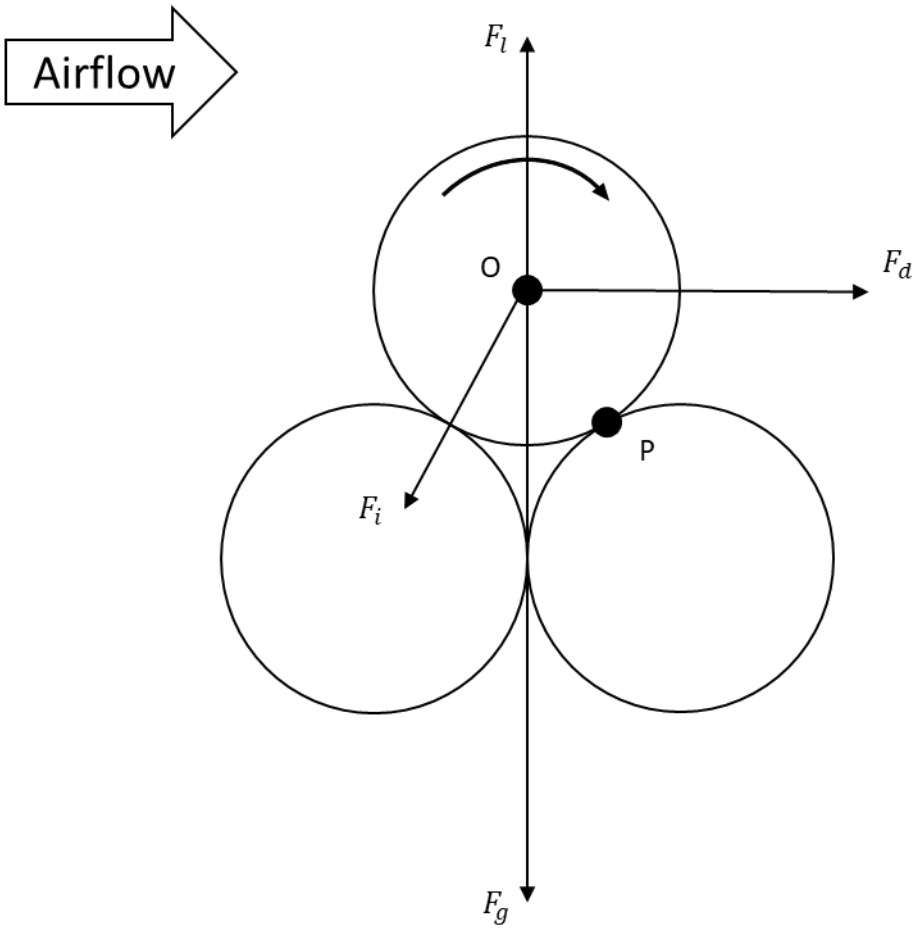

Figure 1.1: Free body diagram showing the forces that act on a particle at rest. F_l is the aerodynamic lift force, F_d is the drag force, F_i is the interparticle force and F_g is the force of gravity. O represents the particle's center of gravity and P represents the pivot point of the particle's motion (as per Shao, 2008).

Field studies conducted in high-latitude regions (Gillies et al., 2012; McKenna Neuman, 1990; Périard & Pettré, 1993) have recorded some of the highest average wind velocities on Earth. Some high-latitude regions such as Antarctica and Greenland experience wind speeds 150% higher than those found in subtropical regions (Bullard et al., 2016). Examples include wind speeds ranging from 20 ms^{-1} at Terra Nova Bay Antarctica (Bromwich, 1989; Parish & Bromwich, 1991) to 30 ms^{-1} at Port Martin, Antarctica while persisting for over 24 hours (Bullard et al., 2016). These extraordinary wind speeds can be tied to selected topographical features commonly found in high-latitude regions. Katabatic drainage for instance is a common driver of persistent, high-velocity winds. These can be found where the landscape exhibits abrupt changes in elevation over a short horizontal distance, like the interior of the Antarctic continent (Périard & Pettré, 1993). Katabatic winds originate at the top of a sloped landform such as a mountain or glacier. Due to radiative cooling, the air mass densifies, and under the force of gravity begins to descend the slope, warming adiabatically (Nappo & Shankar Rao, 1987; Papadopoulos et al., 1997). Katabatic winds have a low relative humidity, desiccating the valleys through which they flow. In terms of initiating sediment transport in these regions, winds created by katabatic drainage play a much more important role than convection-driven winds, which generally initiate sediment transport in subtropical or hot desert regions (Bullard, 2013; Bullard et al., 2016). Common, persistent, and strong katabatic winds are just one example of a climate factor particular to high-latitude regions that provide conditions conducive to sediment transport. High-latitude regions are generally transport-limited. Sufficient sources of sediment that are readily entrained by wind are available, however, extreme conditions are required to transport much of this

sediment. On the other hand, systems where sources can be frozen together in the presence of pore ice are supply-limited. In this case, the airflow has excess momentum as few grains are available to be entrained. As discussed in the results section of this thesis, it is in supply-limited systems where grains move with greater energy and velocity. Using a climate-controlled laboratory, this project aims to collect data on mass transport rates, particle trajectories, and velocities in sub-zero temperatures and over frozen surfaces.

High wind speeds along with seasonal darkness, wildlife, and freezing temperatures make field studies not only difficult but also dangerous to work in and therefore, few measurements have been made in polar regions that pertain to mass transport rates and particle trajectories and velocities (Gillies et al., 2013).

1.1.2 Air temperature

The density (ρ) and kinematic viscosity (ν) of air are both temperature dependent, (Figure 1.2) affecting particle entrainment through the drag force (F_d) and the turbulence of the flow (Re_{*t}) (McKenna Neuman, 2003).

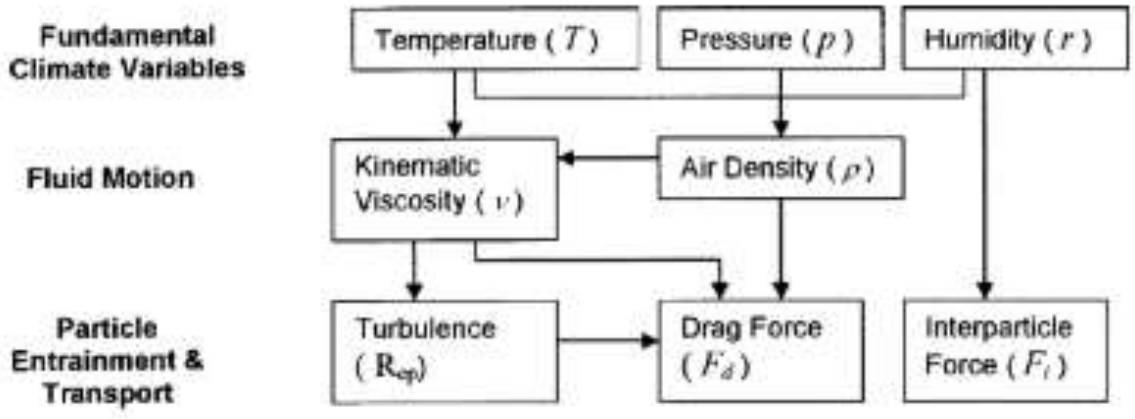

Figure 1.2: Diagram depicting the relationship between various climate variables and their influence on factors that determine particle entrainment (after McKenna Neuman, 2003).

As an air mass decreases in temperature, its density increases. This has implications for particle entrainment as the drag force (F_d) that an airflow imparts on the surface is directly proportional to the density of the air (Shao, 2008). Any decrease in temperature will result in a greater drag force acting on a particle. An example from McKenna Neuman (2004) demonstrates the magnitude and implications of this relationship well: the density of cold dry air at -40 ºC is $\rho = 1.515$ kg m^{-3} while the density of air at 40 ºC is $\rho = 1.128$ kg m^{-3}. Therefore, the density ratio of cold air to hot air in this case is 1.35. Considering density in isolation would suggest that mass transport rates in high-latitude, polar regions could be up to 35% higher than in hot, desert regions.

C_d = Drag coefficient
A = Cross-sectional area of particle
u = wind speed

$$F_d = \frac{1}{2} C_d \rho A u^2 \qquad \text{(Equation 2)}$$

However, another relationship to consider is the influence of temperature on the fluid's dynamic viscosity (μ). The viscosity of air decreases with a decrease in temperature. Viscosity and air density determine the magnitude of the drag coefficient (C_d), a dimensionless variable that represents the resistance to motion experienced by a particle moving through an airflow. It is a measure of the efficiency with which the fluid can transmit drag forces to the object. In the context of particle entrainment, the drag coefficient plays a crucial role. When a fluid flows past a particle, it exerts a drag force on the particle. The magnitude of this drag force depends on various factors, including the size, shape, and surface characteristics of the particle, as well as the properties of the fluid. Particles with a high drag coefficient can have a higher drag force exerted on them,

making them more susceptible to transport. Different particle shapes and sizes have different drag coefficients, and they can vary widely depending on the Reynolds number, which is the ratio of inertial forces to viscous forces in a system and characterizes the flow regime. The drag coefficient can be estimated using mathematical models, one of the simplest being:

$$C_d(R_{ep}) = \frac{24}{R_{ep}}\left[1 + 0.15R_{ep}^{0.687}\right] \quad \text{(Equation 3)}$$

where the particle friction Reynolds number is given as: $R_{ep} = \rho u_r d/\mu$, d being the particle diameter, μ being the dynamic viscosity of the air, and u_r the particle velocity relative to the airstream. As temperature decreases, μ decreases and ρ increases, causing an increase in the Reynolds number which controls C_d. Because R_{ep} is in both the denominator and in the numerator raised to the power of 0.687, the increase in C_d with increasing temperature may balance out the effects of density on F_d. Researchers have yet to investigate the full effect of temperature on C_d.

The level of turbulence within a flow is quantified by the Reynolds number (R_e) and is also determined by the dynamic viscosity and density of the flow. Turbulent flow prevails at higher Reynolds numbers when inertial forces dominate over viscous forces. In the presence of turbulence, particle transport is enhanced through the increase in the lift force via near surface and turbulent structures such as eddies, which are responsible for ejecting particles from the bed (Nickling, 1988). Due to the viscosity difference across a wide range of temperatures, it is expected that colder temperature airflows have higher levels of turbulence than warm airflows. Over a 40°C temperature range, there is a 22% increase in the Reynold's number (Figure 1.3) This relationship has yet to be confirmed

by experimental research. There is a lack of data comparing near-surface velocity profiles in cold air and with saltation.

Figure 1.3 explores the effect of R_e, C_d, and therefore, density and viscosity on F_d via isopleth plots of the ratio of R_e, C_d, and F_d at temperatures below 0°C to R_e, C_d, and F_d at temperatures above 0°C. The ratio of F_{d_cold} to F_{d_hot} decreases when increasing the temperature range from 10 °C to 80 °C. F_d therefore, cannot be the cause of any increase in mass flux with a decrease in temperature which has been observed in recent studies (McKenna Neuman, 2003, 2004) leading to the investigation of other variables affecting saltation rates.

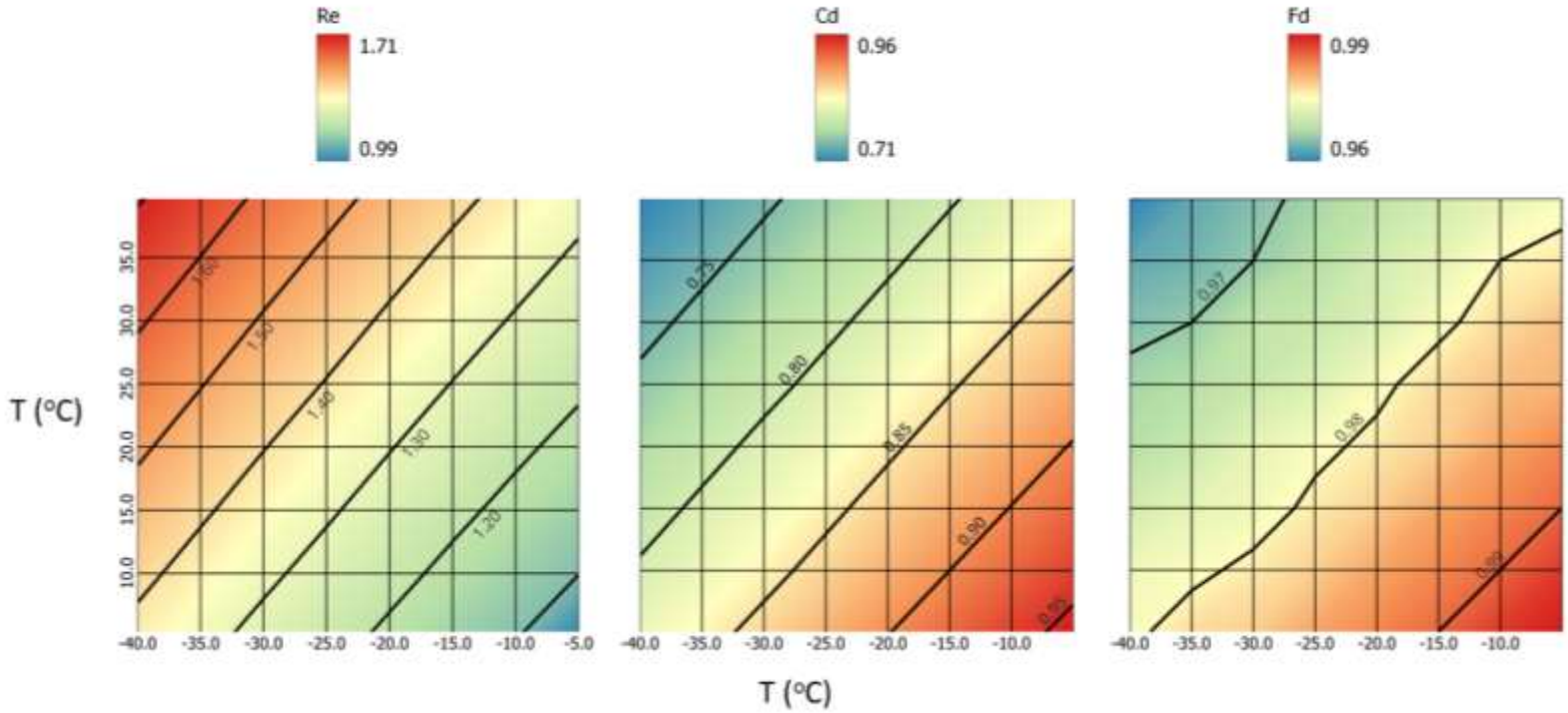

Figure 1.3: Isopleth plots of the magnitude of the ratio of R_e, C_d, and F_d, at temperatures above and below 0°C.

1.1.3 Humidity

The second feature that governs saltation is humidity. Specifically, as humidity rises, saltation rates decrease. Both laboratory and field experiments have measured this phenomenon (Yang et al., 2013). Underpinning this is the concept of matric potential (ψ_m), the tension at which water is held onto the surface of a particle. This variable is strongly dependent on temperature and humidity. The matric potential decreases as temperature decreases or as relative humidity increases as described by the Kelvin Equation,

$$\psi_m = \left(\frac{RT}{V_w}\right) \ln\left(\frac{RH}{100}\right) \quad \text{(Equation 5)}$$

where R is the ideal gas constant at 8.314 J K^{-1} mol^{-1}, T is temperature, V_w is the molar volume of water which is 18.07 cm^3 mol^{-1} and RH is relative humidity.

The matric potential is an indicator of the interparticle force (F_i) acting on a particle. As humidity increases, water is adsorbed onto the surface of a particle through hydrogen bonding (McKenna Neuman & Sanderson, 2008). Cohesive forces exist when two particles share a thin film of this adsorbed water. The water that is held on and between the surfaces of particles has a lower freezing point and remains in a liquid phase well below 0 ºC (McKenna Neuman, 2003; Xiao et al., 2020). Because the contact area between particles can be in the order of square nanometers, the magnitude of this cohesive force is quite small. This force can be estimated by multiplying the matric potential by the contact area (A_c) between any adjacent particles.

$$F_i = \psi_m \cdot A_C \quad \text{(Equation 6)}$$

Due to the irregular shapes of particles, A_c is impossible to determine; however, estimates can be made assuming sphericity for sand particles. When larger amounts of water are added to a surface, the cohesive forces increase. Water in the form of thin films surrounding particles and wedges between particles require greater shear forces than dry surfaces to break these cohesive bonds (McKenna Neuman & Nickling, 1989; Namikas & Sherman, 1995). As pore water increases, these bonds become stronger, further increasing the shear forces required to liberate these grains. At saturation, water may be seen pooling on the surface. This water can act as a trap to stop the motion of saltators upon impact. The following section will explore how particle transport is affected by changing surface moisture contents and pore ice contents.

1.1.4 Surface moisture

As previously discussed, the presence of soil moisture creating tension between two particles can arrest saltation as greater wind speeds are required to entrain particles (McKenna Neuman & Nickling, 1989). However, moisture added to a dry surface changes the way saltating particles interact with it. The wind speed required to sustain saltation over a wet surface is much lower than the wind speed required to initiate it (Comola et al., 2019). On a particle scale, when water is added to the surface, the interparticle forces increase. No longer is water only held to the surface of the grain by hydrogen bonding, but water fills the pore spaces between grains and is held by

capillarity until field capacity is reached. As the amount of capillary water increases, A_c increases faster than ψ_m decreases, increasing the interparticle force. The interparticle force is therefore directly proportional to the inverse of ψ_m (McKenna Neuman & Sanderson, 2008). Particles in a wet surface are bound together much tighter than in a dry surface, requiring increased shear stresses to liberate a particle (Namikas & Sherman, 1995). Once set in motion, however, particles saltating over wet surfaces retain more of their energy compared to dry surfaces. Collisions that result in a near-zero net loss of a particle's kinetic energy are defined as elastic. Particles that undergo near elastic collisions have a high coefficient of restitution; the ratio of final to initial velocity of a particle after impacting the surface.

When temperatures drop below 0°C, the water present in pore spaces begins to undergo a phase change. However, a certain amount of water remains unfrozen between the ice crystals and soil particles, known as the "non-freezable layer". Water occupying the macropores between sand grains has a freezing temperature of 0°C. Within micropores, the freezing point of water can decrease to -45°C as a diminishing pore radius increasingly depresses the freezing point of water (Xiao et al., 2020). Sand has a high percentage of macropore volume (93-95%) as compared to silt and clay (55-80%) so much of the water added to the material used for this project had a freezing point just below 0°C. Frozen surfaces also have a much higher strength than unfrozen surfaces, since the strength of ice increases with decreasing temperature, until -20°C (McKenna Neuman, 1989; Xiao et al., 2020).

Therefore, it would seem that particle ejection from the surface and the mass transport rate should decrease with increasing moisture content and decreasing

temperature. McKenna Neuman (1989) tested this hypothesis in a laboratory experiment by using a sandblaster to abrade frozen surfaces of varying ice content and temperature. Similar to wet surfaces, frozen surfaces allow for more elastic collisions, and since the kinetic energy of saltators is largely retained, aeolian transport can likely be maintained at lower wind velocities. As expected, the number of grains ejected from the surface decreased with a drop in temperature from -5^{o}C to -15^{o}C, however around -20^{o}C, the amount of surface abrasion increased again. This was speculated to arise from a reduction in ductility and strength as hydrogen atoms in the ice lattice lose mobility at low temperatures. This early work demonstrates that frozen surfaces are susceptible to erosion. Few studies have investigated aeolian transport over surfaces with high ice contents. Wind tunnel labs cannot replicate these environments unless they are climate controlled and this represents a considerable obstacle. Despite nearly three decades of research, McKenna Neuman's (1989) findings remain at the forefront of this specific topic. She concluded that although frozen surfaces are highly stable, upon the impact of highly energetic particles, they can be abraded. This abrasion of the surface is a key contributor to the saltation load. Thus, compared to warm environments, cold environments may require much lower windspeeds to sustain sediment transport provided there is an adequate particle supply.

Fully understanding the dynamics of saltation in cold environments is necessary for understanding other aeolian transport phenomenon. Dust emissions are of concern in Earth's high-latitude areas, making up 5% of Earth's global dust budget (Bullard et al., 2016). The following section will investigate the linkages between saltation and dust emission and explore the phenomenon of dust emission in high-latitude regions.

1.2 Saltation as a driver for dust emission

The existing research surrounding the creation and entrainment of dust (particles less than 100 μm in diameter) is extensive, as the repercussions of dust emission are significant on a global scale. Dust emissions come from natural sources but they also can arise from anthropogenic sources. The Sahara Desert for example is the most active natural dust source in the world with far-reaching effects. Dust originating from North Africa plays a crucial role in providing essential nutrients and has the potential to influence the biogeochemical processes in both aquatic and terrestrial ecosystems, particularly in the North Atlantic Ocean and the Amazon Basin (Engelstaedter & Washington, 2007). Furthermore, North African dust has been confirmed to negatively affect both animal and human health. Examples of this include decreases in some amphibian populations in Puerto Rico (Stallard, 2016) and the creation of conditions that support the spread of diseases such as meningitis in the Sahel (Engelstaedter & Washington, 2007). Volcanic sources of dust are also known to have wide-reaching effects. The eruption of the Icelandic volcano, Eyjafjallajökull in 2010 halted air travel over the Atlantic Ocean, and volcanic ash reached as far as the UK and northern Europe, affecting air quality (Richards-Thomas, 2020). Interestingly, polar regions are capable of producing significant local and global-scale dust transport events. Significant natural sources of polar dust include New Zealand (Eden & Hammond, 2003; Selby et al., 1974), Patagonia (Li et al., 2010), Antarctica (Bullard et al., 2016), Alaska (Barr et al., 2023) and Greenland (Amino et al., 2020). Anthropogenic sources of dust are more likely to have local and regional effects as opposed to global effects. The mining industry is quite active in polar regions and fugitive dust from these sources has been known to affect waterways,

flora, and fauna such as caribou and their forage (Chen et al., 2017), cloud nucleation (Fan, 2013) and human health (Griffin & Kellogg, 2004). Predicting dust emissions from a variety of sources and environments is therefore critical to protect human health and sensitive ecosystems. Current models were designed to predict dust emissions from warm, humid climates, not accounting for differences in temperature, humidity, and surface moisture (Lu & Shao, 1999; Y Shao et al., 1993). This can lead to miscalculations in the range and effects of dust from polar regions.

Dust emission can arise from any one of three possible mechanisms. The first involves the release of existing dust particles through particle splash. As saltators impact a surface and transfer momentum to the surface grains, dust present within the pore spaces is released upon the ejection of the larger particles that provide shelter from fluid drag. The second method of dust emission is through spalling or the chipping of larger particles into smaller fractions. Sand particles with dust adhered to the surface by moisture-induced cohesion or electrostatic forces, as well as sand-sized dust aggregates, are fragmented upon impact by saltators. Elastic waves within the aggregate, generated upon impact, may break cohesive bonds between individual particles (Kok et al., 2012). Finally, aerodynamic lift is the third method by which dust is entrained. It is by far the most uncommon and therefore least important mechanism. Due to the strong bonds between dust-sized particles, the direct lift of particles from the surface requires wind velocities that far exceed the threshold for saltation (Kok et al., 2012). In a natural setting, aerodynamic lift alone provides insufficient drag to break interparticle bonds and initiate dust entrainment (Shao et al., 1993). Saltation is therefore the main cause of dust emission. The relationship between saltation flux/mass transport rates and dust flux has

been investigated thoroughly and models have been created to predict the amount of dust emitted due to saltation bombardment. Lu and Shao (1999) proposed a new model for dust emission building on the work of Shao et al. 1993 and Gillette and Passi (1988). By creating a model based on the understanding that saltating particles carve out craters in the surface, they determined that V_f is directly proportional to u_*^{n+1}, where n = 2 ~ 3. To simplify, for hard surfaces $V_f = u_*^3$ and for soft surfaces, $V_f = u_*^4$. Since Q is directly proportional to u_*^3, the ratio of V_f/Q is linearly proportional to the fraction of dust within the material and u_* (Lu & Shao, 1999). Despite being a quite advanced model, there are some limitations including but not limited to the absence of temperature and relative humidity as parameters. One of the goals of experiment 1 is to understand if this absence is consequential when predicting V_f.

There is strong evidence to suggest that global dust emissions increased during cycles of glaciation due to increased aridity, weakened hydrological cycles, strong winds, decreased global biomass, and an influx of fine sediment sources (Bullard, 2013). Today, the characteristic, high wind speeds in polar regions have the potential to dry surfaces quickly, making particle suspension possible (Bullard et al., 2016). Despite warm environments currently being responsible for the majority of Earth's dust emissions, the entrainment and dispersion of dust still occur in high-latitude regions (Bullard, 2013). Present-day models for dust emission do not encompass the range in temperature, humidity, and surface properties characteristic of these regions. Therefore, this could also indicate that the quantity of dust that is resuspended in high-latitude regions is greater than in hot, desert regions. Few measurements have been carried out to quantify these differences.

1.3 Core Objectives

The goal of this research is to extend our understanding of aeolian transport processes across a wide range of conditions on planetary surfaces. Six hypotheses were tested to achieve this goal:

1. Over a dry bed, the saltation cloud height will increase with decreasing temperature.
2. Over a dry bed, the mass transport rate will increase with decreasing temperature.
3. Vertical dust fluxes over a bed of dry sand will increase with decreasing temperature.
4. The proportion of particles traveling in creep and reptation relative to those moving in ballistic trajectories will decrease with an increasing ratio of pore ice to liquid water.
5. Mean sand particle velocity within the transport cloud will increase with an increasing ratio of pore ice to liquid water.
6. Fewer particles will be ejected during a collision with a frozen surface (below 0ºC with pore ice), relative to a warm dry surface.

The study of sediment transport in aeolian environments has been largely based on quantitative observations. To fully understand sediment transport across a full range of environments, a shift must be made to incorporate cold weather transport phenomena into existing transport models (McKenna Neuman, 1989). To test these hypotheses, a novel

methodology has been designed, requiring the modification and calibration of instruments to operate at sub-zero temperatures.

Chapter 2: Methods

2.1 Overview of Experimental Design

This investigation of aeolian transport processes under cold conditions incorporates two experimental designs; the first involves the measurement of mass transport, saltation cloud height, and dust emission over dry surfaces across a 40°C temperature range (30°C to -10°C), and the second involves the measurement of mass transport, particle velocity and the amount of erosion for surfaces of varying moisture content (dry, low, medium and high) across an 8°C temperature range (3°C to -5°C). Each experiment required the development of a saltation event over a bed of sand extending along the entire working section of the wind tunnel. Laser Doppler Anemometry (LDA) was employed to measure the 2D velocity of saltators allowing for the quantification of saltation, erosion, and dust emission. A wedge sand trap was used to quantify the mass transport rate while laser sensors sampled the saltation intensity. To measure the dispersion of dust released from the surface, DustTrak aerosol monitors sampled the airflow in a vertical profile.

During Experiment 1, two relative humidity regimes were investigated; a low humidity of 35% and a moderate humidity of 58%. Most periglacial environments are characterized by relative humidities between 50-90% year-round. Saltation events were simulated at freestream wind speed settings of 7, 9, and 11ms^{-1} at lab temperatures of 30,

25, 15, 5, 0, -5, and -10ºC. Although only a range of 4ms^{-1}, this range is characteristic of the average windspeeds that are found in the Arctic. Although Arctic regions see strong gusts of wind, it is the persistent winds of lower velocities that form the erosional and depositional features seen across these landscapes. Each run lasted approximately 4-5 minutes, inclusive of the ramping up and ramping down of the fan motor. Through pilot testing it was determined that this time frame allowed for a sufficient amount of data collection while ensuring that the bed of sand would not deflate. Once the fan motor reached the requested windspeed, a sand feed was initiated to seed the development of a saltation cloud.

In Experiment 2, three temperatures of 3, 0, and -5ºC and four wind speeds of 6, 7, 8, and 9 ms^{-1} were established. Investigating a narrow temperature range around the freezing point of water allowed for the examination of the effect of phase changes in pore water on saltation.

2.2 Facility

The Trent Environmental Wind Tunnel (Figure 2.1) is a research facility that simulates sediment transport in atmospheric boundary layer flows. It has a 13.5-meter-long working section with a cross-section of 0.77 mH x 0.7 mW. An AC variable control motor and fan on the downwind end of the tunnel are used to pull air through an intake bell equipped with a straw filter to straighten and compress the flow. A trip plate containing an array of 2 cm diameter wooden dowels initiates a strong shear within the flow, forcing the boundary layer to develop within a few meters of the intake. Above the trip plate is an auger-driven, sand feed controlled by a variable control motor capable of

introducing sand from a reservoir atop the tunnel into the freestream at a constant rate. As these particles impact the bed surface, they trigger the development of the saltation cloud through the momentum transfer and the initiation of particle splash. For all experiments, the variable control motor was set to produce a sand output of 2.8 g s^{-1}. The lab in which the tunnel is located is fully insulated and acts as an environmental chamber allowing for the simulation of aeolian transport in temperatures as low as -15°C and humidity ranging from 3 to 70% (McKenna Neuman, 2021). An industrial-style refrigeration unit ensures that the laboratory temperature is accurate to ±1°C while an industrial dehumidifier and kettle humidifier are used to attain the requested relative humidity with an error of ±2%. This allows simulation of the conditions of periglacial environments to a degree that has yet to be undertaken by workers elsewhere. However, at $T < 0$°C and $RH > 60\%$, icing of the coils becomes a problem in the lab. Therefore, the maximum achievable relative humidity was 58%.

The TEWT has its unique flow characteristics that must be described and quantified before experimentation as the airflow within the tunnel affects the processes being monitored. To assist in the characterization of the flow, three traverse-mounted pitot tubes are located at 2.55 m (Pitot X), 5.59 m (Pitot Y), and 10.13 m (Pitot Z) downwind of the trip plate. These instruments are designed to simultaneously sample air velocity at any given fixed height above the bed surface. They are also programmed to measure air velocity while cycling through a profile of 24 heights between 5 mm to 400 mm above the surface. From this profile, the aerodynamic roughness length (z_0) and the shear velocity (u_*) can be calculated. After both experiments 1 and 2 were complete, velocity profiles of the airflow for each experimental setting were measured. First, as in

experiment 1, the tunnel was filled with dry, silica sand, and 5 replicate profiles were taken at 6 ms^{-1}, 7 ms^{-1}, 8 ms^{-1}, 9 ms^{-1}, and 11 ms^{-1}. The bed surface had to be re-leveled between 6 ms^{-1}, 7 ms^{-1}, and 8 ms^{-1} and between each replicate at 9 ms^{-1} and 11 ms^{-1} due to the deflation of the surface during the profiling. Experiment 2 dealt with wet and frozen surfaces with very little saltation and bed deflation so a second set of profiles was taken at the same freestream settings where the bed was wetted to ensure near-clean airflows. For a given windspeed, the five profiles at each pitot tube were averaged and then plotted with an exponential trendline. Given the form of the equation, $y = a^{bx}$, $z_0 = a$, and the shear velocity is calculated as $u_* = \frac{k}{b}$, where k is the von Karman constant equal to 0.41.

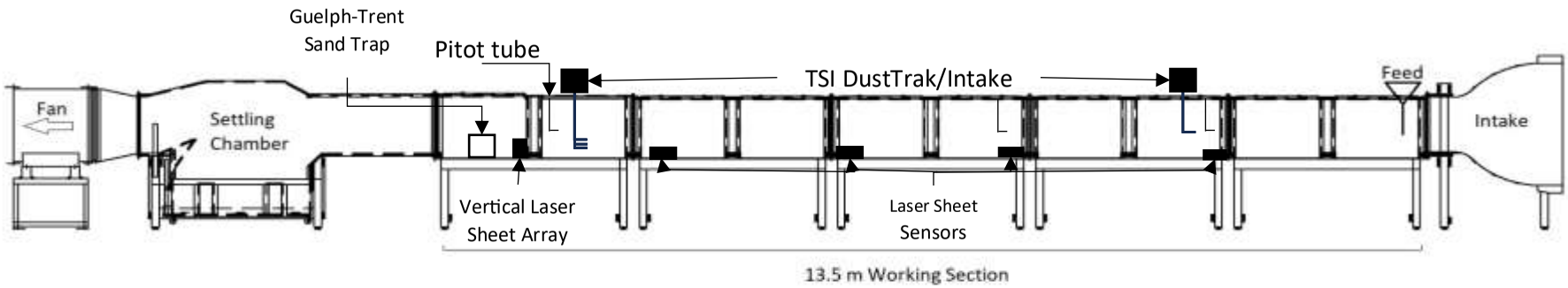

Figure 2.1: Schematic of the Trent Environmental Wind Tunnel showing the placement of the instrumentation used in both Experiments 1 and 2.

2.3 Test Surface Design

2.3.1 Dry beds

The entire working section of the wind tunnel as well as the particle feed reservoir was filled with white silica sand, creating a 12-m long, 0.7-m wide, and 0.025 m thick bed of sand. The total volume was 0.21 m^3, which given a bulk density of 1600 kg m^{-3}, amounted to approximately 335 kg (739 lbs) of sand. Once poured onto the wind tunnel floor, the sand was leveled flush with the side rails of the wind tunnel. Each surface was flat and loosely packed. The test sand had a mean particle diameter of 295 μm (Figure 2.2). This is a common grade of sand that is similar to natural aeolian deposits such as desert dunes (Bagnold, 1941; Lancaster, 1981). Measuring the dust flux above this surface is dependent on the inclusion of dust within the sand bed. The sample has a small proportion of silt below 63 μm in diameter (Figure 2.2). It is assumed that there is a supply of PM_{10} within the sample as this material is naturally dusty. A Horiba LPSA was used to measure this however no particles below 63 μm was measured in this sample. Nonetheless, this assumption can be made because the entire working section of the wind tunnel was filled with sand so a small amount of dust within the bed can lead to high concentration readings. Further, no water was added to the surface so that the dust could be entrained. The bed surface gravimetric moisture content was confirmed to be 0-0.2% across all runs. After the run was completed, the bed, having been deflated and sorted was mixed by hand, and new sand was added to avoid grain-scale armouring and the exhaustion of the PM_{10} supply. This experimental design is concisely shown in Table 2.1 below.

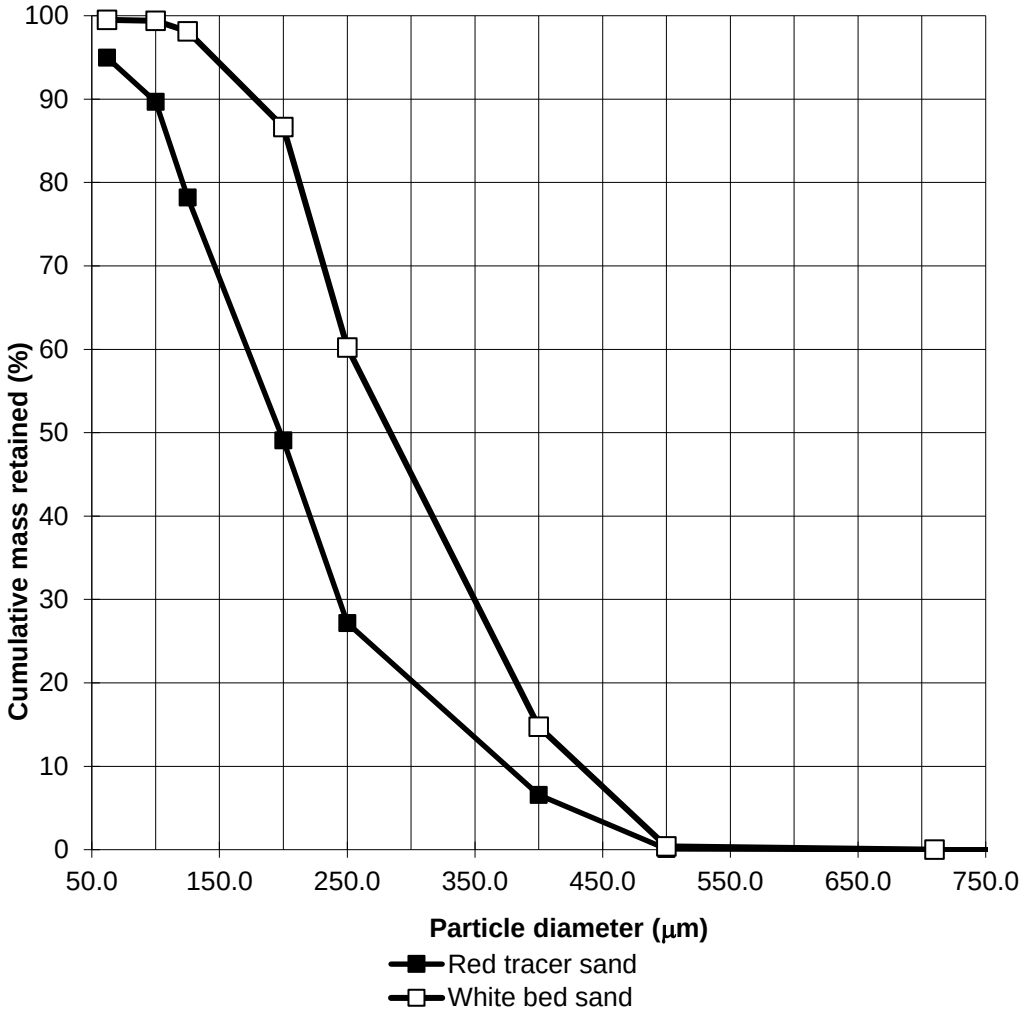

Figure 2.2: Particle size distribution for the silica, test-bed sand, and for the red, tracer sand.

Table 2.1: Climate conditions governing each run during Experiment 1. Transport events were simulated at 7, 9, and 11 m s^{-1} at a low (35%) and high (58%) relative humidity at each temperature. Each wind speed was run 3 times, one after the other, to observe any temporal changes in dust concentrations.

Temperature (^{o}C)	**Relative Humidity (%)**	**Absolute Humidity (g m^{-3})**
30	35	10.6
	58	17.6
25	35	8.1
	58	13.4
20	35	6.1
	58	10.0
15	35	4.5
	58	7.4
10	35	3.3
	58	5.5
5	35	2.4
	58	3.9
0	35	1.7
	58	2.8
-5	35	1.2
	58	2.0
-10	35	0.8
	58	1.4

2.3.2 Beds with moisture added

There are multiple methodologies by which water can be added to a surface to achieve the desired moisture content. Pilot testing began with measuring particle velocities over small trays of wet and frozen material. Known amounts of sand and water was added to a concrete mixer and mixed for 5 mins, attaining a precise and replicable moisture content (Table 2.2). Early measurements, however, showed that the fetch associated with these small trays was too short to meet the aims of this study. This prompted the move towards filling the entire working section of the wind tunnel with sand. With this test design, however, the methodology by which water was added to the previous sediment trays was abandoned as wetting and transporting 350 kg of sand would have required an excessive amount of time and space to dry out the material once wetted, as well as a level of manpower that was unattainable.

For the second set of experiments, the following method was contrived to conserve time and material. An 8-liter, hand-pump garden sprayer was used to apply water to the surface of the test bed in systematically varied quantities (2, 4, and 6 L). Corresponding gravimetric and volumetric moisture contents are reported in Table 2.2. It was difficult to ensure that the surface reached a consistent moisture content before each experiment due to the large surface area of the bed and the varying spray intensity of the pump. As a consequence, some targeted moisture contents required multiple attempts. This occurred when trying to achieve a low moisture content, but due to the overapplication of water, a high moisture content was achieved instead. Gravimetric moisture contents were calculated after the run was complete. Bed moisture content was determined by scraping the top grains off the surface of a 100 cm^2 area with a thin

stainless-steel blade both before and after the experiment to account for the effects of evaporation. Additionally, either cores or frozen surface chips were broken off to provide a measurement of the bulk water content of the test bed. Cores were collected by inserting into the bed two stainless steel lab scoops (Fisher Scientific product number 01189170) attached so that the convex sides faced outwards.

This test design was used to assess the effect of pore water and ice content on particle velocity, saltation height, erosivity, and the fetch effect. Table 2.2 summarizes the climate conditions for each run.

				Surface GMC (%)				Surface VMC (%)				Reps
	Humidity		Moisture Descriptor	Mean		CV		Mean		CV		
	RH (%)	AH (g/m^3)		Before	After	Before	After	Before	After	Before	After	
3°C	28-30	1.9-2.0	dry	0.17	0.00	0.16	-	0.11	0.00	0.16	-	1
			low	2.82	2.52	0.22	0.48	2.20	1.01	0.09	0.93	2
			medium	6.63	4.98	0.19	0.29	3.23	1.64	0.13	0.43	2
			high	8.20	6.28	0.33	0.15	5.08	3.22	0.18	0.56	3
0°C	30-40	1.5-1.9	dry	0.00	0.03	0.00	0.26	0.00	0.02	0.00	0.26	1
			low	3.12	1.57	0.10	0.44	1.95	0.98	0.10	0.44	1
			medium	3.19	5.29	0.22	0.70	1.99	3.31	0.22	0.70	1
			high	9.56	16.27	0.62	0.72	5.97	10.17	0.62	0.72	1
-5°C	30-35	1.0-1.2	dry	0.17	0.00	0.50	-	0.11	0.00	0.50	-	1
			low	5.55	3.38	0.11	0.11	3.47	2.11	0.11	0.11	1
			medium	8.23	8.15	0.36	0.11	5.15	5.09	0.36	0.12	1
			high	13.40	11.02	0.91	0.71	8.38	6.89	0.91	0.71	1

Table 2.2: Climate and surface conditions governing each run during Experiment 2, along with the number of replications completed at each nominal wind velocity. The moisture content of four core and four surface samples was averaged

2.3.3 Bed temperature

Temperature measurements were obtained for the airflow and test bed throughout each experiment. A Campbell Scientific data logger sampled temperature using copper-constantan thermocouples. The data logger recorded the time-averaged temperature over 5 s intervals for the duration of the experiment in a vertical profile, 10 m downwind of the intake (Figure 2.3). This provided a reference temperature gradient. Thermocouple 1 (TC1), was secured to the side rail of the tunnel bed, 10 mm above the test surface. Thermocouple 2 (TC2), also secured to the side rail, measured temperature at the bed surface. Thermocouple 3 (TC3), which was inserted through the tunnel floor, measured the temperature at the base of the test surface. Measuring the temperature of each surface is important as the main thermistor for the climate control system is wall-mounted at the entrance of the laboratory and therefore, does not reflect bed temperature. Further, the thermocouple data verified that the temperature had stabilized and reached the target for the experiment.

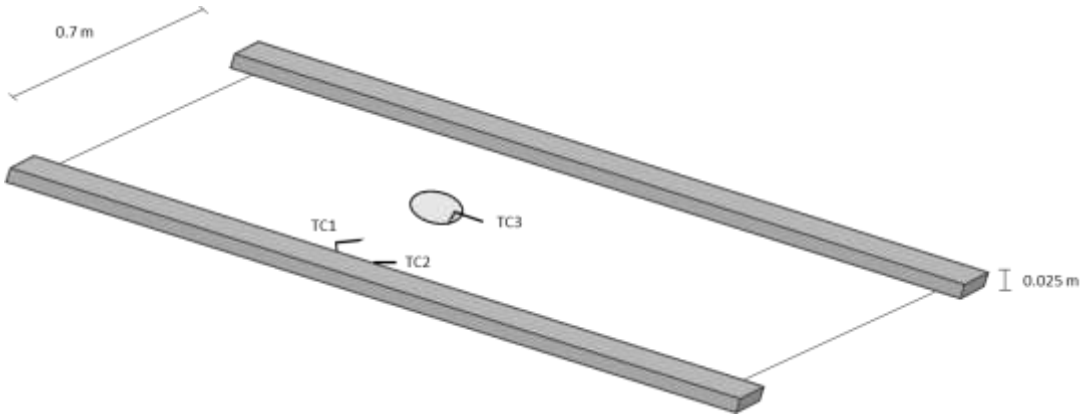

Figure 2.3: Diagram of thermocouple location, 10 m downwind of the entrance to the working section of the tunnel (i.e., fetch distance).

2.4 Assessment of Sand Transport

2.4.1 Guelph-Trent wedge sand trap

Throughout both experiments, a passive, isokinetic sand trap near the end of the wind tunnel was used to facilitate the direct measurement of the vertically integrated mass transport rate (Q). Isokinetic conditions through and around the inlet of the trap ensure minimal disruption of the airflow, allowing for more accurate measurement of mass transport. The collection efficiency of the trap (92%) is dependent on these isokinetic conditions (McKenna Neuman & Nickling, 1997). Sand that enters the 2 cm x 20 cm inlet is redirected via a rectangular, grounded funnel, through the floor of the wind tunnel, to an electronic laboratory weigh scale where it accumulates. The mass of the accumulated sediment was measured in real time and then sent to an Excel output sheet every second for the duration of the experiment. Using the cumulative mass output from

the Guelph-Trent wedge trap, the mass transport rate for the simulation was calculated using the following equation:

Where:
m = cumulative mass (kg)
H = height of the sand trap opening (m)
W = width of the sand trap opening (m)
t = duration of collection period (s)

$$Q = \frac{m}{(H \times W) \times t} \quad \text{(Equation 7)}$$

The test bed was leveled around the trap inlet and subsequently sprayed with an aerosolized polymer fixative (hairspray) to arrest scouring, which can lead to particle under-collection. Since this instrument remains in a fixed location it cannot assess the fetch effects of the saltation cloud. To address this, a series of optical sensors were mounted to the tunnel floor at 2.5, 5.45, 7.70, and 10.02 m downwind of the trip plate.

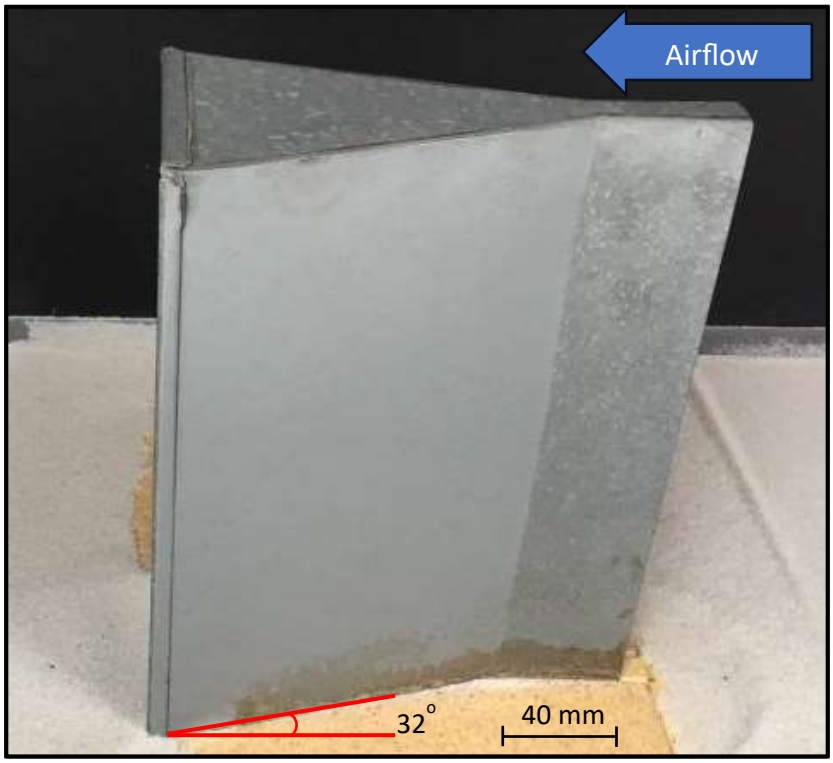

Figure 2.4: Passive, isokinetic sand trap, located 10.9 m downwind of the intake.

2.4.2 Optical sensors

The assessment of the vertical saltation profile and the fetch effect was done using an array of Keyence™ laser sheet sensors, which includes the LV-N11MN amplifier and the LV-NH300 sensor head, comprised of a transmitter and a receiver. The amplifier allows the operator to adjust the light output and the sensitivity of the receiving unit and to set saturation limits. The transmitter emits a 32 mm-wide laser with a wavelength of 660 nm at an output of 310 µW. When the transmitter's laser is aligned perfectly toward the receiver, a maximum of 5 Volts can be detected. Interruption of this beam, due to particles saltating through it, results in a voltage drop that was recorded by the main operating computer (DAQbook). This average drop in voltage over the time of sampling,

when divided by the initial voltage reading when the beam was uninterrupted, represents the proportion of the beam blocked by saltating particles.

Two separate laser sheet orientations were employed. For experiment 1, under dry bed conditions, five laser sheet sensors were stacked vertically (5, 11, 18, 23, and 31 mm above the surface of the bed) and staggered (Figure 2.5a). Staggering the sensor heads was necessary to have a profile of 5 laser sheets measuring below 40 mm above the bed, as the sensor heads are 12.4 mm thick. The transmitter and the receiver heads were placed 0.27 m apart, in the center of the bed. This distance was chosen to avoid exceeding the sensor's maximum detecting distance of 0.30 m while covering approximately 40% of the wind tunnel width. This vertical array was placed 10.65 m downwind, 0.25 m in front of the Guelph-Trent sand trap (Figure 2.5b). Hairspray was sprayed in between and around the sensors to avoid scouring of the bed around the sensor and exposure of the mount on which the array was fastened. From the data collected during each run, a vertical saltation intensity profile was created for each windspeed, temperature, and humidity condition. In Experiment 2, under wet bed conditions, each sensor pair was mounted on its own, custom-made board so that the laser sheet was 5 mm above the bed and the sensor heads were 27 cm apart (Figure 2.5c). The mounted laser sheet sensors were located 2.5, 5.45, 7.70, and 10.02 m downwind of the trip plate. By employing a downwind distribution of laser sheet sensors, the effects of the fetch on the transport rate with increasing moisture content could be assessed.

Because the laser sheet sensors provide an indirect measurement of the mass transport rate, the results provide a dimensionless index of saltation intensity.

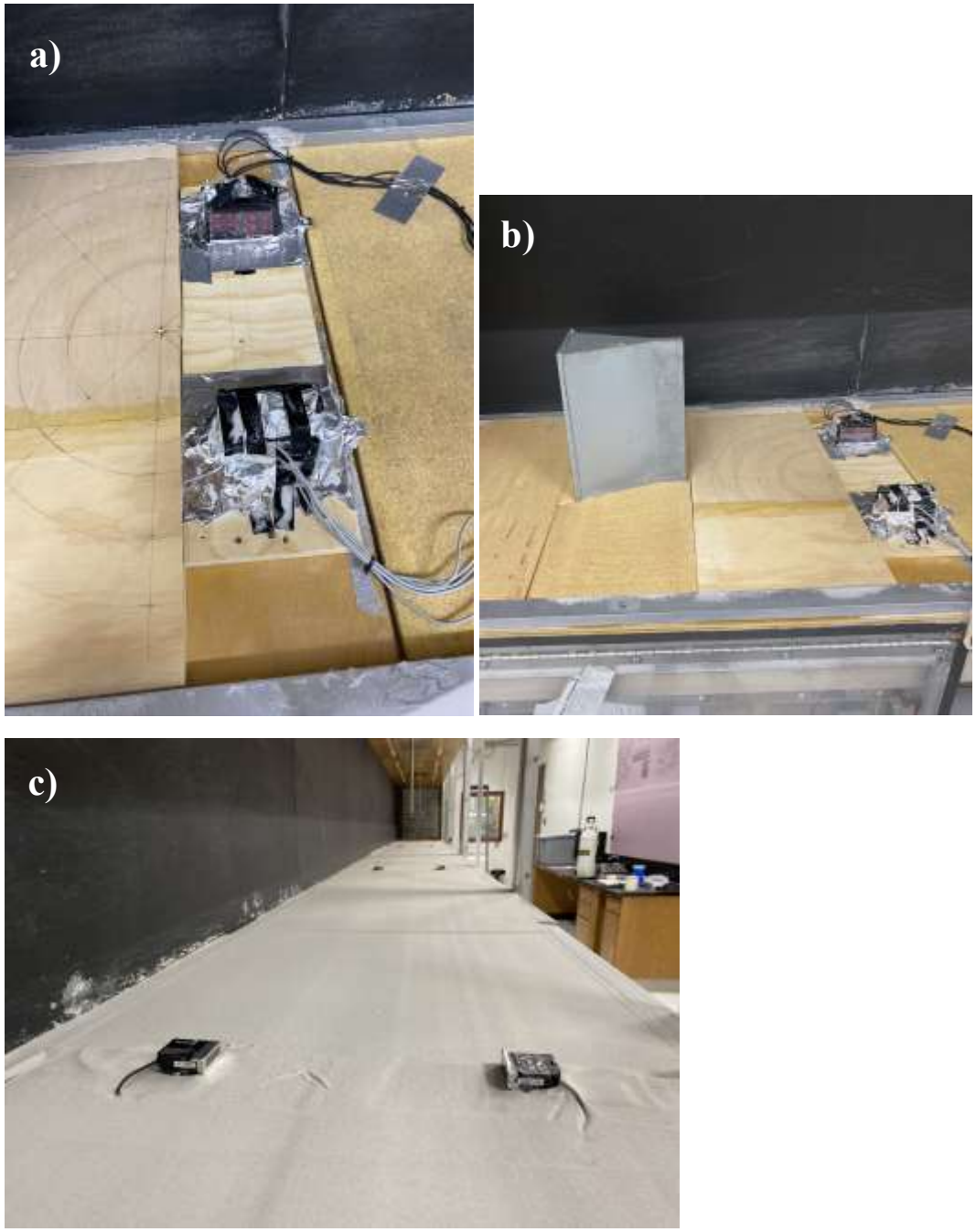

Figure 2.5: a) Vertical stack of staggered Keyence™ laser sheet sensors.
b) Laser sheet array in relation to the Guelph-Trent sand trap
c) Downwind allocation of laser sheet sensors prior to the addition of water to the bed

For scale, the laser sheet head dimensions are 42.5 x 41 x 12.4 mm.

2.4.3 Image analysis of tracer sand

One of the goals of Experiment 2, was to evaluate the response of the wetted and/or frozen surfaces to impact and to provide a measure of the likelihood of successive saltation. Successive saltation is a term used to describe when a particle rebounds off a surface without entraining other particles (Tsuchiya, 1969). In order to do this, a red-coloured sand with an average diameter of 212 μm, was put into the sand feed reservoir and was released onto the bed of white silica, acting as a tracer. Figure 2.2b shows the particle size distribution for this material. Red grains transfer their momentum to the white surface grains, ejecting them from the surface and into the flow. Some grains that reach the end of the tunnel are collected by the sand trap. The sand was collected from the scale after the run and put in a plastic bag in preparation for subsequent analysis.

Each sample collected from the sand trap was photographed using a Canon EOS Rebel SL3 mounted on a tripod using a shutter speed of 1/25, aperture of 8.0, and ISO of 800. The particles were evenly distributed on black posterboard and shaken until a layer of sand had formed that was at least 5 grains thick. If the layer of sand was too thin, the particles were darkened by the black paper behind them, creating inconsistent lighting. To ensure consistent lighting, the pictures were taken in a room with sufficient overhead lighting so that the camera would not cast a shadow on the grains. Once placed directly below the camera, the first of three photographs were taken. Between each photograph, the sample was shaken to redistribute the grains on the posterboard.

The relative proportion of white to red particles provides an index of the erosivity of the surface. To quantify this, each image was analyzed by a custom code written by Patrick O'Brien which counted the number of white and red pixels. The code was

calibrated by sampling ten red pixels and ten white pixels of varying colour intensity within these images and recording their RBG values. This provided a range of RBG values that could be considered either red or white. The program selected particles that fell within 2 standard deviations of the average of the ten RGB values. Standard deviations above 2 allowed the program to count some pixels twice, once as red and once as white. A standard deviation below 2, resulted in particles being left uncounted. Taking the proportion of white pixels to red pixels produces a value termed, the Surface Erosivity Index (ϵ). The Erosivity Index was compiled for each surface into a bar graph, showing the change in erosivity across test beds of different moisture content.

2.5 Assessment of Particle Kinetics

During Experiment 2, where moisture was added to the bed, the velocity components of the saltating particles were measured. A Dantec 2-D Laser Doppler Anemometer (LDA) was used to calculate the horizontal (u) and vertical velocity (v) of a saltating particle. This is done for each particle that passes through its 0.04 mm^3 sampling volume created at the intersection of four lasers.

Many electronic instruments, including the LDA processor and laser head, are not designed to operate below 0ºC. A thorough investigation of the LDAs operation in cold temperatures was undertaken to assess its accuracy and precision during runs at and below 0ºC. Testing began by attaching copper-constantan thermocouple wire to the processor compartment, the LDA laser head, and the traverse to sample air temperature. The temperature was monitored as it warmed up for one hour in a control room and for an hour of data collection in the lab at 0ºC. The validation rate of the data collection was recorded and plotted against the temperature. This showed that as the temperature in the lab decreased, so did the validation rate. Heaters were then mounted onto the side of the compartment containing the processor and the experiment was repeated. When the processor maintained a temperature of 15ºC, the validation rate did not drop below 90%. Appendix A provides details on this calibration exercise.

The LDA was placed 10 m downwind so that the laser beams were normal to the airflow and sampled particle velocities in vertical profile at heights of 4, 6, 8, 10, 20, and 40 mm above the bed (Figure 2.7). Data collection was prioritized at the downwind end of the tunnel where the saltation cloud and the airflow come into equilibrium. Due to the

exponential decay in the number of particles saltating within the transport cloud with height above the test bed, the cloud is expected to be contained within the first centimeter above the bed which is why most measurements occur at and below 10 mm of vertical height (O'Brien & McKenna Neuman, 2019, 2023). The duration of each sampling period was 20 seconds per location. The settings summarized in Table 2.3 were used to ensure the highest possible data validation rate.

Table 2.3: LDA BSA Flow Software settings employed for the collection of particle velocities.

Parameter	**LDA 1 Setting**	**LDA 2 Setting**
Minimum Record Length	32	32
Maximum Record Length	64	64
Sensitivity	1200 mV	1400 mV
Signal gain	14 dB	14dB
Anode Current Limit	1500 μA	2000 μA
Level Validation Ratio	4	4

Figure 2.6: LDA Flow Explorer laser head, traverse mounted and on top of mobile compartment within which is stored the processor. The LDA is positioned normal to the airflow within the tunnel, where the intersection of the lasers (sampling volume) is situated approximately in the middle of the tunnel.

2.6 Assessment of the Dust (PM_{10}) Flux

Two TSI^{TM} DustTrak II aerosol monitors 8530 were used to sample dust concentration within the airflow. Using a light-scattering laser photometer, the DustTrak outputs real-time dust concentrations for particles between 0.1 and 10 μm. A flexible plastic tube connects the DustTrak to an L-shaped, metal intake tube (Figure 2.8) which was fed through the roof of the wind tunnel where it remained at a fixed height above the bed for the duration of the experiment. Four DustTraks sampled the airflow in the wind tunnel; one 0.3 m above the bed and 1.2 m downwind of the sand feed, and three DustTraks 9.5 m downwind at the end of the tunnel at 0.1, 0.2, and 0.3 m above the bed. A DustTrak close to the intake sampled the background concentration of dust entering the tunnel. This background concentration was subtracted from the dust concentrations measured by the downwind DustTraks. A vertical profile of intake tubes was used to measure the dust flux (V_f) or PM_{10} emitted from the surface of the test surface. The DustTrak measured the dust concentration every second for one minute. Once the required windspeed was attained, the DustTraks were manually started. Three, one-minute sampling periods were completed at the same velocity to capture variations in dust concentration with time. The wind tunnel fan, the laser sheet output, and the scale reading output were stopped once the DustTrak finished sampling the airflow.

Like the LDA system, this instrument's operational temperature range, recommended by the manufacturer, does not extend below 0^{o}C. Calibration of the instrument was necessary to demonstrate that reliable data collection can occur at temperatures below 0^{o}C. Each DustTrak aerosol monitor was connected to a bucket via vinyl tubing. Once the tubing was fed through the bucket, 0.5 g of silt ($d < 65$ µm) was

loaded into the bucket. Subsequently, the bucket was shaken for 3 s to suspend the particles before sampling began. The DustTrak then measured the PM_{10} concentration inside the bucket for 60 s. Each DustTrak underwent ten replications at both 20°C and 0°C. There was no significant difference in the dust concentration sampled at 20 °C and 0°C suggesting that the instrument is capable of functioning and providing reliable measurements at low temperatures. Appendix B presents the results of this calibration and explains the methodology in further detail.

Figure 2.7: DustTrak intake tubes with an inner diameter of 3 mm, flow-aligned to allow for particulates to enter, at their fixed height (0.1, 0.2, and 0.3 m) above the sand bed. The tubes were taped together to ensure their positioning remained constant throughout the experiment.

2.7 Boundary Layer Flow Characteristics

Finally, it is important to understand and characterize the flow conditions within the wind tunnel during each experiment.

The requested, nominal freestream velocities (u_f) at which the wind tunnel was run were 6, 7, 8, 9, and 11 ms^{-1}. Table 2.4 details the corresponding shear/friction velocities (u_*) and aerodynamic roughness lengths (z_0). These profiles were created by running the wind tunnel at five freestream velocities and sequentially measuring the wind velocity at 24 heights above both a wet, immobile bed surface and a dry, mobile bed surface. Three traverse-mounted pitot tubes measured a velocity profile at 2.55 m, 5.59 m, and 10.14 m downwind. Figure 2.8a shows the velocity profiles for each nominal wind speed with a dry bed, wherein the flow was saturated with particles. This is representative of the conditions in Experiment 1 where the system was transport limited. In this figure, the bottom four points of each curve depart from the linear region which is the constant stress region (rate of change with velocity is constant). These four points have a similar curve to that of the freestream, where the velocity does not change with height above the bed. The fluid stress is greatly reduced and insufficient to entrain additional particles from the bed. In response to the saturation of the saltation cloud, the boundary layer thins and u_* increases. Further, aerodynamic roughness lengths are seen to increase with increasing wind speed. z_0, is a measure of the surface's capacity to absorb momentum due to its roughness. In a dry system with saltation, z_0 becomes the product of surface roughness and saltation roughness. Therefore, at higher windspeeds, with more particles in transport, z_0 increases.

For the bed wetted to prevent particle motion (Figure 2.8b), all the points fall within the linear, constant stress region as there is no saltation cloud to extract momentum from the airflow (less shear within the flow). These calculated u_* values are representative of the conditions for Experiment 2, where the surface was wet and/or frozen. z_0 values at each windspeed are of the same magnitude since there is no added saltation roughness.

Table 2.4: Summary of airflow characteristics. Freestream velocities were measured by pitot tubes positioned in the freestream of the tunnel (35 cm above the bed) during the experiment. u_* and z_0/z_{0s} values are an average of the calculated values at 2.55 m, 5.59 m and 10.14 m downwind to ensure that u_* and z_0 are representative of the entire working section. R^2 values correspond to the trendlines in Figures 2.8a (where the bottom five points are excluded) and b.

Freestream Velocity (ms^{-1})	Dry Bed			Wet Bed		
	u_*	z_{0s}	R^2	u_*	z_0	R^2
6.00	0.26	0.0019	0.994	0.21	0.0040	0.998
7.13	0.35	0.0148	0.977	0.28	0.0009	0.996
8.20	0.49	0.0331	0.979	0.32	0.0007	0.999
9.33	0.55	0.0471	0.985	0.36	0.0008	0.997
11.51	0.76	0.0974	0.984	0.42	0.0007	0.998

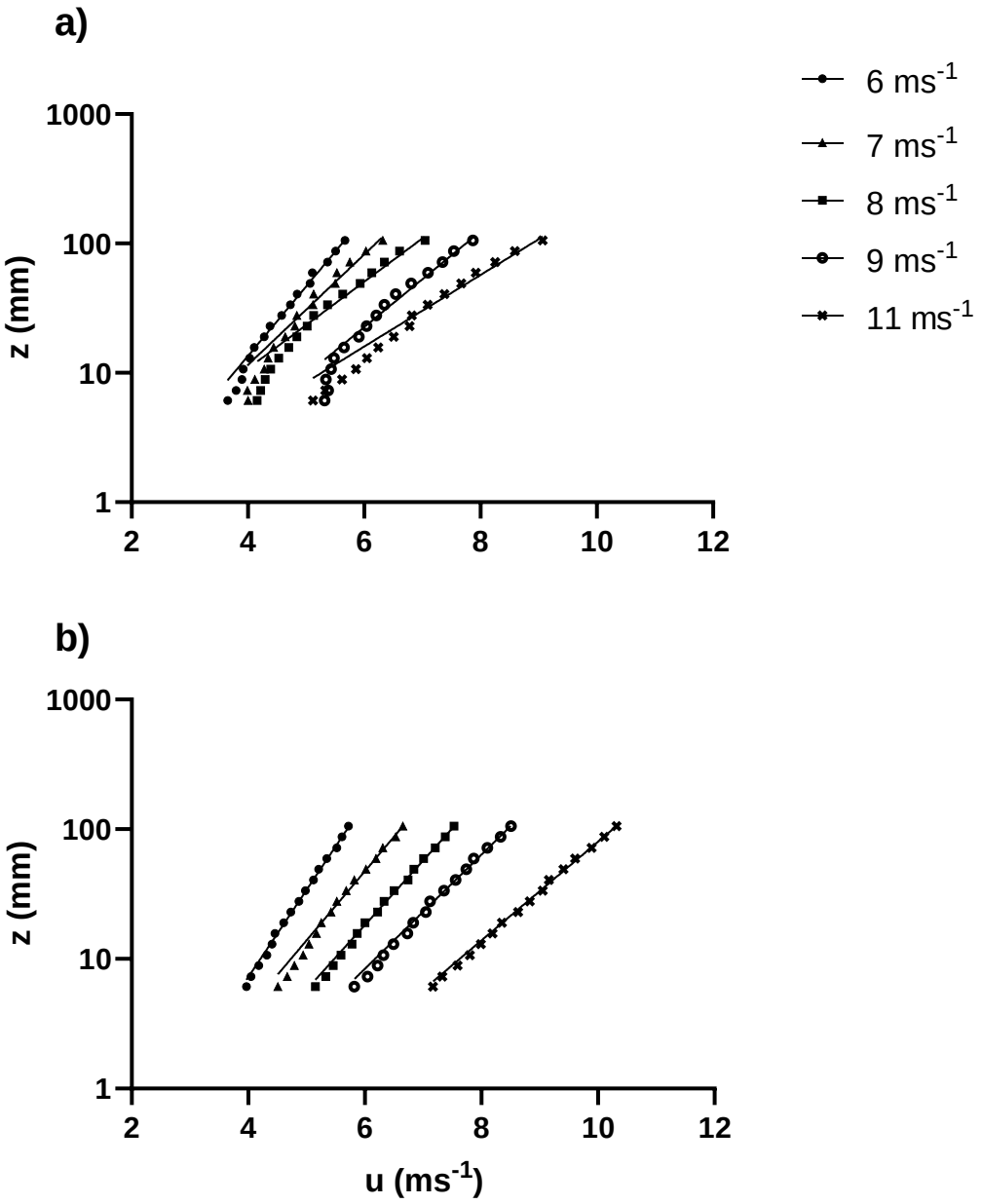

Figure 2.8: a) Average velocity profiles over a dry bed at each requested freestream velocity representative of Exp 1. b) Average velocity profiles over a wet bed, with no saltation representative of the conditions present in Exp 2. Each profile is the average of 5 replicates at Pitot Z.

2.8 Limitations

Due to the difficulty of the execution of these experiments, this study was limited in the number of experiments that could be conducted within a reasonable length of time for a MSc thesis. Only one replicate at each moisture content during experiment 1 was feasible. The time requirement to fill and empty the working section of the wind tunnel at temperatures reaching -10 ºC was considerable. To avoid waste, some of the uncontaminated sand was reused from experiment to experiment. In most cases, this sand needed extended periods to unfreeze and dry, delaying experimentation. Cooling a lab of this size further complicates the execution of these experiments. The lab needed to be left overnight to equilibrate at the desired temperature for the experiment. Technical difficulties were faced throughout the project as well. Delays occurred due to the humidifier kettle and the refrigeration unit requiring servicing. The instrumentation used during these experiments was not engineered to work in cold environments so careful calibration was required to ensure their functionality. Further, during experiment 1, the LDA processor failed resulting in the redesign of experiment 1 to include the tracer method and the extension of the thesis to include experiment 2. Finally, the dust experiments were also limited by the supply of dust available. The sand sample was assumed to have a significant dust portion within it. The actual quantity of dust remains unknown. To avoid the depletion of this portion and ensure that there would be enough dust available, new sand was used to replenish the bed. This further limited the replication of the experiment.

Chapter 3: Experiment 1 Results and Discussion

This section presents the results of experiment 1 ordered by instrument, followed by the presentation and discussion of the results.

3.1 Dry Bed Transport Experiment

3.1.1 Effect of temperature on the mass transport rate

This section is concerned with understanding the effect of temperature on mass transport rates over loose, dry beds. Transport events were simulated across a 40°C temperature range and included measurement of the saltation cloud intensity and height and the mass transport rate (Q).

Figure 3.1 plots Q, calculated using the cumulative mass data collected by the passive sand trap, against the averaged air temperature measured at 350 mm above the bed at the time of the run. The slope of each regression line is significantly different from 0 (Table 3.1). For all three friction velocities, there is a 22-23% linear increase in mass transport rate with falling temperature between 30°C and -12°C at both 35% and 58% relative humidity. Relative humidity does not seem to be a major control of saltation and the mass transport rate. Further evidence into the lack of humidity's effect on saltation is shown in Appendix D where Q is plotted against the matric potential. However, in nature, relative humidities beyond this range are commonly found and may produce an effect on saltation.

3.1.2 Effect of temperature on the saltation cloud height

Figure 3.2 displays the data from the vertical array of laser sheet sensors which measured saltation intensity as inferred from the proportion of the laser sheet intercepted. In the low relative humidity runs, there appears to be a slight increase in saltation intensity with decreasing temperature. At 1.1 cm above the surface, the proportion of the beam blocked increases by 22%, 23%, and 16% from 30 to -12^{o}C at u_* of 0.35, 0.55, and 0.72 ms^{-1} respectively. However, during the high humidity runs, this trend is not seen. The only similarity is that the 30^{o}C run has the lowest saltation intensity, suggesting that the presence of water vapour within the system, complicates these processes. Using the associated regression equations reported in Table 3.3, the change in the height of the saltation cloud with temperature can be evaluated. The y-intercept is assumed to be the height at which the laser sheet's beam is no longer intercepted; the top of the saltation cloud. Figure 3.4 plots the y-intercept for each curve for the low-humidity runs. The lowest windspeed has a slope of 0 whereas the two highest windspeeds exhibit a weak negative relationship between the y-intercept and temperature that is also not significantly different from 0 (Table 3.2). The height of the saltation cloud does not appear to increase with decreasing temperature leading to the rejection of hypothesis 1. Similar results are found when comparing the saltation cloud height to the matric potential, indicating that there is no relationship between saltation cloud height and humidity. These plots are found in Appendix E

Having conflicting evidence that mass transport increases and saltation cloud height remains unchanged with decreasing temperature, the next section investigates how

this impacts dust emissivity across the same range of temperatures, as saltation is the main driver of dust emission.

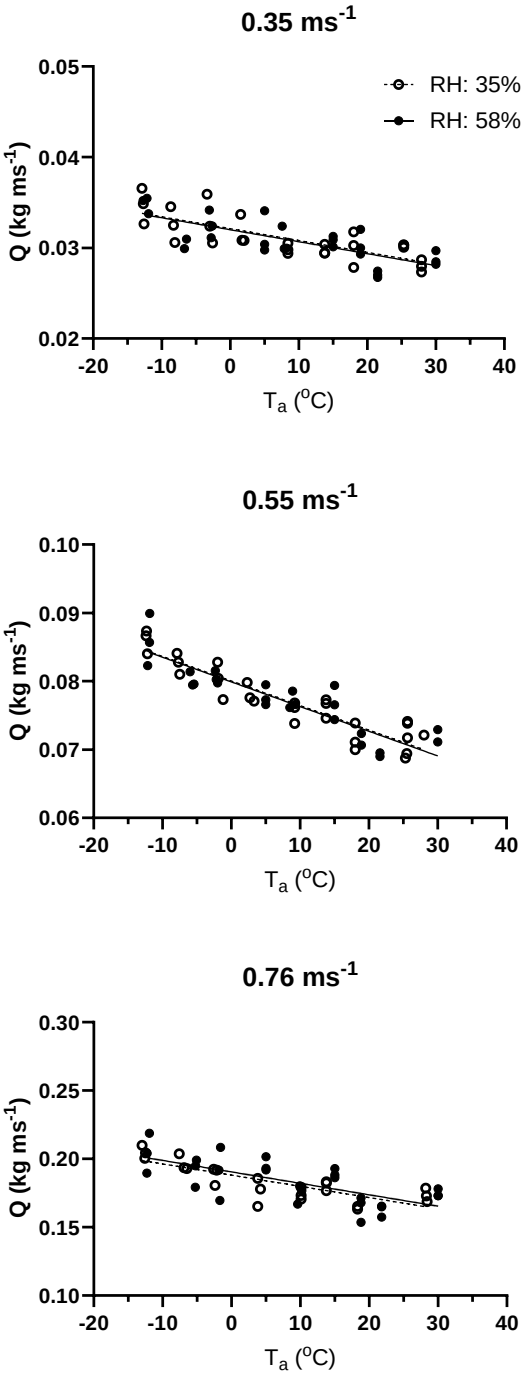

Figure 3.1: Mass transport rate was calculated for a 3 min transport simulation. Three test replicates were conducted at each temperature. The Y-axes are adjusted to properly display each trend while accounting for differences in magnitude

Table 3.1: Regression statistics for plots (a), (b), and (c) in Figure 3.1.

	Low RH				High RH			
	Slope	**Value at 0°C**	**R^2**	**P-Value**	**Slope**	**Value at 0°C**	**R^2**	**P-Value**
a)	-1.3×10^{-4}	0.032	0.59	<0.0001	-1.3×10^{-4}	0.032	0.55	<0.0001
b)	-3.6×10^{-4}	0.080	0.85	<0.0001	-3.6×10^{-4}	0.080	0.79	<0.0001
c)	-8.2×10^{-4}	0.188	0.64	<0.0001	-8.4×10^{-4}	0.191	0.47	<0.0001

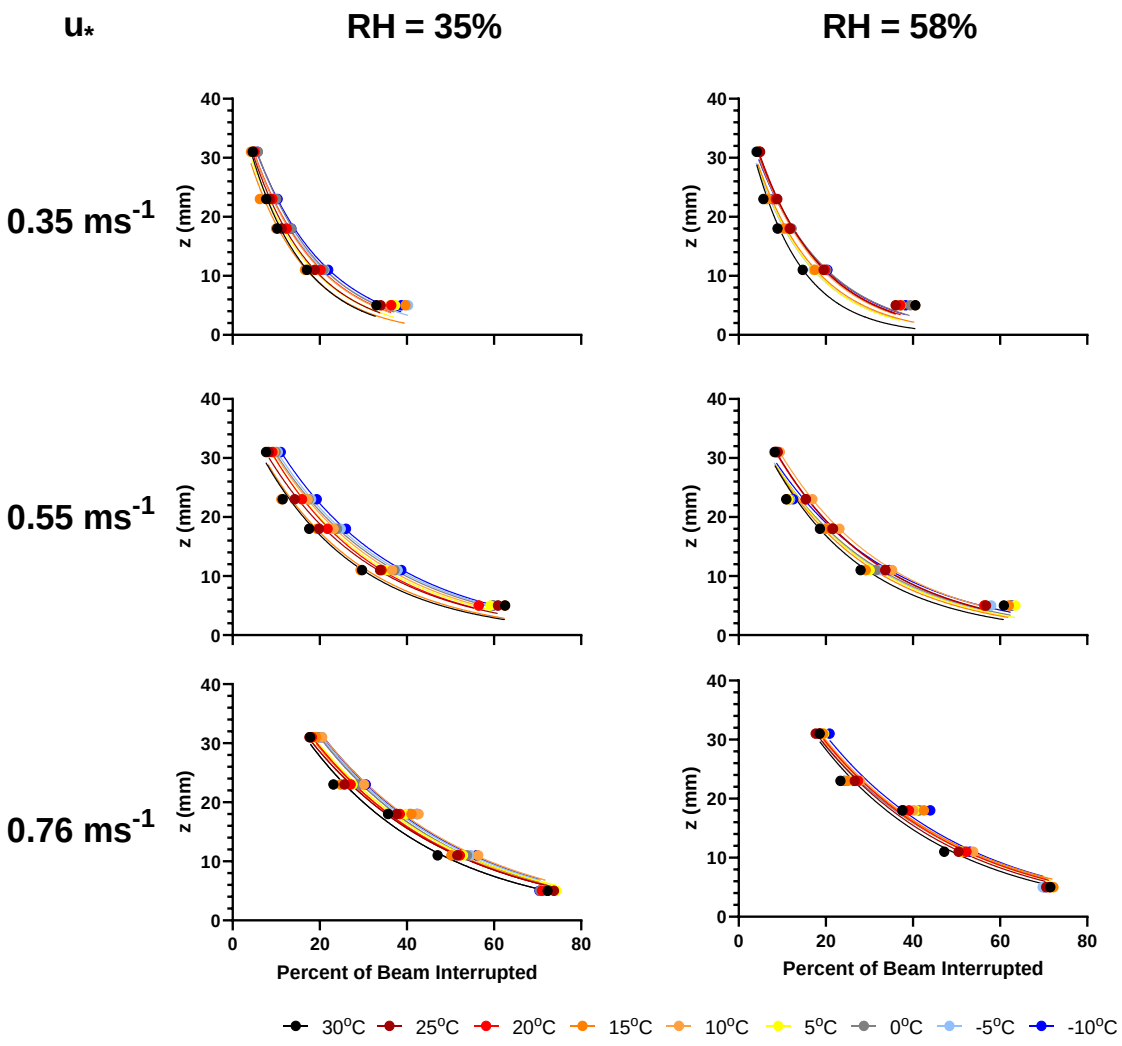

Figure 3.2 Vertical saltation intensity profile measured by the Keyence™ laser sheet sensors.

Table 3.2: Y-intercept and exponent for each curve in Figure 3.2. The general form of the relation is $z = y_0 e^{kx}$ where: z = height above bed, y_0 = y-intercept, k = rate constant, and x = % of beam interrupted.

RH = 35%						
u_*	0.35		0.55		0.76	
T	y-int.	Exponent	y-int.	Exponent	y-int.	Exponent
30°C	43.48	-0.08014	40.88	-0.04394	53.66	-0.03289
25°C	42.87	-0.07214	44.57	-0.04085	54.48	-0.03085
20°C	42.83	-0.06662	40.87	-0.04262	53.50	-0.03032
15°C	40.00	-0.07612	46.87	-0.03712	58.07	-0.0301
10°C	42.73	-0.06704	41.96	-0.04006	52.30	-0.03022
5°C	40.39	-0.07022	44.79	-0.03879	57.69	-0.02977
0°C	44.88	-0.066	43.72	-0.03927	53.84	-0.02975
-5°C	41.26	-0.06266	44.69	-0.03763	57.60	-0.03095
-10°C	43.74	-0.0624	45.36	-0.03719	57.22	-0.03014
RH = 58%						
u_*	0.35		0.55		0.76	
T	y-int.	Exponent	y-int.	Exponent	y-int.	Exponent
30°C	41.96	-0.09065	41.94	-0.04553	54.38	-0.03258
25°C	42.58	-0.0687	44.17	-0.04096	54.08	-0.03125
20°C	41.75	-0.06737	43.91	-0.04098	54.67	-0.03063
15°C	39.93	-0.07274	40.80	-0.04219	52.92	-0.02943
10°C	41.92	-0.06933	45.01	-0.03965	54.62	-0.03004
5°C	40.04	-0.07522	40.98	-0.04128	55.14	-0.03086
0°C	40.13	-0.06379	40.30	-0.03969	52.33	-0.02972
-5°C	39.06	-0.07398	40.64	-0.04067	52.56	-0.02989
-10°C	39.93	-0.06406	40.35	-0.03751	56.06	-0.03011

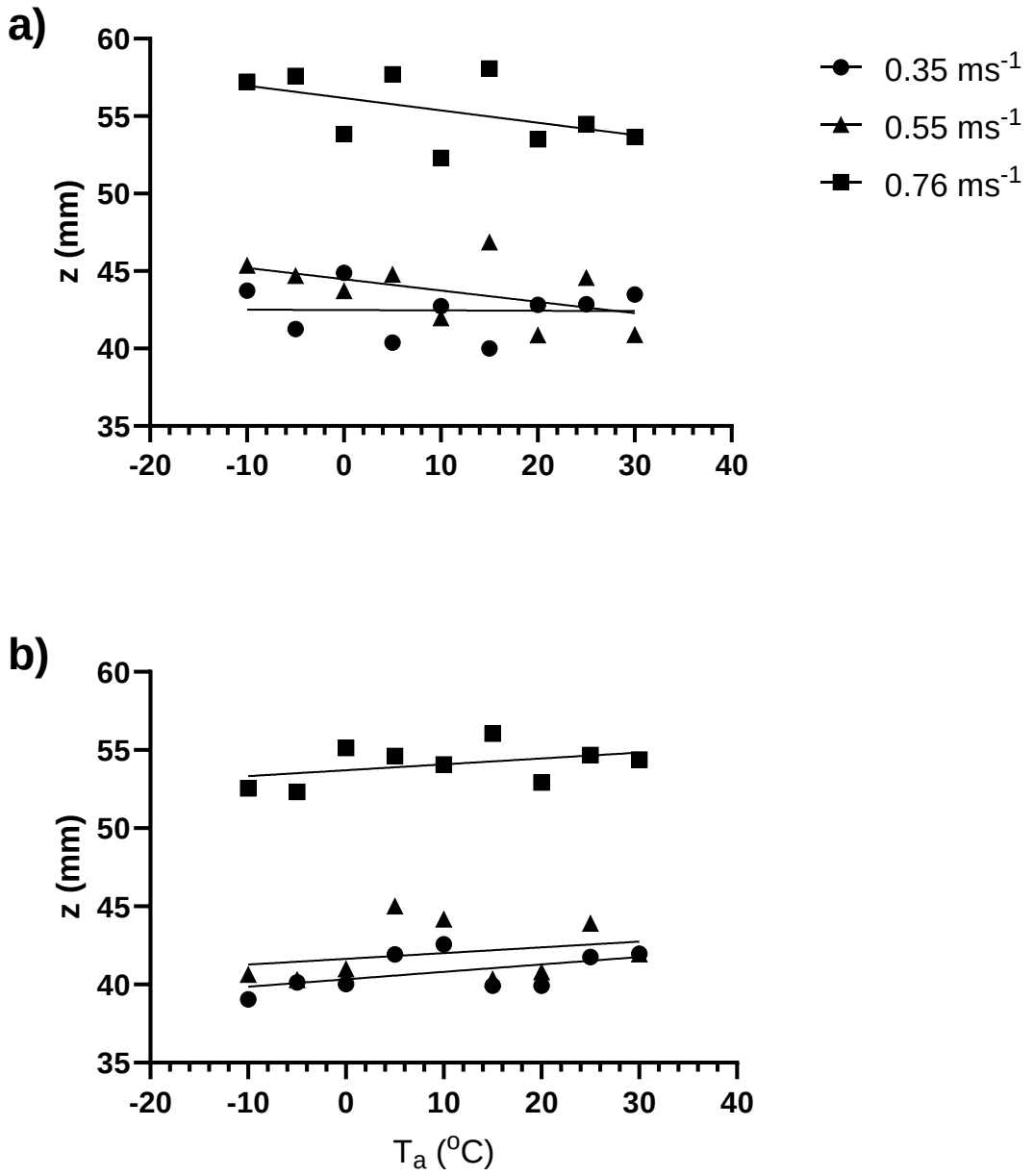

Figure 3.3: Y Intercept of each curve in Figure 3.2 plotted against temperature. Graph a) represents the low humidity runs and b), the high humidity runs. The Y-intercept is assumed to be the height at which the laser sheet will no longer record particle motion which is a proxy for the height of the saltation cloud. Any change in saltation cloud height across all runs, cannot be explained by a change in temperature.

Table 3.3: Regression statistics for Figure 3.4. None of the slopes are statistically different from zero.

	u_* (ms^{-1})	Slope	Intercept	R^2	P-Value
a)	0.35	-2.3×10^{-6}	0.042	0.00	0.9595
	0.55	-7.3×10^{-5}	0.044	0.23	0.1910
	0.76	-8.0×10^{-5}	0.056	0.23	0.1831
b)	0.35	4.8×10^{-5}	0.040	0.28	0.1459
	0.55	3.8×10^{-5}	0.042	0.07	0.4794
	0.76	3.8×10^{-5}	0.054	0.17	0.2696

3.1.3 PM_{10} dispersion over mobile beds

To test the hypothesis that vertical dust fluxes over a bed of dry sand will increase with decreasing temperature, TSI DustTraks measured the PM_{10} concentration at three heights above the bed surface (0.10, 0.25, and 0.30 m). The average PM_{10} concentration data (Figure 3.4) at each of the heights show a decreasing PM_{10} concentration and decreasing variability in PM_{10} concentration with increasing height above the bed, as characterized by an exponential decay. Dust emission and dispersion is a highly stochastic process resulting in order of magnitude variation. The concentration data show no discernable relationship with temperature. Using the average dust concentrations (c_1 and c_2) at 0.25 (z_1) and 0.30 m (z_2) above the bed, the vertical dust flux was calculated using the finite difference method. These two sampling locations were chosen from the three possible heights as the DustTrak intake at the lowest height (0.10 m above the bed) was inundated with sand throughout the experiments resulting in high variability and less reliable measurements. The vertical dust flux is a measure of dust emission. Equation (8) below was used to calculate the vertical dust flux (V_f, mg m^{-2} s^{-1}).

$$V_f = \frac{-ku_*(c_1 - c_2)}{\ln\left(\frac{z_2}{z_1}\right)} \quad \text{(Equation 8)}$$

V_f was then divided by the saltation rate (Q, mg m^{-2} s^{-1}) for each run, providing a dimensionless index that isolates the effect of decreasing temperature on dust emission and dispersion from that associated with ballistic entrainment through saltation. Figure 3.5 plots each of these normalized dust flux values against air temperature. These plots show Q adjusted for the height of the saltation cloud but u_* is not adjusted for the associated roughness as affected by changing temperature. However, V_f is strongly affected by u_*. Except for 3 outliers in plot (b) across the three windspeeds, $V_f < 0.4$, and V_f does not appear to be directly affected by either temperature or relative humidity. Independent of saltation, no trend of increasing dust flux with decreasing temperature is present. The effect of an increase in saltation on dust emission dominates this system and any effect of increased air density or decreased viscosity on the dispersion mechanisms (e.g. turbulence structures) would seem to be minimal in comparison.

Similar to the mass transport data, there is no separation between the high relative humidity and low relative humidity runs. On the other hand, matric potential (ψ) is an indicator of the strength of interparticle binding within a system (Equation 5 and 6). For the low humidity runs, -1.5×10^2 MPa $< \psi < -1.3\times10^2$ MPa whereas the range for high humidity runs was, -76 MPa $< \psi <$ -66 MPa (Appendix F). A two-sample t-test assuming unequal variances was run to test for a significant difference between the mean V_f/Q of the low-humidity runs and the high-humidity runs. With a t-statistic of 1.253 and a two-tailed t-critical value of 1.980, the null hypothesis of equal means is supported. Despite

there being an order of magnitude difference in the matric potential between low and high humidity runs, the vertical dust flux would not appear to be dependent on matric potential for the experimental conditions considered. As such, hypothesis (3) cannot be accepted as the vertical dust flux was not found to be dependent on temperature or humidity but is dependent on the saltation rate.

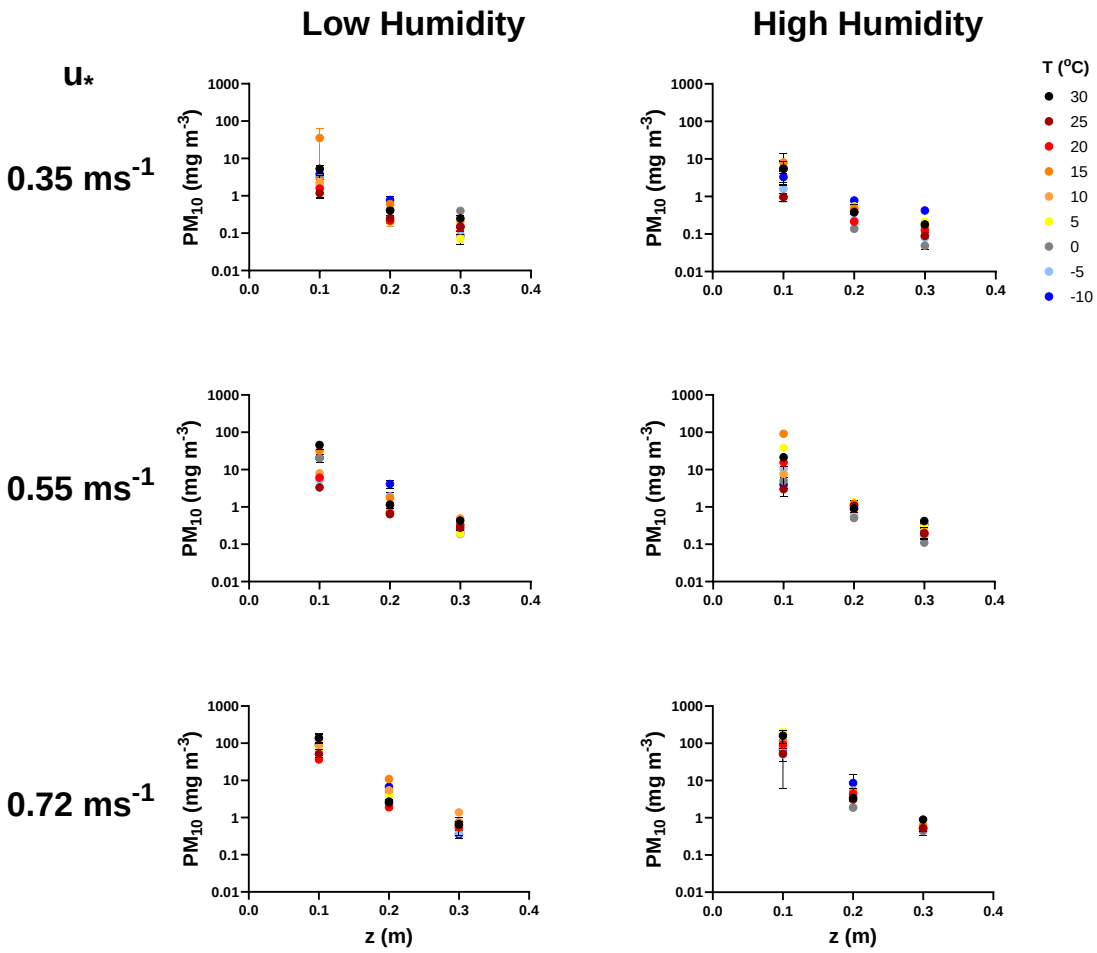

Figure 3.4: Raw dust concentration data at each of the three elevations after having subtracted the background dust concentration measured at the wind tunnel intake.

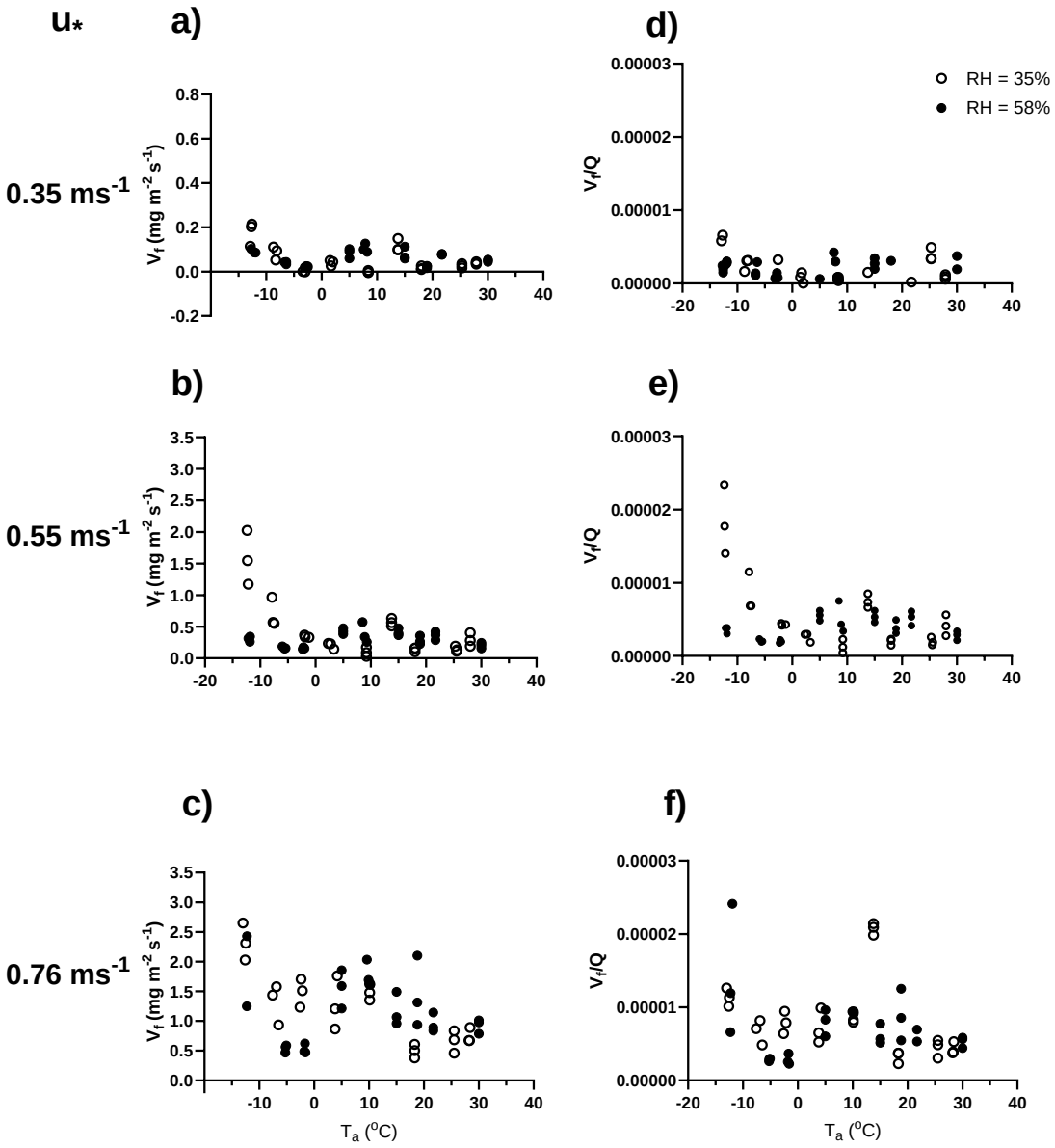

Figure 3.5: Dust flux versus temperature (plots a-c) and normalized dust flux versus temperature (plots d-f) at each u* setting.

3.2 Discussion

3.2.1 Effect of temperature on mass transport rate

The Guelph-Trent sediment trap is an instrument that directly measures Q through sampling the real-time cumulative mass transport. A strong negative relationship (R^2 values ranging from 0.47 to 0.85) was found between Q and temperature at both relative humidities suggesting that Q is dependent on T but not relative humidity (Figure 3.1). This trend is in agreement with results from previous wind tunnel experiments and field work and also challenges model predictions.

One study from McKenna Neuman (2003), measured the threshold wind speed of four grain sizes at temperatures ranging between 32°C to -12°C. The results of scale data suggest that it is easier for cold air to entrain sediment and indeed larger particles than warm air. This earlier work corresponds to what has been shown in this study, whereby more sediment was entrained at lower temperatures over dry surfaces. McKenna Neuman (2004) built on this study by measuring mass transport rates over dry beds at a temperature range of -9°C to 32°C. She observed a 32% increase in Q with decreasing temperature. This is higher than the 19-23% increase in Q observed in this study. Using extrapolation, she predicted a 70% increase in Q over an 80°C temperature range. This is higher than the more conservative 28-30% increase calculated from the regression equation from Experiment 1. Differences in methodology could explain these differences. In her discussion, McKenna Neuman suggests that because the effects of density and viscosity balance each other out, as discussed in Chapter 1 of this thesis, changes in the drag force are not responsible for this increase. This present study suggests that relative humidity may not be the cause either as there is no separation between the regression

lines at 35% and 58% humidity. Further research must explore this relationship across a wider range of relative humidities.

Fieldwork in Arctic regions is very challenging due to extreme conditions and any work that has been done is coarse and fragmented (Lancaster et al., 2010), yet the results from this thesis support some findings from fieldwork. A benchmark study from McKenna Neuman (1990) looked at the changes in sediment transport within Pangnirtung Pass, Baffin Island year-round. She found that sediment transport was significantly greater in the winter months than in the summer months, due to stronger katabatic drainage and dry conditions in the winter while the summer was characterized by high precipitation, flooding and replenishment of local sediment source areas, and low evaporation rates. More recent work, by Stout (2003), and Yang et al. (2013, 2017) monitoring saltation fluxes over a saline playa in Northwest Texas, and the Taklimakan Desert respectively, confirm that favourable atmospheric conditions in the winter lead to greater saltation fluxes. They concur that lower temperatures result in lower threshold velocities, theoretically allowing for more sediment transport. However, each note that the various conditions that affect threshold and their interactions are complicated, and other factors may be at play. Gillies' et al. (2013) for example, monitored saltation over the course of two years in a dry valley in Antarctica. Their field measurements did not provide evidence to suggest decreasing temperatures affect threshold but rather high-speed, seasonal foehn winds are responsible for greater saltation fluxes in winter.

Saltation models indirectly account for temperature and relative humidity through the incorporation of air density (ρ). The effects of other variables such as surface hardness or moisture are represented by a lumped or "blackbox" parameter, c_o. These

models predict an increase in Q with decreasing temperature as this trend is a product of the increase in air density with decreasing temperature. Because of this, the models in Table 3.4 predict a 13-15% increase in Q across the temperature range used for this experiment. However, the regression equation from Table 3.1 suggests a slightly larger increase of 18-20%. This may be due to the various factors that remain unaccounted for by the experimental design. For example, electrostatic forces were not measured. This interparticle force was noticeably stronger with decreasing relative humidity due to the "sticking" of particles to the device used to level the bed surface, however its effect could not be isolated by the experimental design. Moreover, the turbulence within the flow was not measured, which is expected to increase with decreasing temperature due to an increase in the dynamic viscosity.

Table 3.4: Table of models to evaluate Q, as per Shao (2008). These models carry with them varying assumptions, including spherical, uniformly sized, and shaped particles, that particle motion is two-dimensional and that particle motion is repetitive (same trajectories, independent of time).

Source	Expression	Parameter
Bagnold (1937)	$c_o(\frac{d}{D})^{1/2}\frac{\rho}{g}u_*^3$	$D = 250\ \mu m$ $c_o = 1.5$, uniform sand $c_o = 1.8$, natural graded sand $c_o = 2.8$, poorly sorted sand
Zingg (1953)	$c_o(\frac{d}{D})^{3/4}\frac{\rho}{g}u_*^3$	$c_o = 0.83, D = 250\ \mu m$
Kawamura (1964)	$c_o\frac{\rho}{g}u_*^3(1-\frac{u_{*t}}{u_*})(1+\frac{u_{*t}}{u_*})^2$	$c_o = 1.8\ to\ 3.1$
White (1979)	As Kawamura (1964)	$c_o = 2.6$
Owen (1964)	$c_o\frac{\rho}{g}u_*^3(1-\frac{u_{*t}^2}{u_*^2})$	$c_o = 0.25 + \frac{w_t}{3u_*}$
Lettau and Lettau (1978)	$c_o\left(\frac{d}{D}\right)^{1/2}\frac{\rho}{g}u_*^3(1-\frac{u_{*t}}{u_*})$	$c_o = 4.2$

3.2.2 Effect of temperature on saltation cloud height

Saltation intensity profiles were created (Figure 3.2) using the data from the vertical array of Keyence^{TM} laser sheet sensors. Both numerical and experimental studies have shown that the particle concentration decays exponentially with height (Dong, Wang, Zhang, et al., 2004). Other works have shown that particle concentration decays exponentially with the square root of height (Dong et al., 2006) or follows a power function (Shao, 2008). Exponential curves were fit to the points in Figure 3.2 and the saltation cloud height was assumed to be the y-intercept. Figure 3.3 plots the saltation cloud height against temperature and a regression analysis shows that the slopes of these lines are not statistically different from zero, warranting the rejection of Hypothesis 1. Although the height of the cloud would not appear to be affected by temperature, the saltation intensity profile is affected, though not consistently. At low relative humidity (35%) at $u_* = 0.35$ and 0.55 ms^{-1}, an increase in saltation intensity with decreasing temperature is seen.

The lack of change in saltation cloud height is consistent with the argument that the drag force during flight is unchanged.

The results from the optical (Keyence) sensors do not agree with those from the Guelph-Trent sediment trap in suggesting that temperature does not affect saltation cloud density and height. It is well known that >90% of the saltation cloud is contained below 10 mm of elevation (O'Brien & McKenna Neuman, 2018, 2023). The lowest sampling point for the laser sheet array was 5 mm above the bed surface, limiting measurement to well under 50% of the saltation cloud. Further, the laser sheet output is given as a voltage providing an indirect measure of saltation intensity. The sediment trap however, collects

particles travelling in creep, reptation and saltation, collecting a representative sample of particles and providing a direct measurement of the total mass transport (kg ms^{-1}).

Numerical models for both the saltation cloud height (Owen, 1964) and the saltation flux profile (Gillette et al., 1997; Raupach & Shao, 1992) account for temperature and relative humidity indirectly through the incorporation of fluid density as well as model parameters which must be calibrated using empirical data. Considering the lack of agreement observed in the present study, further experiments should use direct measurement only, perhaps using a slot trap.

3.2.3 Effect of temperature on dust flux

Dust dispersion is a substantially more stochastic process than sand transport resulting in large variations in the dust concentration profiles measured above the surface (Fig. 3.4). There is an order of magnitude increase in the dust concentrations at 0.2 m and 0.3 m above the surface between 0.35 ms^{-1} and 0.76 ms^{-1}. This is seen in the vertical dust flux across both relative humidities as well. Due to the consistent range in V_f across all temperatures and wind speeds, there is no discernable relationship with temperature or at least none that can be detected due to the natural noise within the system or due to the limited number of replications.

The measured PM_{10} concentrations are of the same magnitude as the dust concentrations coming off of a bed of pulverized mine tailings with 60% of particles below 100 μm (McKenna Neuman et al., 2009). However, said experiment used a 26.5 cm x 16 cm strip of material, 2.5 cm deep.

However, when looking at vertical dust flux, the values presented in this study do not compare well to both lab and field studies. The aforementioned study from McKenna Neuman et al. (2009) looking at fugitive dust emissions on mine tailings report a dust flux of 0.5 – 2.0 mg m^{-2} s^{-1} at $u_* = 0.56$ ms^{-1} for small trays of slurry material which is comparable to the V_f at 0.76 ms^{-1} in this study. Sweeney et al. (2008) report a dust flux of 0.1 mg m^{-2} s^{-1} at $u_* = 0.56$ ms^{-1} mud cracked surfaces of lacustrine sediments. This is similar to the values reported at 0.55 ms^{-1} in this study. Many natural soils such as disturbed silt and loam from Owens lake are an order of magnitude more emissive (Roney & White, 2006).

Shao and Lu (1999) concluded that V_f is proportional to u_*^{n+1} where n = 2 or 3; 2 for hard surfaces and 3 for soft surfaces. By plotting the average V_f across all temperatures against windspeed, the present study considers V_f to be proportional to $u_*^{4.4}$. arlier work from Shao et al., (1993) investigated the relationship between V_f and Q for soils of varying grain sizes. The ratio of V_f/Q at for this study is not comparable to that measured by Shao et al. (1993) for their 100-210 μm diameter soil which likely contains far more dust than the material used for this study (<0.03 in this study compared to 0.25)

The PM_{10} concentration within this material might come from dust coats that are released as particles are abraded during transport, limiting the amount of measurable dust during the run.

Chapter 4: Experiment 2 Results and Discussion

4.1 Dry, Wet, and Frozen Bed Transport Experiment

4.1.1 Temperature measurement

In this investigation, temperature was sampled at four locations throughout each experiment, inclusive of the room temperature, the temperature of the air 1 cm above the bed, at the bed, and at the base of the test bed. The room temperature was recorded during each 120-second run, when the fan was on. This is because when the air in the lab is stagnant, it stratifies. Once the fan turns on, the air within the lab begins to mix and equilibrate. The most representative air temperature readings are measured a few minutes following the startup of the wind tunnel fan. Figure 4.1 provides a time series plot showing the change in temperature during the full, low surface moisture experiments at each room temperature setting. Noticeably, the air temperature demonstrates some degree of periodicity. This is due to the climate system cycling when the room temperature drops or rises 1°C. The air temperature is engineered to remain within ±1°C of the desired value. The run at -3°C shows a small continuous drop in temperature over time. Beginning this experiment before attaining equilibrium within the room resulted in this trend. Utilizing a thermocouple setup that displays this information in real time would have allowed for more accurate timing of the experiments. Table 3.5 displays the average temperature and standard deviation for each measurement location during each set of runs. This confirms that the temperatures during each run are within ±1°C of the target value. For example, the warm runs, above 0°C are consistently around 3°C ± 1°C. Considering that this was a large-scale experiment, where attaining a high degree of precision with temperature is difficult, the vertical temperature gradients are well

constrained. The warm run's target temperature was 5°C, however, an average temperature of only 3°C was achieved. This was due to an operator error while monitoring the thermocouple's datalogger. Fundamentally, this is not problematic as a one-way ANOVA confirms a significant difference in mean temperature 10 mm above the test bed for the three nominal experimental conditions (i.e. T above, at and below the freezing point of water).

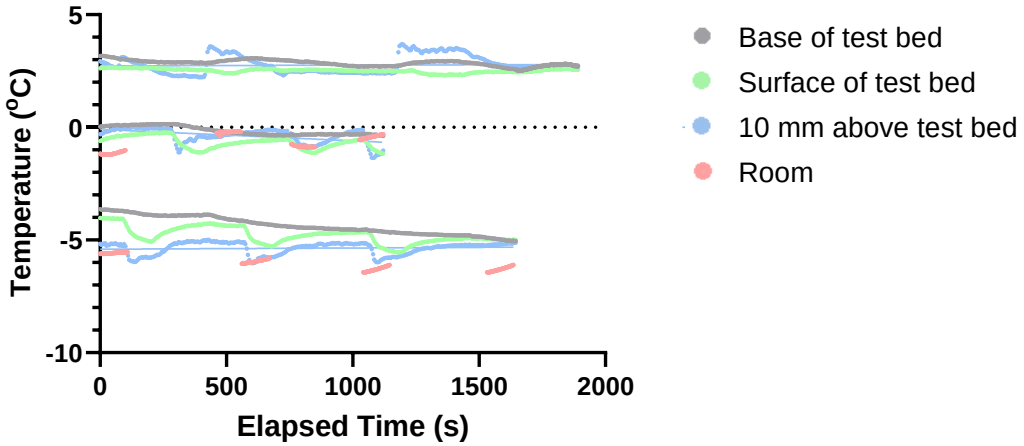

Figure 4.1: Example time series of temperature change at four separate sampling points: the wind tunnel floor (Floor), at the bed surface (Surface), 1cm above the bed surface (Air), and the room temperature (Room) during the 6 ms^{-1}, low surface moisture run. The 0°C run is shorter as there was an extra lab assistant assisting with the execution of the experiment.

Table 4.1 Time-averaged temperature and standard deviation at each sampling location based on binned data for test replicates. The temperature measurements around the test bed are averages over the entire period in which all tests were run. The room temperature averages the temperature of a series of 120-second tests.

Target Temperature (°C)	3		0		-5	
	Mean	St. Dev.	Mean	St. Dev.	Mean	St. Dev.
Base of Test Bed	2.60	0.55	-0.75	0.69	-5.23	1.18
Surface of Test Bed	2.63	0.90	-0.92	1.37	-5.18	1.04
10 mm above Test Bed	2.97	1.30	-0.53	1.10	-5.63	0.78
Room	3.39	1.00	-0.57	0.92	-5.47	0.39

4.1.2 Fetch effect

The second set of experiments involved the addition of water to the bed surface. For this analysis, the gravimetric moisture content of the surface grains was the primary descriptor of the bed's water content, given that it was directly in contact with the saltation cloud. Once the bed was sprayed, water adhered to the surface of grains and filled the surrounding pores, binding them together strongly. Little is known about the effect of pore water on the fetch effect and changes in the mass transport rate with temperature. Pore water and ice bind particles together with forces much greater than the electrostatic forces that bind dry particles together (Kok et al., 2012). This is expected to affect the fetch or the distance at which the saltation cloud reaches steady-state. Over the dry beds, there should be little to no change in the saltation intensity with distance downwind, as the saltation cloud should saturate within the first 2 meters of the bed (Dong, Wang, Liu, et al., 2004). However, when moisture is added, the particles do not have enough momentum to eject a large quantity of particles bonded strongly by cohesion. Perched or weakly bonded particles can be ejected and be added to the saltation cloud, increasing its density and in turn, may fracture or abrade the damp or frozen

surface to an extent that further grains may be entrained. This abrasion process is dependent on the intensity and the duration of the bombardment, with the intensity building over the distance of transport (fetch) in this cascading system.

A key feature of aeolian transport over a dry surface is the overshoot of saltation. The onset of saltation is dominated by aerodynamic processes. These saltating particles eject more particles into the air through splash. Entrainment through particle bombardment quickly begins to dominate the system, initiating a rapid fetch dependent growth in Q. As more and more particles are entrained into the air, the partitioning of fluid momentum to the saltation cloud reduces the windspeed near the bed, resulting in a slight drop in Q as it adjusts toward an equilibrium state further downwind (Shao & Raupach, 1992).

To examine the fetch effect under varied surface conditions, Keyence^{TM} laser sheet sensors were installed approximately every 2 m along the bed of the tunnel. Figure 4.2 displays a very slight overshoot for the dry beds, as there is a consistent increase in saltation intensity in moving from the first sampling point to the second, followed by a downwind decrease. This pattern is not apparent for the dampened beds. As expected, saltation intensity also increases with higher wind speeds during the dry runs. With the addition of water, however, the saltation intensity decreases by 50-75% across all runs. The generally positive slope of the associated regression lines would appear to indicate the progressive ejection of particles from the bed surface with increasing fetch, despite the presence of strong interparticle bonds. The only exception is for runs with high moisture content at 3^{o}C ($0.28 < u^* < 0.36$ ms-1) wherein the saltation intensity decreases with the fetch distance. In this case, saltators delivered from the upwind feed may have

largely adhered to the wet, 'sticky' surface. The mean saltation intensity is only significantly different for the dry runs. Table 4.2 provides some evidence of the flux rate increasing with decreasing temperature over these surfaces, particularly for low velocities. This is in agreement with the trend of decreasing mass transport rates with temperature from experiment 1 (Figure 3.1) and supports the hypothesis that fewer particles can be ejected from frozen beds than warm dry beds. ANOVA testing concludes that at $u_* = 0.21$ ms^{-1} there is no significant difference between the mean saltation intensity for beds with moisture across the 8^{o}C temperature range. At higher velocities, the state of water in the pore spaces seems to affect saltation intensity at low moisture contents whereby an increasing proportion of pore ice to liquid water results in a decreasing saltation intensity.

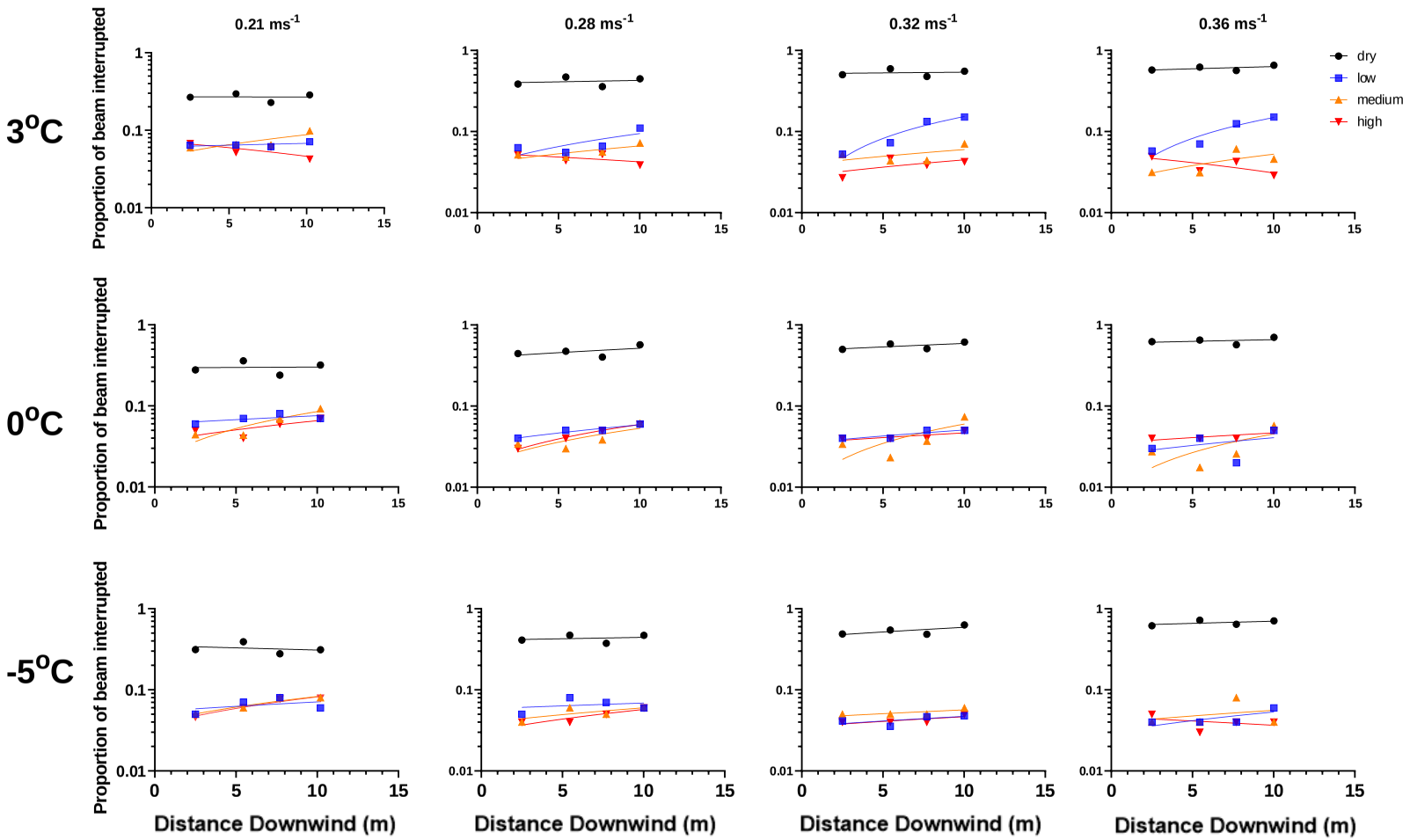

Figure 4.2: Fetch variation in saltation intensity at each of the floor-mounted Keyence™ laser sheet sensors. Saltation intensity is not given in scalable units but rather in terms of the percent decrease in voltage in response to the saltators blocking portions of the laser sheet.

Table 4.2: The average proportion of the beam interrupted and slope of the regression line for each temperature and moisture setting. Slopes denoted as "ns" are not significantly (95% confidence level) different from zero.

u_* (ms^{-1})		0.21			0.28			0.32			0.36		
T (°C)	Water Content	Mean	Slope	Sig	Mean	Slope	Sig	Mean	Slope	Sig	Mean	Slope	Sig
3	dry	0.269	0.000	ns	0.134	0.003	ns	0.532	0.002	ns	0.605	0.008	ns
	low	0.065	0.001	ns	0.033	0.006	ns	0.102	0.014	s	0.101	0.013	s
	medium	0.072	0.005	ns	0.038	0.003	ns	0.052	0.002	ns	0.042	0.003	ns
	high	0.056	-0.003	ns	0.026	-0.001	ns	0.039	0.002	ns	0.038	-0.002	ns
0	dry	0.299	0.001	ns	0.473	0.012	ns	0.552	0.011	ns	0.637	0.006	ns
	low	0.070	0.002	ns	0.050	0.002	s	0.045	0.002	ns	0.035	0.002	ns
	medium	0.062	0.007	ns	0.041	0.003	ns	0.042	0.005	ns	0.032	0.004	ns
	high	0.055	0.003	ns	0.045	0.004	s	0.043	0.001	ns	0.043	0.001	ns
-5	dry	0.323	-0.004	ns	0.432	0.004	ns	0.538	0.015	ns	0.673	0.008	ns
	low	0.065	0.002	ns	0.065	0.001	ns	0.043	0.001	ns	0.045	0.002	ns
	medium	0.068	0.004	ns	0.053	0.002	ns	0.053	0.001	ns	0.050	0.002	ns
	high	0.066	0.005	s	0.048	0.003	ns	0.043	0.001	ns	0.040	-0.001	ns

4.1.3 Particle total velocities

So far, the results suggest that particles impacting cohesive, brittle, and frozen beds are less likely to eject particles from the surface than over a dry bed. Therefore, they should retain more of their momentum as they move downwind. Having more momentum, they should move at higher velocities since the mass of the particle is constant ($p = m \times u$). Similarly, they should travel in higher, longer ballistic trajectories, so that the frequency of impact on the bed surface will decline. Measuring particle velocity can provide insight into the momentum partitioning that occurs during saltation over surfaces of varying moisture content.

The velocity components of sand particles sampled at six heights above each test surface were measured using an LDA. During the 20-second sampling period, between 150 and 10,000 particle velocities were sampled at each height. Such a large sample size ensures a high degree of accuracy. The average total particle velocity at each height then was calculated and plotted in vertical profile, as shown in Figure 4.3.

The profiles demonstrate an increase in particle velocity with height above the bed surface, while the difference between the average total particle velocity for the dry versus wet bed runs increases with increasing wind speed. Indeed, a stark difference in particle velocity exists between dry beds and surfaces with low moisture content, suggesting that any amount of added moisture will result in a substantial increase in particle velocity at all heights above the bed. As shown in Figure 4.3, the highest particle velocities were measured for runs with the highest friction velocities (0.32 and 0.36 ms^{-1}) and gravimetric moisture contents. At 0.21 and 0.28 ms^{-1}, the mean particle velocities over beds of low, medium, and high moisture content are not statistically different. In

general, saltators have velocities 3-4 times greater over wet or frozen surfaces than over dry surfaces, regardless of the wind speed. Given that a particle's kinetic energy is proportional to the square of its velocity, it may saltate over wet or frozen surfaces with 9-12 times more kinetic energy than over a dry bed.

The high degree of overlap between the particle velocity profiles shown in each subplot in Figure 4.3 further shows that for any bed surface containing any amount of water, the influence of temperature is negligible while windspeed is the primary governing factor. Supporting statistics are provided in Appendix H.

From this analysis of particle velocity across a range of moisture contents characterizing the bed on both sides of the freezing point, it is clear that the mean total velocity of particles sampled within the saltation cloud increases with an increase in interparticle force within the bed surface. However, an increase in particle velocity is not seen with an increasing ratio of pore ice to water. For beds devoid of pore water, temperatures that lie above the freezing point tend to be associated with lower particle velocities, but increasingly cold conditions do not consistently increase particle velocity. Further experiments with test replicates are needed to fully examine this relation.

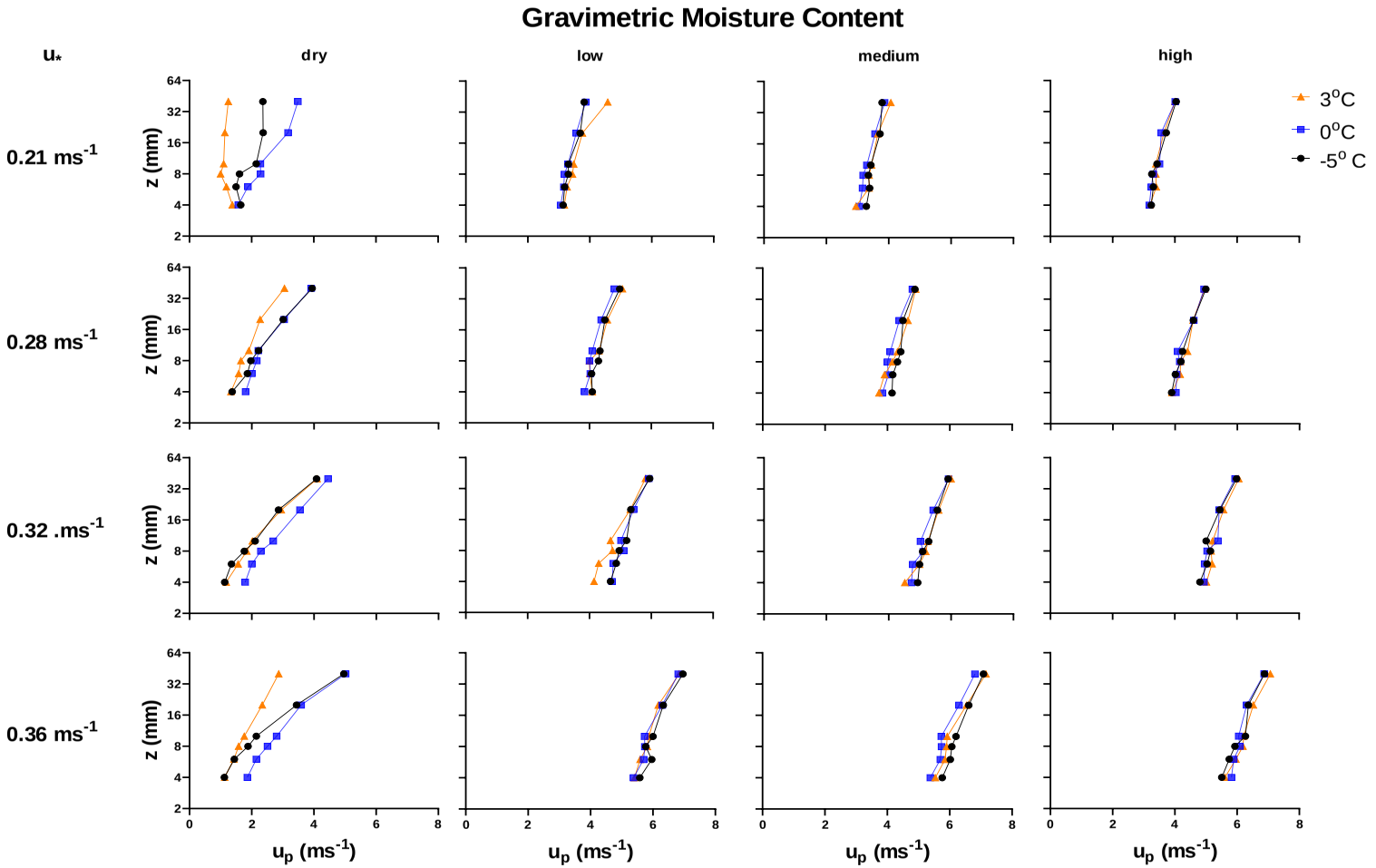

Figure 4.3: Vertical profiles of the mean total particle velocity. Profiles are plotted for varied combinations of wind speed and temperature. Each profile is based on a single replicate.

Table 4.3: Average and standard deviation for the total particle velocity sampled for each temperature and moisture setting at 4 mm and 40 mm above the bed surface.

u_* (ms^{-1})			0.21		0.28		0.32		0.36	
Height	T (°C)		Mean	St. Dev	Mean	St. Dev	Mean	St. Dev	Mean	St. Dev
4 mm	3	dry	1.24	1.18	1.84	1.47	1.14	1.81	1.30	1.36
		low	3.14	0.73	3.90	1.16	4.03	1.35	5.39	1.33
		medium	2.89	0.94	2.89	0.94	4.39	1.40	5.52	1.24
		high	3.05	0.82	3.79	0.95	5.19	0.97	5.54	1.32
	0	dry	1.58	1.31	1.72	1.46	1.67	1.38	1.85	1.59
		low	3.10	0.80	3.88	1.00	4.41	1.21	5.19	1.48
		medium	2.95	0.88	3.76	1.00	4.69	1.02	5.37	1.04
		high	3.07	0.89	3.97	0.86	4.88	0.92	5.84	1.05
	-5	dry	1.80	1.38	1.38	1.36	1.14	1.30	1.12	1.26
		low	3.02	0.93	3.97	1.01	4.66	1.21	5.64	1.16
		medium	3.21	0.91	4.13	0.81	4.96	0.98	5.81	1.06
		high	3.16	0.77	3.83	0.97	4.89	0.97	5.51	1.14
40 mm	3	dry	1.21	1.16	3.60	1.08	3.90	1.81	4.69	1.56
		low	4.29	0.60	4.97	0.82	5.60	1.21	6.84	0.98
		medium	4.03	0.76	4.75	0.96	5.80	1.01	7.07	1.03
		high	3.93	0.79	4.91	0.69	5.98	1.24	6.91	1.10
	0	dry	3.32	1.24	3.76	1.27	4.25	1.42	4.82	1.58
		low	3.66	0.75	4.69	1.17	5.74	1.08	6.70	0.93
		medium	3.72	1.12	4.74	0.78	5.91	0.86	6.72	0.93
		high	3.91	0.67	4.84	0.82	5.87	0.99	6.83	0.98
	-5	dry	2.88	1.35	3.78	1.32	3.91	1.47	4.79	1.62
		low	3.74	0.79	4.90	0.76	5.89	1.14	6.97	0.80
		medium	3.81	0.85	4.78	0.88	5.93	0.96	7.00	0.82
		high	3.91	0.84	4.94	0.83	5.99	0.80	6.87	0.88

4.1.4 Coefficient of restitution

Pore ice and water change the strength properties of the surface causing particle collisions to become more elastic. Sampling velocities in two dimensions in a vertical profile indirectly provides information about the partitioning of momentum when particles collide with the surface, as well as the elasticity of the collision. The coefficient of restitution, calculated as the ratio of the rebound velocity to the impact velocity, provide an index of the elasticity of a given collision. Particles with high rebound velocities and high coefficients of restitution are assumed in this study to be saltators, retaining more momentum after collision with the surface than for relatively low-speed splashed particles with low coefficients of restitution. To calculate the coefficient of restitution for a given experiment, all particle velocity (u_p) data from the 4 mm sampling elevation were isolated. This is the sampling point closest to the bed where particles are either about to impact the surface or have just departed from the surface. Particle velocities then were segregated by the respective vertical velocity component (u_{pv}), given that negative values represent descending grains and vice versa. The average velocity calculated for all ascending grains was divided by that for all descending grains to approximate the bulk coefficient of restitution for the subpopulation of particles sampled. In collisions with either a wet or frozen bed surface, rebounding particles conserved up to 80% of their incoming momentum, as opposed to only 60% over a dry, loose surface (Table 4.2). However, no significant difference (95% confidence level) is found between the coefficients of restitution for surfaces of low, medium, and high moisture content (see Appendix I for details of the one-way ANOVA).

Table 4.4: Coefficient of restitution calculated using LDA velocity data from the 4 mm sampling point.

u_* (ms^{-1})	0.21			0.28			0.32			0.36		
T (°C)	3	0	-5	3	0	-5	3	0	-5	3	0	-5
dry	0.58	0.59	0.68	0.69	0.62	0.71	0.73	0.62	0.70	0.66	0.63	0.71
low	0.81	0.76	0.81	0.76	0.82	0.84	0.80	0.83	0.78	0.82	0.85	0.82
med.	0.75	0.76	0.83	0.78	0.81	0.84	0.83	0.83	0.84	0.84	0.85	0.85
high	0.90	0.80	0.84	0.79	0.81	0.83	0.85	0.84	0.88	0.82	0.84	0.86

4.1.5 Surface erosivity

The degree of surface erosivity for beds of varying moisture content was evaluated and compared for all three temperature settings (3, 0, and -5 °C) as follows. Using images of sediment collected by the GT wedge trap, a customized Matlab program was used to identify and count the number of white pixels associated with particles ejected from the bed surface, and then divide this value by the number of red pixels associated with particles originating from the upwind feed. The resultant is described herein as the Erosivity Index and denoted with the character epsilon (ϵ). This index provides an indication of the bed's susceptibility to abrasion when initiated by an upwind source of loose grains moving in ballistic trajectories. The higher the order of magnitude of the index, the more erosive is the surface. Figure 4.4 examines the influence of temperature and moisture content on ϵ, with the raw data binned over all windspeed settings. Across all three temperatures, the dry surface has an Erosivity Index of approximately 10^5. For any given temperature, a general decrease in erosivity with increasing moisture content is observed. At 5 °C, a slightly lower index value of $10^{4.5}$ is

observed for the low moisture content bed, decreasing to 10^{1} at 0 ºC and $10^{0.5}$ at -5 ºC. Erosivity Indices for bed surfaces with medium to high moisture content provide new insights into the underlying processes. The least erosive surfaces were the medium and high moisture content beds at 0 ºC with $10^{-3} < \epsilon < 10^{-1}$, suggesting varying degrees of adhesion of the feed grains to the wet surface. When the same amounts of pore water are frozen at -5 ºC within the bed surface, $10^{-1} < \epsilon < 1$, corresponding to the ejection of approximately one white particle arising from the impact of each red particle from the upwind feed.

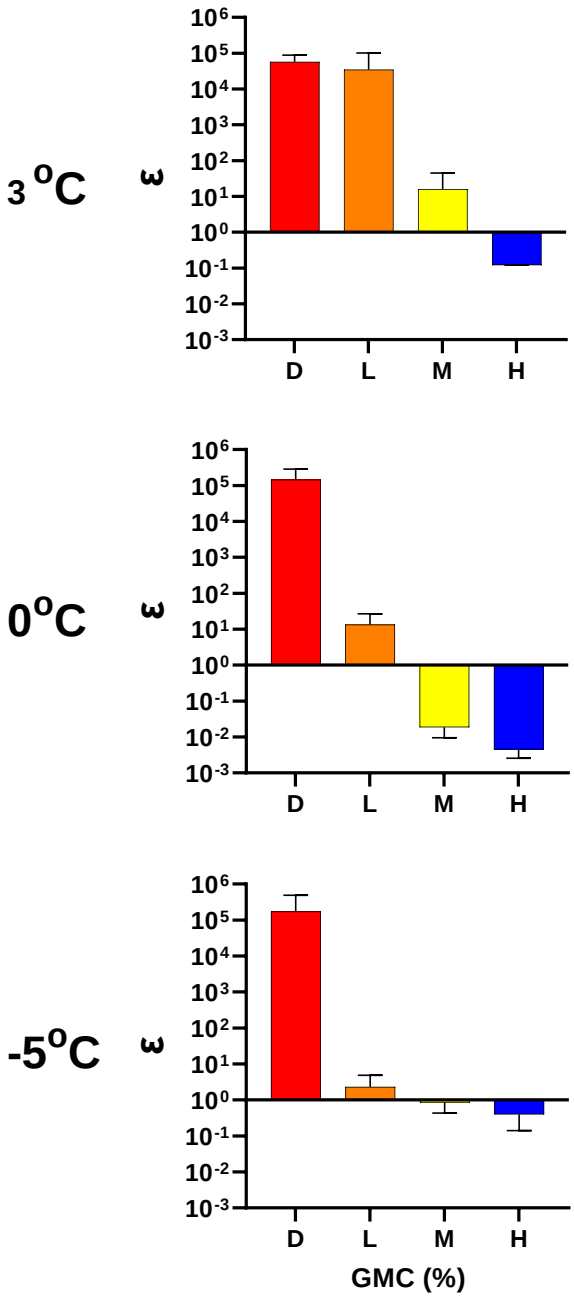

Figure 4.4: Dependency of the Erosivity Index on pore water content and temperature. At 10^0, there is one white particle for every red particle, suggesting that each red particle impacting the surface liberated one particle from the bed.

4.1.6 Saltation Flux

Unlike the Keyence laser sheet sensor measurements which serve as a proxy for the mass transport rate (Q), the saltation trap provides a direct, scalable measurement in physically meaningful units, kg m^{-1} s^{-1}. Figure 3.12 displays systematic variation in Q that is either very subtle or completely absent in the laser sheet data. The transport rates for dry beds under all temperature regimes are greater than for the low moisture content beds, followed by those with medium water content. The beds with the highest moisture contents have the lowest transport rates.

In comparing transport rates across the freezing point within a narrow 8ºC temperature range, it appears that temperature has little influence in a dry system. Once water is added to the bed surface, however, the temperature or phase change begins to play a role (Figure 4.5). At low and medium moisture contents, Q is higher at 3ºC than at 0 and -5ºC when pore ice forms. At high moisture contents nearing saturation, when the interparticle voids are nearly filled with water, the sand transport rate does not scale with either windspeed or temperature. This outcome is consistent with previous observations in this study which suggest that pore ice is more effective at arresting transport than pore water until a very high pore water content is attained.

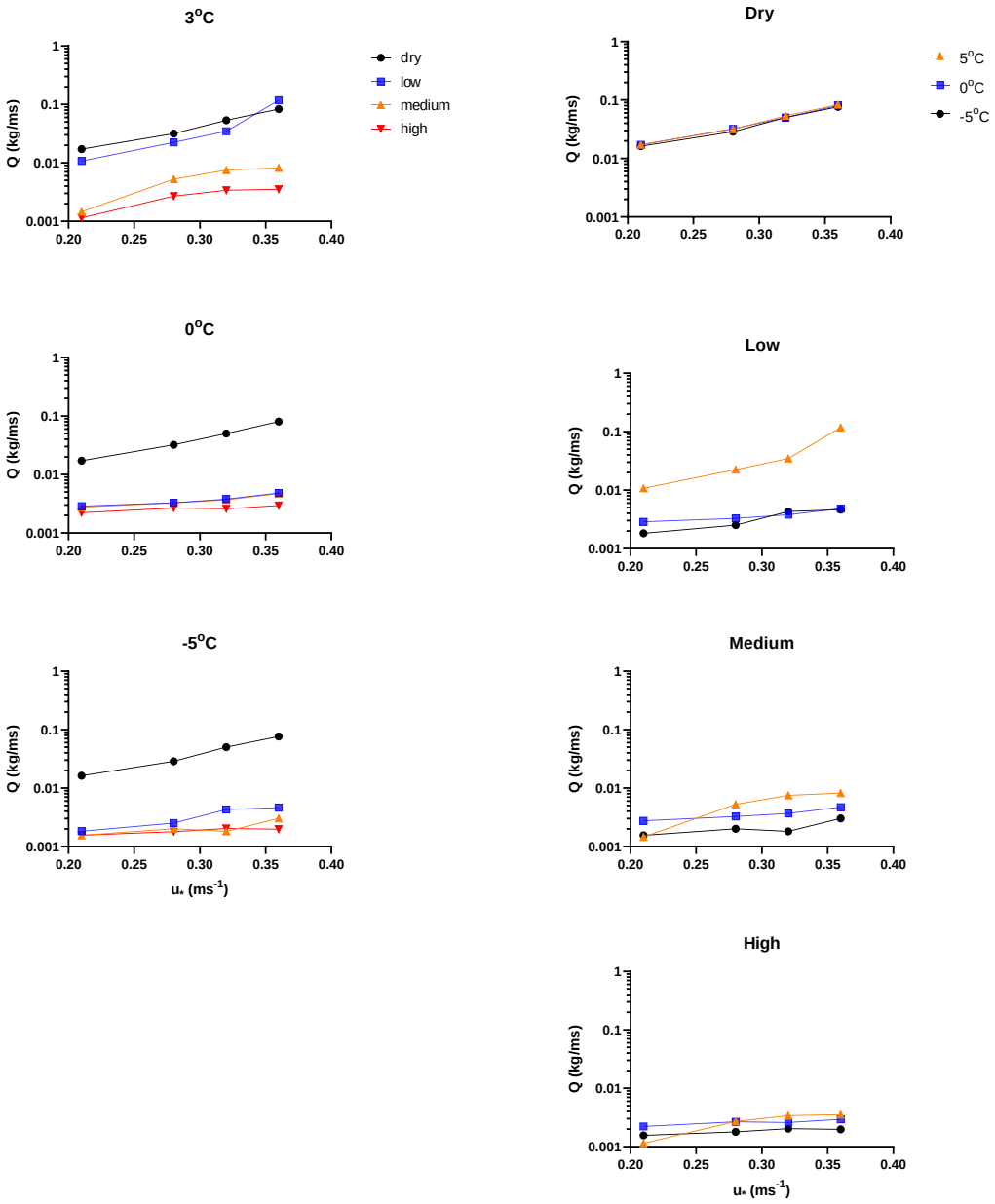

Figure 4.5: (Left) Average mass transport rates showing an increase in transport with increasing u∗ for each water content. (Right) Average mass transport rates plotted to show temperature effects on mass transport.

4.2 Discussion

4.2.1 Kinematics of particle transport

When the temperature of the bed drops below 0°C, not all the water in the pore spaces freezes. Based on a thermodynamic model to determine the unfrozen water content at -5°C, the liquid water saturation or the percentage of water that remains liquid, is around 2% (Xiao et al., 2020). This has implications for the resistance of the surface to fracture, as its strength increases with increasing pore ice content (Lai et al., 2014; Xiao et al., 2020). Higher fluid drag is therefore required to initiate particle entrainment because of interparticle cohesion. Over surfaces bound by such strong cohesive forces, impactors retain much more of their momentum, resulting in more elastic collisions, than for the splash-generating collisions occurring over dry surfaces.

Table 3.6 displays the bulk coefficient of restitution, which can be used to make inferences about the kinematics of particles travelling along ballistic trajectories within the saltation cloud. Particles saltating over surfaces with low, medium, and high moisture contents all have coefficients of restitution ranging from 79% to 86%, as compared to 61 to 66% for the dry surface. This confirms that particles retain more of their kinetic energy upon impact with a wet or frozen surface. Such particles ricochet off the surface at relatively high speeds as compared to a dry bed, moving higher into the shearing flow where they experience greater fluid drag and thus acceleration. The low coefficient of restitution over the dry surfaces are indicative of greater momentum partitioning to the bed surface and the consequent splash ejection of slow-moving particles which surrounded the impact site. This analysis provides indirect evidence in support of hypothesis 4 suggesting that the proportion of particles traveling in creep and reptation

relative to those moving in ballistic trajectories is higher for dry surfaces than those with either pore ice or water.

Both numerical and wind tunnel experiments report similar values for the coefficient of restitution over dry, loose surfaces (Gordon & Mckenna Neuman, 2011; Gordon & Neuman, 2009; Haff & Ansderson, 1993; O'Brien & Mckenna Neuman, 2012; Yaping Shao, 2008). One such study by O'Brien & McKenna Neuman (2012) also used a means-based approach to calculating the coefficient of restitution, which is the sample average velocity for the ascending particles divided by that for the descending particles ($u_p\uparrow / u_p\downarrow$). One drawback associated with this computational method is that no distinction is made between particles that ricochet off the bed and those ejected from it. A further limitation of the present study is that the sampling height for the LDA was 4 mm, well above the bed surface relative the diameter of a sand particle that is an order of magnitude smaller. At this elevation, particles ricocheting off the bed would have been accelerated to a small degree by the fluid drag of the wind that the outgoing velocity measured may be high as compared to that immediately after impact with the surface. The particle tracking methodology used by Gordon and Mckenna Neuman (2011) employed high-speed photography to isolate the trajectories of discrete particles as they saltated over a test surface. Although this method is direct and therefore more accurate, it is also very slow and tedious, and thus, the sample size is relatively small (10^1). The means-based approach, based on sample sizes in the order of 10^3, provides a reasonable first approximation of ε. But the challenge is the light source needed to illuminate the particles, as it would cause melting of the pore ice in low temperature experiments. This

might be possible with backlighting using LED, but currently a high-powered laser is used.

Figure 4.3 shows that particle velocity increases substantially with the addition of any amount of water to a dry sand bed. However, increasing the moisture content from low to medium to high does not result in a sustained velocity increase. These results are consistent with the findings of O'Brien and McKenna Neuman (2023) in which Particle Tracking Velocimetry allowed for the analysis of the near-surface (below 5 mm elevation) dynamics of particles saltating over surfaces of varying moisture content. As compared to a dry, loose bed, they measured particle velocities 1.4 times greater over a bed of 4% GMC and 1.8 times greater over a bed of 10% GMC. For a similar range in moisture content, however, particle velocities measured in this project were 3-6 times greater than those for a dry bed. This difference may in part be due to the varied instrumentation and sampling design. O'Brien and McKenna Neuman's PTV work assessed particles saltating in trajectories no higher than 5 mm above the bed. The LDA used for this project could only measure particle velocities at and above 4 mm in elevation resulting in the under-sampling of splashed particles and preferential sampling of particles saltating higher within the shearing flow, potentially experiencing more drag. Nonetheless, the results of the present study point to a significant increase in particle velocity and thereby, kinetic energy with the introduction of bed moisture.

The mean velocities of all ascending particles at 4 mm above the bed surface is plotted in Figure 4.6 against the shear velocity for the run. As characteristic of a saturated saltation cloud, particle speed at the lowest point sampled above the dry bed stays the same across all wind speeds (O'Brien & McKenna Neuman, 2018). Increasing the available fluid momentum by increasing the shear velocity does not increase the speed of the grains near the bed, but moves more of them. This is a distinguishing feature of a *transport-limited* system (Parsons & Abrahams, 2009). With the addition of pore water to the bed surface, less particle ejection or splash occurs. Therefore, less momentum is partitioned from the airflow so that the fluid drag is not only able to accelerate saltating grains to higher velocities than for the dry bed, but also, the particle speed in this *supply-limited* system scales with the shear (u_*) within the boundary layer airflow. This is consistent with the results from the coefficient of restitution data and stands in partial support of Hypothesis 5 wherein adding either pore water or ice serves to increase the kinetic energy of particles travelling within the saltation cloud; however, the amount of water does not have a strong influence.

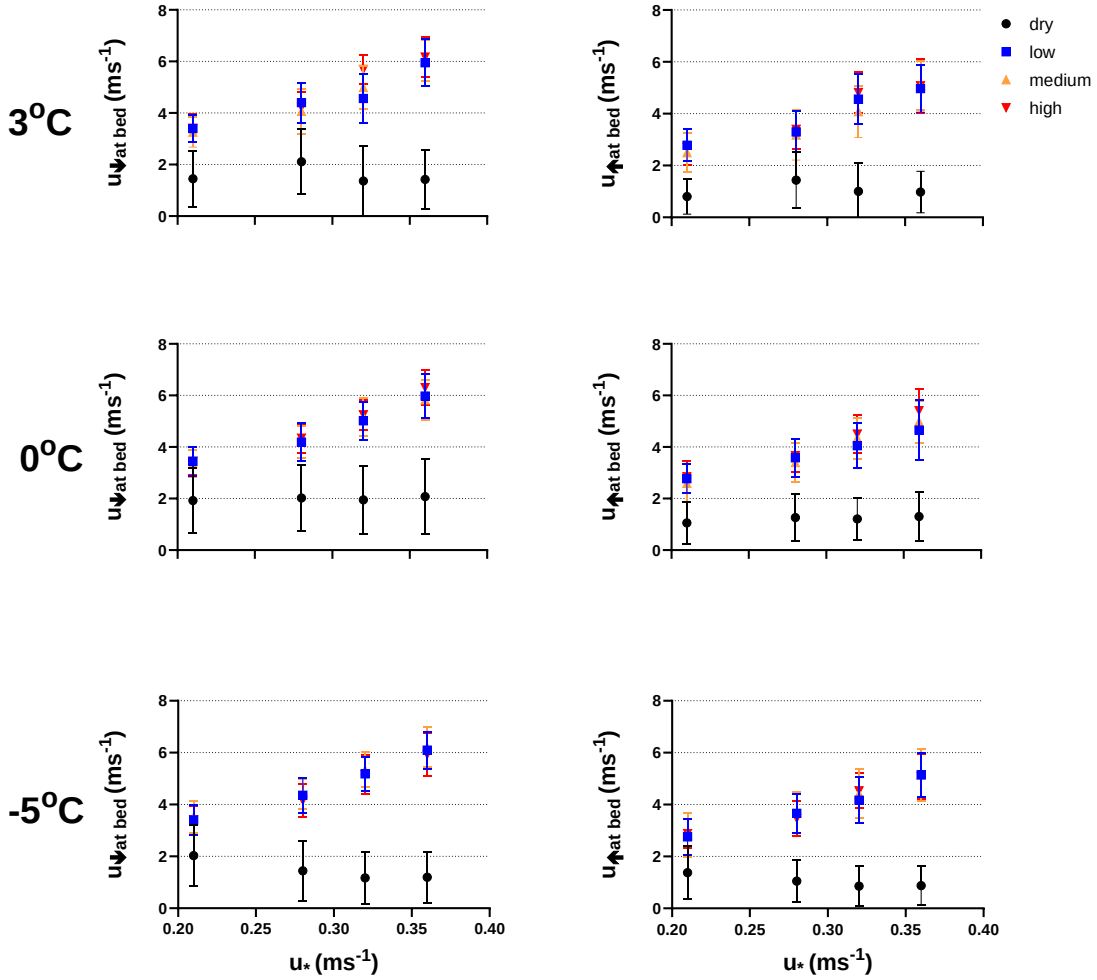

Figure 4.6: Plot of the velocity of ascending particles ($u_{\uparrow}$) and descending particles ($u_{\downarrow}$), 4 mm above the surface, against the shear velocity (u_*) of the airflow. Velocities greater than 2 standard deviations from the mean were excluded from the analysis.

Additionally, evidence of an effect of temperature on particle speed can be seen. Under dry conditions, except for at 0.32 ms^{-1}, the mean total particle speed in vertical profile at 3ºC is consistently lower than at 0 and -5ºC (Figure 4.3). Density driven changes in the fluid drag are not responsible for this (Figure 1.3). Having looked at a temperature range of only 8ºC, future studies should aim to cover a much broader range of temperature, one that is representative of all natural environments in which aeolian processes occur. As done with the mass transport experiment described in Chapter 3 for which -13 °C < T < 30 °C, a wider scale may allow further refinement of the relationships between particle velocity and either temperature or surface moisture content.

4.2.2 Surface erosivity and mass transport

Given that particles saltate over surfaces of high moisture content and pore ice content with more velocity and thus kinetic energy, it can be expected that these surfaces, although more cohesive than dry surfaces, experience some degree of abrasion. This is quantified in this study by the Erosivity Index (ε), which is the proportion of (white) particles collected in the sand trap that originated from within the bed surface to those supplied from an upwind gravity feed (red). Experiments using the red tracer confirm that dry, cohesionless beds are highly erosive. Cohesive beds with pore water/ice can also erode, but ε was found to decrease with increasing GWC (Figure 4.4) while the impact velocity (U↓) was unaffected by the amount of pore water. In a pioneering experiment by McKenna Neuman (1989), surfaces of various textures, temperature, and moisture content were sandblasted (10 m s^{-1} < U ↓ < 15 m s^{-1}), demonstrating and quantifying the

susceptibility of frozen surfaces to erosion. However, it remains unclear whether single impacts or a series of fluctuating stresses causing fatigue failure are responsible.

In comparison to beds with higher moisture content, the Erosivity Index decreases as temperature decreases for surfaces with a low moisture content. This implies that the phase change of water in the pore spaces of the grains into ice led to a decrease in the bed's erosivity. It is well known that pore ice enhances surface strength (Lai et al., 2014; Xiao et al., 2020).

The least erosive surfaces were the medium and high moisture content beds at 0°C. For these surfaces, the corresponding ϵ value was 10^{-2}, suggesting that for approximately every 100 red grains impacting the surface, one white grain was ejected from the bed. At the same moisture content for 3°C and -5°C, ϵ was higher, ranging between 10^{1} and 10^{-1}. During the experiment setup, replicating a given bed moisture content was a challenge due to the large surface area that needed to be sprayed with water. However, the medium and high moisture contents for the runs at 0°C were not substantially higher than those at 3°C and -5°C (Table 2.2), which suggests that the observed artifact was not caused by inaccurate moisture content replication. Instead, the low Erosivity Index might be explained by the state of water around the freezing point. At -5°C, nearly 100% of the water (Xiao et al., 2020) within the pores of the sand bed was frozen. At 3°C, none of the water was frozen. During the 0°C runs, however, the temperature fluctuated between 1 and -1°C with operation of the climate control system. Since the pore ice in the underlying bed remained frozen and prevented seepage, water pooled on the surface with melting and then refroze with a slight drop in temperature across the freezing point. These thin sheets of water increased the surface's "stickiness"

and served to trap saltators while preventing particle ejection or “splash”, limiting the erosivity of the surface. When frozen they sheltered to some degree the underlying particles from direct impact. In conclusion, surface erosivity is governed mainly by moisture content, however, as previously discussed, phase changes of water also appear to be influential as apparent in beds with low moisture contents. This confirms Hypothesis 6 that fewer particles will be ejected during a collision with a surface at or below 0^{o}C with ice relative to a warm, dry surface.

The Erosivity Index is not to be confused with the well-known splash index that quantifies the number of bed grains ejected per impacting red grain. When the impact of a loose grain from an upwind source (in this case the particle feed containing a tracer distinguished by its red colour) results in the ejection of a grain from the bed surface, the splashed particle has the potential to eject other grains in subsequent collisions. Although ε is a fetch dependent index specific to the experimental design and not transferrable to other settings, the general trends observed provide a useful indicator of the ability of particles from the upwind supply to a) successively saltate along the entire length of the test bed, and b) initiate a cascade of particle ejection, transport, and impact.

As the saltation cloud develops and increases in density over some distance, the cumulative number of impacts on the surface increases to cause generalized disruption of the interparticle bonds and bed packing.

In laboratory experiments, fetch is an important consideration as it can limit our ability to observe a fully adjusted saltation transport cloud. Wind tunnel working sections are often shorter than the critical fetch length required for a given geophysical process to

reach equilibrium (Delgado-Fernandez, 2010). In terms of the saltation flux, the critical fetch length is the distance required for the maximum mass transport rate to be attained and sustained. The array of Keyence^{TM} laser sheet sensors was used in this study to examine changes in the saltation intensity with distance downwind. Under dry conditions, Figure 4.2 shows that the saltation intensity reached a maximum value ~ 5.45 m downwind. At this point, no more momentum can be extracted from the fluid and the saltation cloud is in equilibrium. As soon as some moisture is added to the bed, the saltation intensity decreases by 80 to 95%. It was also found to be higher over the low moisture content bed at 3ºC than at 0 and -5ºC, most likely for the same reasons that the erosivity was higher.

From field experiments conducted on a beach and foredune in Prince Edward Island National Park, Bauer et al., (2009) conclude that after a rainfall event, reaching the theoretical maximum rate of transport requires a much larger critical fetch length than after a period of surface drying. The laser sheet sensors confirm that the aeolian transport system became particle supply-limited after the addition of water to the surface, while the saltation cloud remained undersaturated with particles throughout the length of the tunnel working section.

However, several limitations are associated with these instruments and their setup, as outlined in section 3.2.2. One further problem is that particles travelling in high, ballistic trajectories may avoid detection by saltating above/over the laser sheet and. As the proportion of such particles increases when moisture is added and collision with the bed surface becomes more elastic, the laser sheets may under sample the saltation

intensity to an unknown extent. Nonetheless, these instruments provide a useful first approximation of fetch effects for surfaces of varied moisture content.

Thus far, saltation intensity and the Erosivity Index have been addressed to assess the dynamics of saltation over frozen surfaces. These two variables are useful but indirect indices of the saltation flux or the mass transport rate (Q). The Guelph-Trent sediment trap is an instrument that directly measures Q through sampling the real-time cumulative mass transport. Figure 4.5 compares Q for each moisture content and temperature setting. There is an abrupt, significant decrease in Q is between dry and wet. Adding more water (from medium to high gravimetric contents) has little influence on Q. This is further evidence supporting the hypothesis (Hypothesis 6) that fewer particles will be ejected during collisions with a surface below 0ºC with pore ice, relative to a warm dry surface. In terms of Hypothesis 2, however, the processes prove to be more complicated. For the low moisture content regime at 3ºC, Q is significantly higher than at 0 ºC and -5 ºC. It is believed that increases in pore ice content are responsible for this, which is determined by temperature. At medium and high moisture contents, however, the cohesion created by the liquid pore water in the bed surface appears to limit aeolian transport as much as the pore ice in a frozen surface so that Q is not temperature dependent. The effect of water pooling in arresting transport has already been discussed for conditions nearing saturation. No effect of temperature on Q is seen under dry conditions. However, the conclusions from Experiment 2 are limited by the narrow 8 ºC temperature range over which the runs took place and the highly stochastic nature of the processes (i.e. noise). In comparison, Figure 3.1 shows a consistent increase in Q with a temperature drop (R^2 values ranging from 0.47 to 0.85) across a 40 ºC temperature range. Through extending

the temperature range from 8 ºC to 40 ºC, a wider range of natural environments should be considered in future work as an extension to the findings reported in this chapter.

Chapter 5: Conclusions

In this study, the dynamics of particle saltation over a full bed of sand with varying moisture contents and a range of temperatures extending below the freezing point of water were measured in an experimental wind tunnel laboratory for the first time. Measurements of saltation flux, particle velocities, and PM_{10} concentrations in profile over a mobile bed were made. In addition, a novel experimental design was employed to quantify the erosivity of surfaces of varying moisture content. The results provide an improved understanding and quantification of particulate transport in cold environments.

Following the six main hypotheses, the key findings are summarized below:

1) The height of the saltation cloud and the intensity profile of saltation were found to be unaffected by temperature. However, these results are questionable due to the indirect measurement method involving laser sheet sensors and sampling within a saturated particle cloud at elevations that lay outside its core.

2) Across a temperature range of 40ºC, at both low and high relative humidities the particle mass transport rate increases over dry surface with a drop in temperature and greater fluid density. Introducing moisture to the system reduces the mass flux significantly, suppressing particle entrainment by fluid drag. However, loose particles from an upwind source can efficiently move in ballistic trajectories over a wet or frozen surface.

3) It is well known that saltation is the main driver of dust emission. The findings of this project confirm this as the vertical dust flux, when normalized by the saltation flux, shows no dependency on either the air temperature or relative humidity.

4) Inferences made from analysis of the bulk coefficient of restitution suggest that the proportion of splashed particles travelling in creep/reptation relative to saltation decreases with an increasing ratio of pore ice to water. Outgoing particle velocities were significantly higher over wet/frozen surfaces than dry ones, suggesting more elastic collision and energy retention in particle ricochet but reduced partitioning of momentum to particles splashed from the bed.

5) Over the dry beds, particles travel slower over warm beds than over cold beds. There is a significant increase in particle velocities from a dry bed compared to a bed with a gravimetric moisture content of about 3%. However, any additional water does not increase the particle velocity significantly.

6) Based on a tracer method and sediment trap measurements, it was determined that fewer particles are emitted from a surface below 0^{o}C with pore ice than from a warm, dry surface. The formation of pore ice with a decrease in temperature would appear to strengthen interparticle bonding.

5.1 Relevance and importance of findings

The effects of colds temperatures and pore moisture on particulate transport studied in this project underscores the significance of understanding these interactions for both scientific understanding and practical applications.

For decades, field studies have identified aeolian deposits and landforms such as ripples, dunes, and lag surfaces in cold and seasonally cold regions of the world (Belanger & Filion, 1991; Selby et al., 1973; Smith, 1980; Thorn & Darmody, 1985). Over time, the processes that create these landforms have become better understood. By quantifying the erosivity of surfaces and particle kinematics over surfaces with varying moisture content and temperature, we can address crucial knowledge gaps surrounding the formation of aeolian landforms in cold regions.

Particulate transport affects our built environment. Infrastructure within cold or seasonally regions has been known to be damaged by sand and dust transport such as bridge damage in South Tibet (Xie et al., 2020) or railroad blockages in China (Zhang et al., 2012). As the Arctic warms, new infrastructure developments such as roads, railways, and mines will open in these areas. Along with anthropogenic sources of dust, new sources of sediment will become available for transport from melting permafrost and glaciers. This can pose risks to not only the built environment but to flora and fauna as well as human health. Findings from this study can provide insight into the modelling of sand and dust transport in these areas that are not encompassed by current models. Many aeolian transport models use the blackbox parameter, “c”, to incorporate variables or

processes that are difficult to characterize or measure. The results from this thesis can assist with model calibration to improve performance for cold regions.

Finally, this thesis can contribute to future research projects investigating cold-temperature aeolian processes. By creating a novel experimental design to approach this topic, a path has been paved for continued research into these processes. The limitations and difficulties encountered throughout the project may provide insight for those wishing to further this research.

5.2 Suggestions for further research

This project has laid the groundwork for future research into cold-temperature sediment transport processes. The next steps should include expansion of the particle velocity measurements conducted with wet and frozen surfaces to include a greater range of environmental temperature conditions and more experimental replication. Although it is difficult to precisely control the moisture content of the bed surface, future research should attempt to focus on contents between 0-3% to determine how gradual the changes in mass transport rates and particle velocities with increasing moisture content are. If possible, extending the temperature range below -10^{o}C would also be substantial. Previous lab work (McKenna Neuman, 1989) indicates that as ice loses its strength at -20^{o}C, abrasion and mass transport increase. Finally, understanding the role of air density, viscosity and turbulence in dust dispersion at different temperatures and humidities is an important next step. Mobile beds limited the ability for these variables to be isolated, as

dust emission is so dependent on saltation rates. Conducting dust dispersion experiments over fixed floorboards at different temperatures would be beneficial.

The methods developed may serve as a basis for future experimentation. Ultimately, this project validates previous discoveries made through laboratory and field research, demonstrating that addressing inquiries about the transport of particulates in cold climates is achievable. Moreover, it expands the range of inquiries that scientists in this field can now address.

The results of this study would suggest that research on sediment transport should not be limited to the hot, arid regions of the world. Rather, cold-climate aeolian processes are dynamic, energetic and can have far reaching effects. With climate change, high-latitude regions are experiencing disproportionate warming. As glaciers recede, new sources of particulates are emerging and becoming susceptible to transport. With a more temperate climate and shallower frost depth, increased human activity in mining and agriculture will increase the availability of dust for transport, negatively impacting human and animal health. Moreover, these findings can be applied to a variety of planetary surfaces where aeolian processes dominate, such as the Martian surface, allowing for the greater understanding of extraterrestrial bodies. These processes should be further researched to better predict their magnitude and their reach.

Bibliography

Amino, T., Iizuka, Y., Matoba, S., Shimada, R., Oshima, N., Suzuki, T., Ando, T., Aoki, T., & Fujita, K. (2020). Increasing dust emission from ice free terrain in southeastern Greenland since 2000. *Polar Science*, 100599. https://doi.org/10.1016/j.polar.2020.100599

Baker, M. M. et al. "Coarse Sediment Transport in the Modern Martian Environment." *Journal of geophysical research. Planets*, vol. 123, no. 6, 2018, pp. 1380-94, doi:10.1002/2017je005513.

Barchyn, Thomas E. and Chris H. Hugenholtz. "Winter Variability of Aeolian Sediment Transport Threshold on a Cold-Climate Dune." Geomorphology (Amsterdam, Netherlands), vol. 177-178, 2012, pp. 38-50, doi:10.1016/j.geomorph.2012.07.012.

Barr, S. L., Wyld, B., Mcquaid, J. B., Iii, R. R. N., & Murray, B. J. (2023). Southern Alaska as a source of atmospheric mineral dust and ice-nucleating particles. *Science Advances*, *9*, 1–12. https://doi.org/10.1126/sciadv.adg3708

Bauer, B. O., Davidson-Arnott, R. G. D., Hesp, P. A., Namikas, S. L., Ollerhead, J., & Walker, I. J. (2009). Aeolian sediment transport on a beach: Surface moisture, wind fetch, and mean transport. *Geomorphology*, *105*, 106–116. https://doi.org/10.1016/j.geomorph.2008.02.016

Belanger, S. and L. Filion. "Niveo-Aeolian Sand Deposition in Subarctic Dunes, Eastern Coast of Hudson Bay, Quebec, Canada." Journal of Quaternary Science, vol. 6, no. 1, 1991, pp. 27-37.

Bromwich, D. H. (1989). An Extraordinary Katabatic Wind Regime at Terra Nova Bay, Antarctica. *Monthly Weather Review*, *117*, 688–695.

Bullard, J. E. (2013). Contemporary glacigenic inputs to the dust cycle. *Earth Surface Processes and Landforms*, *38*, 71–79. https://doi.org/10.1002/esp.3315

Bullard, J. E., Baddock, M., Bradwell, T., Crusius, J., Darlington, E., Gaiero, D., Gassó, S., Gisladottir, G., Hodgkins, R., McCulloch, R., McKenna Neuman, C., Mockford, T., Stewart, H., & Thorsteinsson, T. (2016). High-latitude dust in the Earth system. *Reviews of Geophysics*, *54*, 447–485. https://doi.org/10.1002/2017RG000559

Chen, W., Leblanc, S. G., White, H. P., Prevost, C., Milakovic, B., Rock, C., Sharam, G., Keefe, H. O., Corey, L., Croft, B., Gunn, A., Wielen, S. Van Der, Football, A., Tracz, B., Snortland Pellissey, J., & Boulanger, J. (2017). Does Dust from Arctic Mines Affect Caribou Forage? *Journal of Environmental Protection*, *8*, 258–276. https://doi.org/10.4236/jep.2017.83020

Comola, F., Gaume, J., Kok, J. F., & Lehning, M. (2019). Cohesion-induced enhancement of aeolian saltation. *Geophysical Research Letters*, *46*, 5566–5574. https://doi.org/10.1029/2019GL082195

Delgado-Fernandez, I. (2010). A review of the application of the fetch effect to modelling sand supply to coastal foredunes. *Aeolian Research*, *2*((2-3)), 61–70. https://doi.org/10.1016/j.aeolia.2010.04.001

Dong, Z., Qian, G., Luo, W., & Wang, H. (2006). Analysis of the mass flux profiles of an aeolian saltating cloud. *Journal of Geophysical Research*, *111*(D16111), 1–11. https://doi.org/10.1029/2005JD006630

Dong, Z., Wang, H., Liu, X., & Wang, X. (2004). The blown sand flux over a sandy surface: a wind tunnel investigation on the fetch effect. *Geomorphology*, *57*, 117–127. https://doi.org/10.1016/S0169-555X(03)00087-4

Dong, Z., Wang, H., Zhang, X., & Ayrault, M. (2004). Height profile of particle concentration in an aeolian saltating cloud: A wind tunnel investigation by PIV MSD. *Geophysical Research Letters*, *30*(19). https://doi.org/10.1029/2003GL017915

Eden, D. N., & Hammond, A. P. (2003). Dust accumulation in the New Zealand region since the last glacial maximum. *Quaternary Science Reviews*, *22*, 2037–2052. https://doi.org/10.1016/S0277-3791(03)00168-9

Engelstaedter, S., & Washington, R. (2007). *Temporal controls on global dust emissions : The role of surface gustiness*. *34*(March), 1–5. https://doi.org/10.1029/2007GL029971

Fan, S. (2013). Modeling of observed mineral dust aerosols in the arctic and the impact on winter season low-level clouds. *Journal of Geophysical Research: Amospheres*, *118*, 11,161-11,174. https://doi.org/10.1002/jgrd.50842

Gillette, D. A., Fryrear, D. W., Xiao, J. B., Stockton, P., Ono, D., Helm, P. J., Gill, T. E., & Ley, T. (1997). Large-scale variability of wind erosion mass flux rates 1. Vertical profiles of horizontal mass fluxes of wind-eroded particles with diameter greater than 50 μm. *Journal of Geophysical Research*, *102*(D22), 25,977-25,987.

Gillies, John A. et al. "Ventifacts and Wind-Abraded Rock Features in the Taylor Valley, Antarctica." Geomorphology, vol. 107, no. 3-4, 2009, pp. 149-60,

doi:10.1016/j.geomorph.2008.12.007.

Gillies, J. A., Nickling, W. G., & Tilson, M. (2013). Frequency, magnitude, and characteristics of aeolian sediment transport : McMurdo Dry Valleys, Antarctica. *Journal of Geophysical Research Earth Surfaces*, *118*, 461–479. https://doi.org/10.1002/jgrf.20007

Gillies, J. A., Nickling, W. G., Tilson, M., & Furtak-Cole, E. (2012). Wind-formed gravel bed forms, Wright Valley, Antarctica. *Journal of Geophysical Research*, *117*(4). https://doi.org/10.1029/2012JF002378

Gordon, M., & Mckenna Neuman, C. (2011). A study of particle splash on developing ripple forms for two bed materials. *Geomorphology*, *129*, 79–91. https://doi.org/10.1016/j.geomorph.2011.01.015

Gordon, M., & Neuman, C. M. (2009). A comparison of collisions of saltating grains with loose and consolidated silt surfaces. *Journal of Geophysical Research*, *114*, 1–13. https://doi.org/10.1029/2009JF001330

Greeley, Ronald and Raymond E. Arvidson. "Aeolian Processes on Venus." Earth, moon, and planets, vol. 50-51, no. 1, 1990, pp. 127-57, doi:10.1007/bf00142392.

Griffin, D. W., & Kellogg, C. A. (2004). Dust Storms and Their Impact on Ocean and Human Health: Dust in Earth's Atmosphere. *EcoHealth*, *1*, 284–295. https://doi.org/10.1007/s10393-004-0120-8

Haff, P. K., & Ansderson, R. S. (1993). Grain scale simulations of loose sedimentary beds: the example of grain-bed impacts in aeolian saltation. *Sedimentology*, *40*, 175–

198.

Khan, A. L., Dierssen, H., Schwarz, J. P., Schmitt, C., Chlus, A., Hermanson, M., Painter, T., & McKnight, D. (2017). Impacts of coal dust from an active mine on the spectral reflectance of Arctic surface snow in Svalbard, Norway. *Journal of Geophysical Research: Atmospheres*, *122*, 1767–1778. https://doi.org/10.1002/2016JD025757

Kok, J. F., Parteli, E. J. R., Michaels, T. I., & Karam, D. B. (2012). The physics of wind-blown sand and dust. *Reports on Progress in Physics*, *75*. https://doi.org/10.1088/0034-4885/75/10/106901

Koster, E. A. "Ancient and Modern Cold-Climate Aeolian Sand Deposition: A Review." Journal of Quarternary Science, vol. 3, no. 1, 1988, pp. 69-83.

Lai, Y., Pei, W., Zhang, M., & Zhou, J. (2014). Study on theory model of hydro-thermal-mechanical interaction process in saturated freezing silty soil. *International Journal of Heat and Mass Transfer*, *78*, 805–819. https://doi.org/10.1016/j.ijheatmasstransfer.2014.07.035

Lancaster, N. (1981). Grain size characteristics of Namib Desert linear dunes. *Sedimentology*, *28*, 115–122.

Lancaster, Nicholas, Nickling, W. G., & Gillies, J. A. (2010). Sand transport by wind on complex surfaces: Field studies in the McMurdo Dry Valleys, Antarctica. *Journal of Geophysical Research*, *115*, 1–10. https://doi.org/10.1029/2009JF001408

Li, F., Ginoux, P., & Ramaswamy, V. (2010). Transport of Patagonian dust to Antarctica.

Journal of Geophysical Research, *115*(D18217), 1–9. https://doi.org/10.1029/2009JD012356

Lu, H., & Shao, Y. (1999). A new model for dust emission by saltation bombardment. *Journal of Geophysical Research*, *104*, 16827–16842.

McGowan, H. A., & Sturman, A. P. (1997). Characteristics of aeolian grain transport over a fluvio-glacial lacustrine braid delta, Lake Tekapo, New Zealand. *Earth Surface Processes and Landforms*, *22*(8), 773–784. https://doi.org/10.1002/(SICI)1096-9837(199708)22:8<773::AID-ESP781>3.0.CO;2-O

Mckenna Neuman, C. (1993). A review of aeolian transport processes in cold environments. *Progress in Physical Geography*, *17*(2), 137–155. https://doi.org/10.1177/030913339301700203

McKenna Neuman, C. (1989). Kinetic energy transfer through impact and its role in entrainment by wind of particles from frozen surfaces. *Sedimentology*, *36*, 1007–1015.

McKenna Neuman, C. (1990). Observations of Winter Aeolian Transport and Niveo-aeolian Deposition at Crater Lake, Pangnirtung Pass, N.W.T., Canada. *Permafrost and Periglacial Processes*, *1*, 235–247.

McKenna Neuman, C. (1993). A review of aeolian transport processes in cold environments. *Progress in Physical Geography*, *17*(2), 137–155. https://doi.org/10.1177/030913339301700203

McKenna Neuman, C. (2003). Effects of temperature and humidity upon the transport of sedimentary particles by wind. *Boundary-Layer Meteorology*, *108*, 61–89. https://doi.org/10.1046/j.1365-3091.2003.00604.x

McKenna Neuman, C. (2004a). Effects of temperature and humidity upon the transport of sedimentary particles by wind. *Sedimentology*, *51*(1), 1–17. https://doi.org/10.1046/j.1365-3091.2003.00604.x

McKenna Neuman, C. (2004b). Effects of temperature and humidity upon the transport of sedimentary particles by wind. *Sedimentology*, *51*(1), 1–17. https://doi.org/10.1046/j.1365-3091.2003.00604.x

McKenna Neuman, C., & Nickling, W. G. (1989). A theoretical and wind tunnel investigation of the effect of capillary water on the entrainment of sediment by wind. *Soil Science*.

McKenna Neuman, C., & Nickling, W. G. (1997). Wind tunnel evaluation of a wedge-shaped aeolian sediment trap. *Geomorphology*, *18*(1997), 333–345.

McKenna Neuman, C., & Sanderson, S. (2008). Humidity control of particle emissions in aeolian systems. *Journal of Geophysical Research*, *113*, 1–10. https://doi.org/10.1029/2007JF000780

Nakashima, M., & Dagsson-Waldhauserová, P. (2019). A 60 year examination of dust day activity and its contributing factors from ten icelandic weather stations from 1950 to 2009. *Frontiers in Earth Science*, *6*(245), 1–8. https://doi.org/10.3389/feart.2018.00245

Namikas, S., & Sherman, D. (1995). A review of the effects of surface moisture content on aeolian sand transport. *Desert Aeolian Processes*. https://doi.org/https://doi.org/10.1007/978-94-009-0067-7_13

Nappo, C. J., & ShankarRao, K. (1987). A model study of pure katabatic flows. *Dynamic Meteorology and Oceanography*, *39*(1), 61–71.

Nickling, W. G. (1988). The initiation of particle movement by wind. *Sedimentology*, *35*, 499–511. https://doi.org/10.1111/j.1365-3091.1988.tb01000.x

O'Brien, P., & Mckenna Neuman, C. (2012). A wind tunnel study of particle kinematics during crust rupture and erosion. *Geomorphology*, *173–174*, 149–160. https://doi.org/10.1016/j.geomorph.2012.06.005

O'Brien, P., & McKenna Neuman, C. (2018). An experimental study of the dynamics of saltation within a three-dimensional framework. *Aeolian Research*, *31*(May 2017), 62–71. https://doi.org/10.1016/j.aeolia.2017.09.003

O'Brien, P., & McKenna Neuman, C. (2019). Experimental Validation of the Near-Bed Particle-Borne Stress Profile in Aeolian Transport Systems. *Journal of Geophysical Research: Earth Surface*, *124*, 2463–2474. https://doi.org/10.1029/2019JF005114

O'Brien, P., & McKenna Neuman, C. (2023). Effect of the surface water content on dry saltation cloud dynamics: A wind tunnel simulation with particle tracking velocimetry. *Earth Surface Processes and Landforms*, 1–12. https://doi.org/10.1002/esp.5684

Owen, P. R. (1964). Saltation of uniform grains in air. *Journal of Fluid Mechanics*, *20*(2),

225–242.

Papadopoulos, K. H., Helmis, C. G., Soilemes, A. T., Kalogiros, J., Papageorgas, P. G., & Asimakopoulos, D. N. (1997). The structure of katabatic flows down a simple slope. *Quarterly Journal of the Royal Meteorological Society*, *123*, 1581–1601.

Parish, T. R., & Bromwich, D. H. (1991). Continental-Scale Simulation of the Antarctic Katabatic Wind Regime. *Journal of Climate*, *4*, 135–146. https://doi.org/https://doi.org/10.1175/1520-0442(1991)004<0135:CSSOTA>2.0.CO;2

Parsons, A. J., & Abrahams, A. D. (2009). Aeolian Sediment Transport. In *Geomorphology of Desert Environments* (pp. 517–555). Springer Netherlands. https://doi.org/10.1007/978-1-4020-5719-9

Périard, C., & Pettré, P. (1993). Some aspects of the climatology of Dumont Durville, Adelie Land, Antarctica. *International Journal of Climatology*, *13*, 313–327.

Raupach, M. R., & Shao, Y. (1992). The overshoot and equilibration of saltation. *Journal of Geophysical Research*, *97*(D. 18), 20,559-20,564.

Richards-Thomas, T. (2020). Laboratory Investigation of Particle-Scale Factors Affecting the Settling Velocity of Volcaniclastic Dust. *Journal of Geophysical Research: Amospheres*, *125*, 1–22. https://doi.org/10.1029/2020JD032660

Ruz, Marie-Helene and Michel Allard. "Sedimentary Structures of Cold-Climate Coastal Dunes, Eastern Hudson Bay, Canada." Sedimentology, vol. 42, no. 5, 1995, pp. 725-34.

Selby, M. J., Rains, R. B., & Palmer, R. W. (1974). Eolian deposits of the ice-free victoria valley, southern victoria land, antarctica. *New Zealand Journal of Geology and Geophysics*, *17*(3), 543–562. https://doi.org/10.1080/00288306.1973.10421580

Shao, Y, Raupach, M. R., & Findlater, P. A. (1993). Effect of saltation bombardment on the entrainment of dust by wind. *Journal of Geophysical Research*, *98*, 12719–12726.

Shao, Yaping. (2008). Physics and Modelling of Wind Erosion. In *Atmospheric and Oceanographic Sciences Library* (2nd ed.). Springer.

Smith, D. G. "Saskatchewan's Sand Dunes:A Touch of Araby." Canadian Geographic, vol. 100, no. 5, 1980, pp. 24-29.

Stallard, R. F. (2016). Society for Conservation Biology Possible Environmental Factors Underlying Amphibian Decline in Eastern Puerto Rico: Analysis of U.S. Government Data Archives. *Conservation Biology*, *15*(4), 943–953.

Stout, J. E. (2003). Seasonal variations of saltation activity on a high plains saline playa: Yellow lake, Texas. *Physical Geography*, *24*(1), 61–76. https://doi.org/10.2747/0272-3646.24.1.61

Szczuciński, W., Zajaczkowski, M., & Scholten, J. (2009). Sediment accumulation rates in subpolar fjords - Impact of post-Little Ice Age glaciers retreat, Billefjorden, Svalbard. *Estuarine, Coastal and Shelf Science*, *85*(3), 345–356. https://doi.org/10.1016/j.ecss.2009.08.021

Thorn, C. E. and R. G. Darmody. "Grain-Size Distribution of the Insoluble Component of

Contemporary Eolian Deposits in the Alpine Zone, Front Range, Colorado, U.S.A." Arctic and Alpine Research, vol. 17, no. 4, 1985, pp. 433-42.

Tsuchiya, Y. (1969). Mechanics of the Successive Saltation of a Sand Particle on a Granular Bed in a Turbulent Stream. *Bulletin of the Disaster Prevention Research Institute*, *19*(1), 31–44.

Watkinson, A. D., Virgl, J., Miller, V. S., Naeth, M. A., Kim, J., Serben, K., Shapka, C., & Sinclair, S. (2021). Effects of dust deposition from diamond mining on subarctic plant communities and barren-ground caribou forage. *Journal of Environmental Quality*, *50*(4), 990–1003. https://doi.org/10.1002/jeq2.20251

White, H. P., Chen, W., & Leblanc, S. G. (2022). Satellite observations for detection of dust from mining activities in a caribou habitat, Northwest Territories and Nunavut. *Geomatics Canada*, *Open File*. https://doi.org/10.4095/330548

Xiao, Z., Lai, Y., & Zhang, J. (2020). A thermodynamic model for calculating the unfrozen water content of frozen soil. *Cold Regions Science and Technology*, *172*, 103011. https://doi.org/10.1016/j.coldregions.2020.103011

Xie, Shengbo et al. "Wind Dynamic Environment and Wind Tunnel Simulation Experiment of Bridge Sand Damage in Xierong Section of Lhasa-Linzhi Railway." Sustainability (Basel, Switzerland), vol. 12, no. 14, 2020, p. 5689, doi:10.3390/su12145689.

Yang, X., He, Q., Mamtimin, A., Huo, W., & Liu, X. (2013). Diurnal variations of saltation activity at Tazhong: The hinterland of Taklimakan Desert. *Meteorology and Atmospheric Physics*, *119*, 177–185. https://doi.org/10.1007/s00703-012-0227-3

Yang, X., He, Q., Matimin, A., Yang, F., Huo, W., Liu, X., Zhao, T., & Shen, S. (2017). Threshold Velocity for Saltation Activity in the Taklimakan Desert. *Pure and Applied Geophysics*, *174*, 4459–4470. https://doi.org/10.1007/s00024-017-1644-5

Zhang, Kecun et al. "Wind Energy Environments and Aeolian Sand Characteristics Along the Qinghai–Tibet Railway, China." Sedimentary geology, vol. 273-274, 2012, pp. 91-96, doi:10.1016/j.sedgeo.2012.07.003.

Appendices

Appendix A

a)

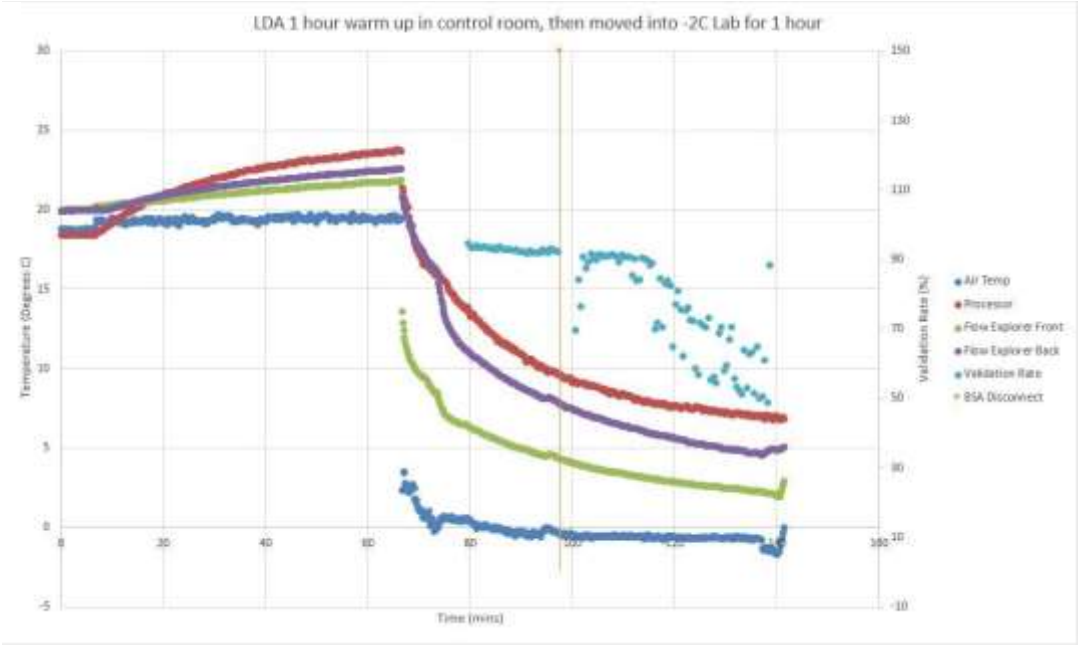

b)

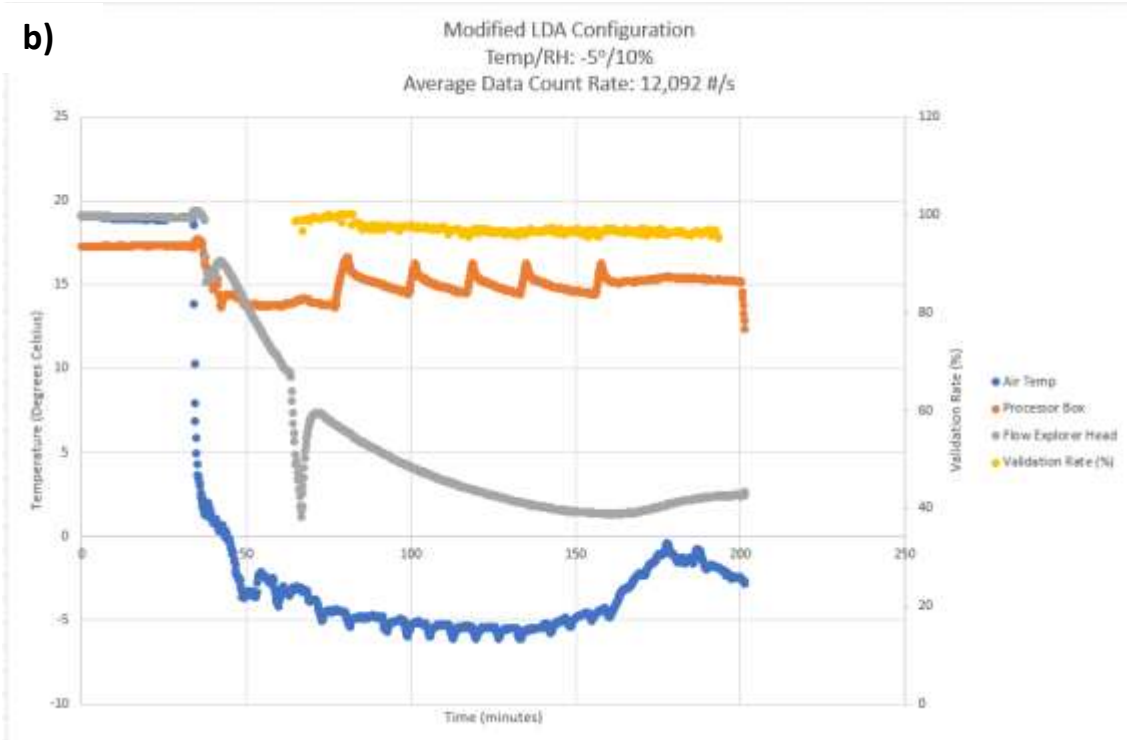

Figure 6.1: a) Temperature measured at 4 locations on the BSA flow processor during the first test run, pre-modification. The processor and the laser was turned on and left running for one hour in the control room, to warm up. After one hour, the LDA was placed in front of the wind tunnel and measured particle velocities for as long as possible. The validation rate is plotted as an indicator of the processor's performance as the temperature decreases. The processor disconnected and stopped measuring at 97 minutes and was reconnected, and the measurement recommenced. After the disconnection, the validation rate begins to drop with decreasing temperature.
b) The LDA was then reconfigured and fitted with a heater attached to the unit in which the processor is stored. To test this configuration, the LDA was allowed to warm up as in a) but only for approximately 30 mins. During the measurement period of this test, the heater maintained the processor's temperature at 15^{o}C ± 1^{o}C. The result is a validation rate near 100% and there was no disconnect at any point during the test run. This result suggests that the processor is sensitive to temperature and its performance decreases at temperatures around 7^{o}C.

Appendix B

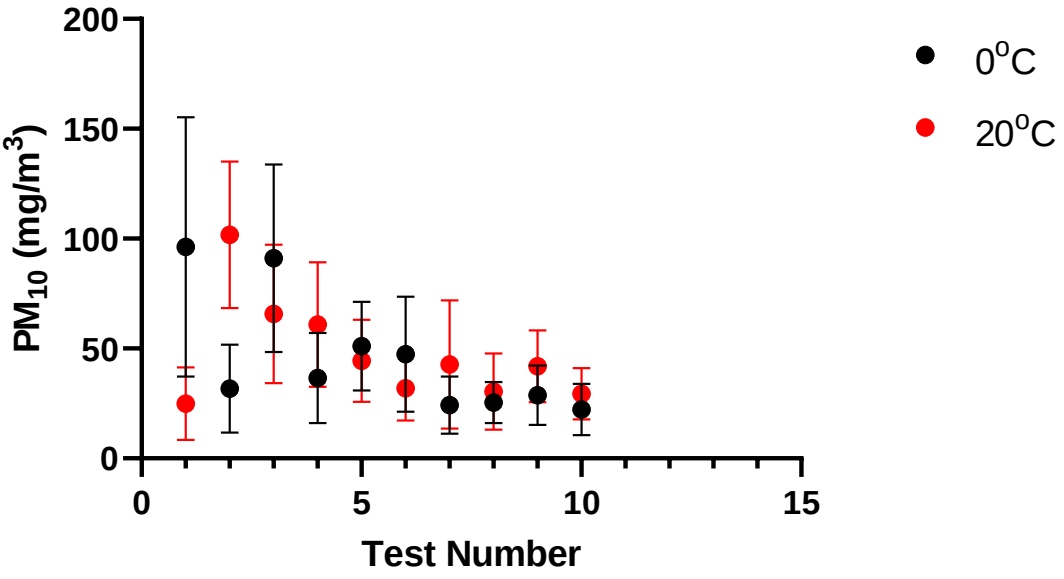

Figure 6.2: 10 tests were completed at each temperature using 0.5 g of dust, the average concentration from the 60 s sampling period is plotted with error bars. The concentrations are not statistically different with a p-value of 0.655. This suggests that the reliability of the DustTrak data is not compromised by low temperatures.

Appendix C

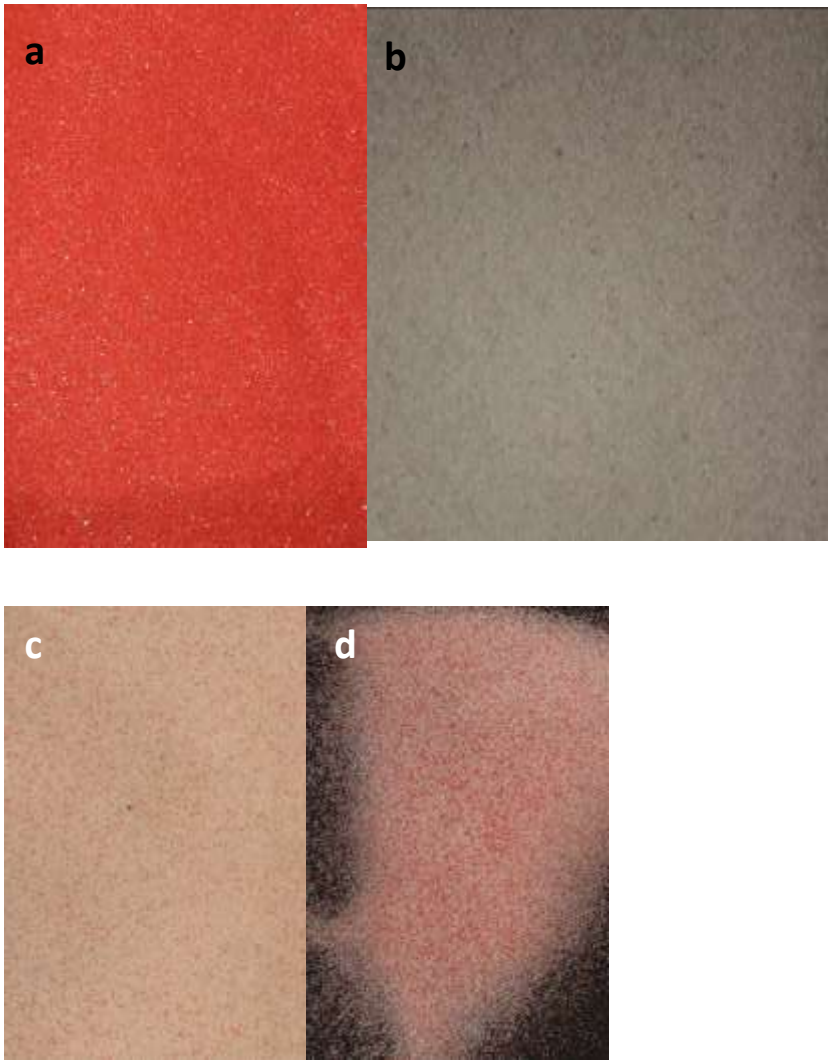

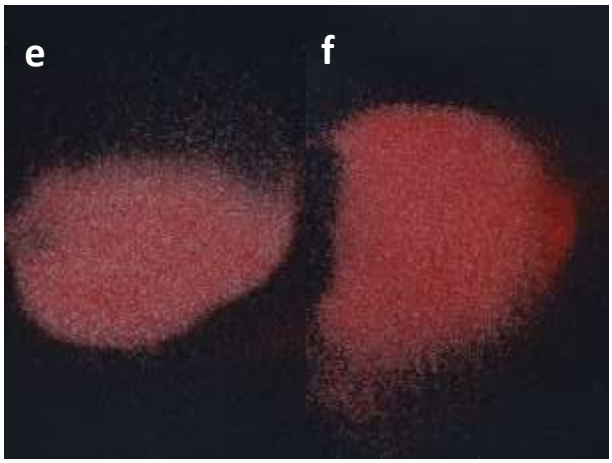

Figure 6.3: Images a and b were used in the calibration of the code to determine the Erosivity Index. 10 pixels were sampled from Image A and C and the RGB values were recorded for each pixel and subsequently averaged. Values within 2 standard deviations of the average were selected by the program.
Images c, d, e, and f are sample pictures of the sand trap contents during the 0ºC run at 8 ms^{-1} for the dry, low, medium, and high moisture content respectively. There is a visible increase in the proportion of red to white particles with an increase in the bed moisture content.

Appendix D

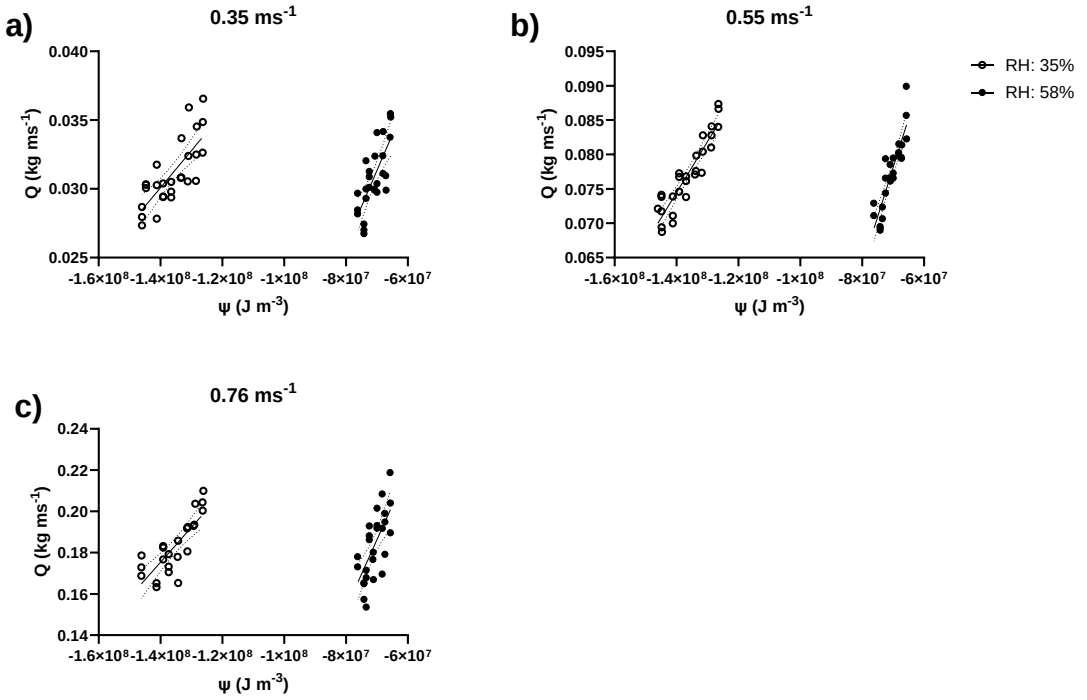

This figure from Experiment 1 plots saltation rate (Q) against the matric potential. There is no difference between the mean saltation rate for the high matric potential runs versus the low matric potential runs.

Appendix E

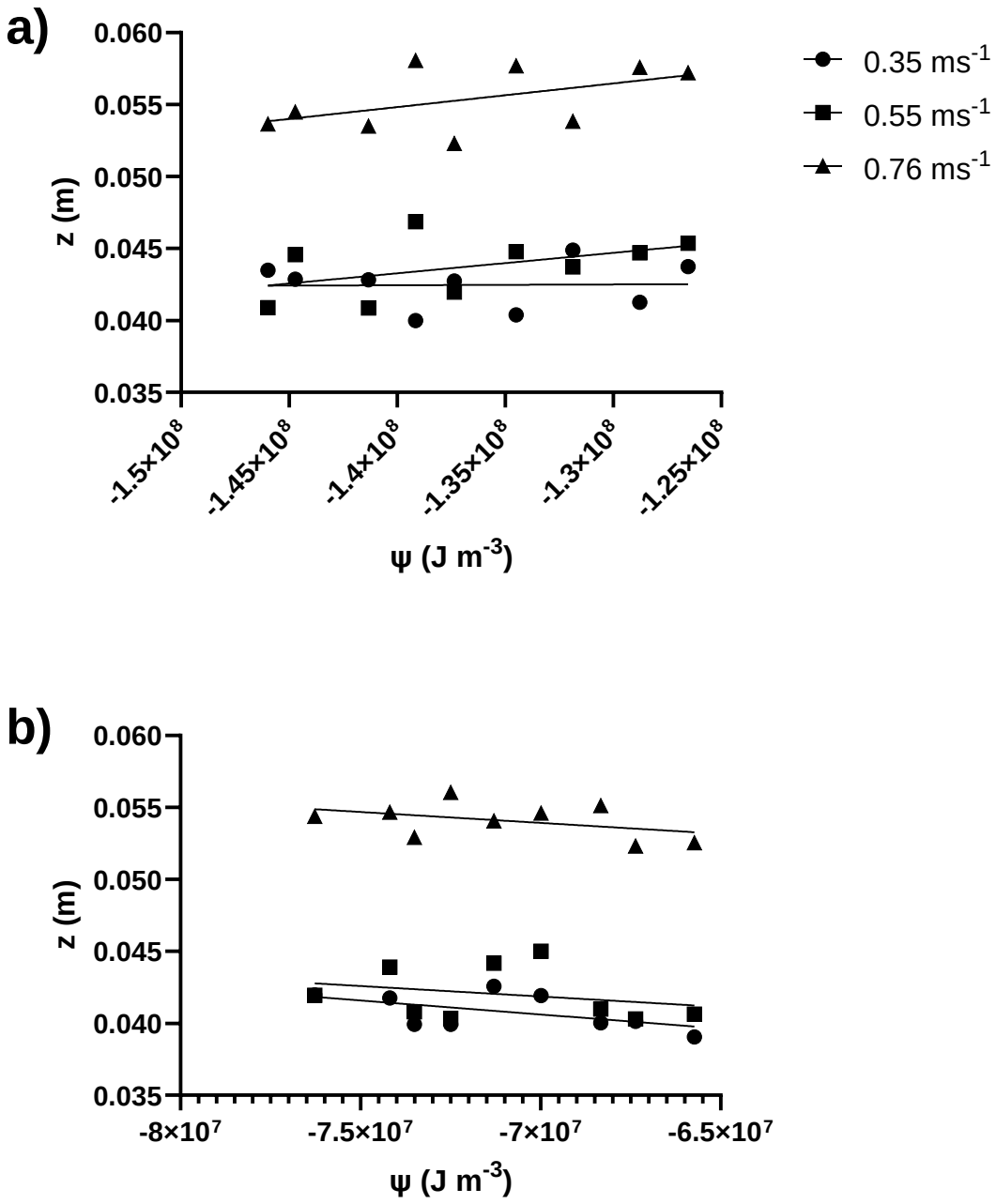

Saltation cloud height is plotted against matric potential showing that there is no strong relationship between saltation cloud height and humidity.

Appendix F

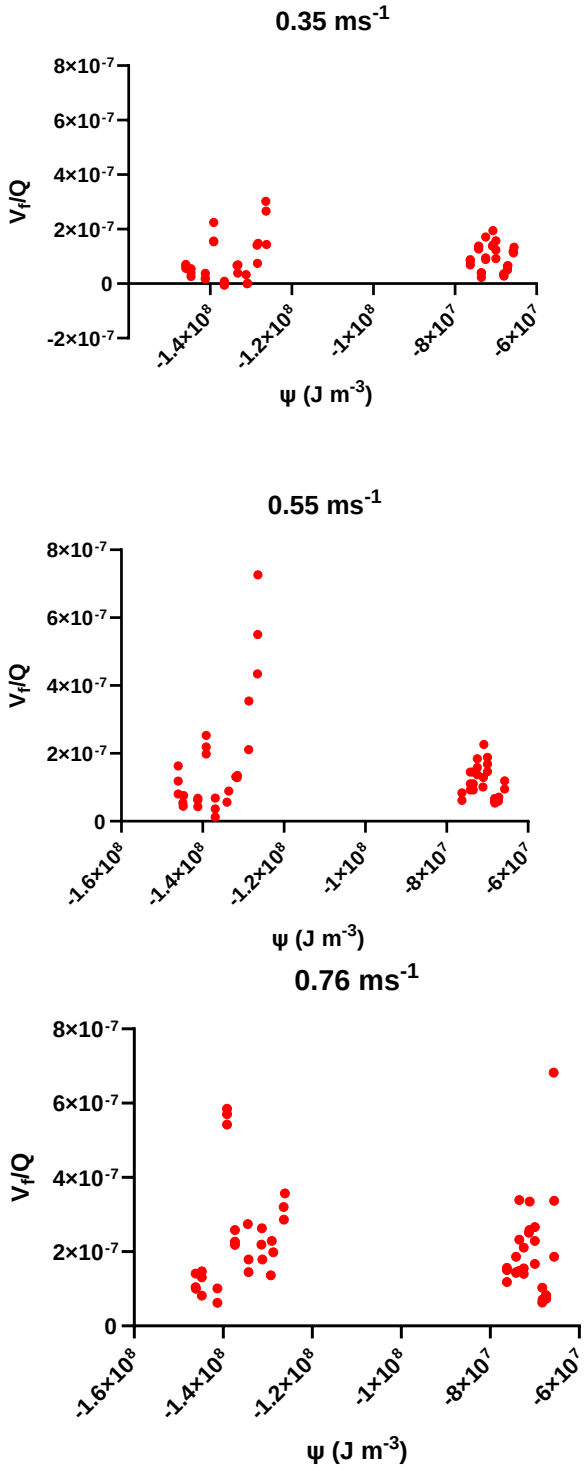
0.35 ms-1
8×10-7
6×10-7
4×10-7
2×10-7
0
-2×10-7
Vf/Q
-1.4×10^8
-1.2×10^8
-1×10^8
-8×10^7
-6×10^7
ψ (J m-3)
0.55 ms-1
8×10-7
6×10-7
4×10-7
2×10-7
0
Vf/Q
-1.6×10^8
-1.4×10^8
-1.2×10^8
-1×10^8
-8×10^7
-6×10^7
ψ (J m-3)
0.76 ms-1
8×10-7
6×10-7
4×10-7
2×10-7
0
Vf/Q
-1.6×10^8
-1.4×10^8
-1.2×10^8
-1×10^8
-8×10^7
-6×10^7
ψ (J m-3)

Appendix G

This section provides the ANOVA Summary and the multiple comparison test for all the runs completed at 0.21 ms^{-1}. There is no significant difference between saltation intensity across the 8ºC temperature range at the same moisture content.

ANOVA summary					
F	70.29				
P value	<0.0001				
P value summary	****				
Significant diff. among means (P < 0.05)?	Yes				
R squared	0.9555				
Brown-Forsythe test					
F (DFn, DFd)	1.979 (11, 36)				
P value	0.0609				
P value summary	ns				
Are SDs significantly different (P < 0.05)?	No				
Bartlett's test					
Bartlett's statistic (corrected)	27.34				
P value	0.0041				
P value summary	**				
Are SDs significantly different (P < 0.05)?	Yes				
ANOVA table	SS	DF	MS	F (DFn, DFd)	P value
Treatment (between columns)	0.4956	11	0.04506	F (11, 36) = 70.29	P<0.0001
Residual (within columns)	0.02308	36	0.0006410		
Total	0.5187	47			
Data summary					
Number of treatments (columns)	12				
Number of values (total)	48				

Number of families	1		
Number of comparisons per family	66		
Alpha	0.05		
Tukey's multiple comparisons test	**Mean Diff.**	**95.00% CI**	**Adjusted P Value**
5dry6 vs. 5low6	0.2039	0.1414 to 0.2664	<0.0001
5dry6 vs. 5medium6	0.1975	0.1350 to 0.2600	<0.0001
5dry6 vs. 5high6	0.2135	0.1510 to 0.2760	<0.0001
5dry6 vs. 0dry6	-0.03000	-0.09249 to 0.03248	0.8673
5dry6 vs. 0low6	0.1992	0.1367 to 0.2616	<0.0001
5dry6 vs. 0medium6	0.2071	0.1447 to 0.2696	<0.0001
5dry6 vs. 0high6	0.2142	0.1517 to 0.2766	<0.0001
5dry6 vs. -5dry6	-0.05413	-0.1166 to 0.008360	0.1431
5dry6 vs. -5low6	0.2042	0.1417 to 0.2666	<0.0001
5dry6 vs. -5medium6	0.2017	0.1392 to 0.2641	<0.0001
5dry6 vs. -5high6	0.2036	0.1411 to 0.2661	<0.0001
5low6 vs. 5medium6	-0.006429	-0.06891 to 0.05606	>0.9999
5low6 vs. 5high6	0.009573	-0.05291 to 0.07206	>0.9999
5low6 vs. 0dry6	-0.2339	-0.2964 to -0.1714	<0.0001
5low6 vs. 0low6	-0.004754	-0.06724 to 0.05773	>0.9999
5low6 vs. 0medium6	0.003222	-0.05926 to 0.06571	>0.9999
5low6 vs. 0high6	0.01025	-0.05224 to 0.07273	>0.9999
5low6 vs. -5dry6	-0.2580	-0.3205 to -0.1956	<0.0001
5low6 vs. -5low6	0.0002463	-0.06224 to 0.06273	>0.9999
5low6 vs. -5medium6	-0.002254	-0.06474 to 0.06023	>0.9999
5low6 vs. -5high6	-0.0003473	-0.06283 to 0.06214	>0.9999
5medium6 vs. 5high6	0.01600	-0.04648 to 0.07849	0.9988
5medium6 vs. 0dry6	-0.2275	-0.2900 to -0.1650	<0.0001
5medium6 vs. 0low6	0.001675	-0.06081 to 0.06416	>0.9999
5medium6 vs. 0medium6	0.009651	-0.05283 to 0.07214	>0.9999
5medium6 vs. 0high6	0.01668	-0.04581 to 0.07916	0.9982
5medium6 vs. -5dry6	-0.2516	-0.3141 to -0.1891	<0.0001
5medium6 vs. -5low6	0.006675	-0.05581 to 0.06916	>0.9999
5medium6 vs. -5medium6	0.004175	-0.05831 to 0.06666	>0.9999
5medium6 vs. -5high6	0.006081	-0.05640 to 0.06857	>0.9999
5high6 vs. 0dry6	-0.2435	-0.3060 to -0.1810	<0.0001
5high6 vs. 0low6	-0.01433	-0.07681 to 0.04816	0.9996
5high6 vs. 0medium6	-0.006351	-0.06884 to 0.05613	>0.9999
5high6 vs. 0high6	0.0006733	-0.06181 to 0.06316	>0.9999
5high6 vs. -5dry6	-0.2676	-0.3301 to -0.2051	<0.0001
5high6 vs. -5low6	-0.009327	-0.07181 to 0.05316	>0.9999
5high6 vs. -5medium6	-0.01183	-0.07431 to 0.05066	>0.9999
5high6 vs. -5high6	-0.009920	-0.07241 to 0.05256	>0.9999
0dry6 vs. 0low6	0.2292	0.1667 to 0.2916	<0.0001
0dry6 vs. 0medium6	0.2371	0.1747 to 0.2996	<0.0001
0dry6 vs. 0high6	0.2442	0.1817 to 0.3066	<0.0001
0dry6 vs. -5dry6	-0.02412	-0.08661 to 0.03836	0.9662
0dry6 vs. -5low6	0.2342	0.1717 to 0.2966	<0.0001
0dry6 vs. -5medium6	0.2317	0.1692 to 0.2941	<0.0001

0dry6 vs. -5high6	0.2336	0.1711 to 0.2961	<0.0001
0low6 vs. 0medium6	0.007976	-0.05451 to 0.07046	>0.9999
0low6 vs. 0high6	0.01500	-0.04749 to 0.07749	0.9993
0low6 vs. -5dry6	-0.2533	-0.3158 to -0.1908	<0.0001
0low6 vs. -5low6	0.005000	-0.05749 to 0.06749	>0.9999
0low6 vs. -5medium6	0.002500	-0.05999 to 0.06499	>0.9999
0low6 vs. -5high6	0.004406	-0.05808 to 0.06689	>0.9999
0medium6 vs. 0high6	0.007025	-0.05546 to 0.06951	>0.9999
0medium6 vs. -5dry6	-0.2613	-0.3237 to -0.1988	<0.0001
0medium6 vs. -5low6	-0.002976	-0.06546 to 0.05951	>0.9999
0medium6 vs. -5medium6	-0.005476	-0.06796 to 0.05701	>0.9999
0medium6 vs. -5high6	-0.003569	-0.06605 to 0.05892	>0.9999
0high6 vs. -5dry6	-0.2683	-0.3308 to -0.2058	<0.0001
0high6 vs. -5low6	-0.01000	-0.07249 to 0.05249	>0.9999
0high6 vs. -5medium6	-0.01250	-0.07499 to 0.04999	0.9999
0high6 vs. -5high6	-0.01059	-0.07308 to 0.05189	>0.9999
-5dry6 vs. -5low6	0.2583	0.1958 to 0.3208	<0.0001
-5dry6 vs. -5medium6	0.2558	0.1933 to 0.3183	<0.0001
-5dry6 vs. -5high6	0.2577	0.1952 to 0.3202	<0.0001
-5low6 vs. -5medium6	-0.002500	-0.06499 to 0.05999	>0.9999
-5low6 vs. -5high6	-0.0005936	-0.06308 to 0.06189	>0.9999
-5medium6 vs. -5high6	0.001906	-0.06058 to 0.06439	>0.9999

Appendix H

This section provides the ANOVA Summary and the multiple comparison test for all the runs completed at 0.21 ms^{-1} for velocities of particles measured at 40 mm above the bed surface.

ANOVA summary					
F	656.1				
P value	<0.0001				
P value summary	****				
Significant diff. among means (P < 0.05)?	Yes				
R squared	0.6123				
Brown-Forsythe test					
F (DFn, DFd)	18.52 (11, 4570)				
P value	<0.0001				
P value summary	****				
Are SDs significantly different (P < 0.05)?	Yes				
Bartlett's test					
Bartlett's statistic (corrected)	403.1				
P value	<0.0001				
P value summary	****				
Are SDs significantly different (P < 0.05)?	Yes				
ANOVA table	SS	DF	MS	F (DFn, DFd)	P value
Treatment (between columns)	7204	11	654.9	F (11, 4570) = 656.1	P<0.0001
Residual (within columns)	4562	4570	0.9983		
Total	11766	4581			
Data summary					
Number of treatments (columns)	12				
Number of values (total)	4582				

Number of families	1		
Number of comparisons per family	66		
Alpha	0.05		
Tukey's multiple comparisons test	**Mean Diff.**	**95.00% CI of diff.**	**Adjusted P Value**
5dry40 vs. 5low40	-3.080	-3.854 to -2.306	<0.0001
5dry40 vs. 5medium40	-2.822	-3.080 to -2.564	<0.0001
5dry40 vs. 5high40	-2.723	-2.941 to -2.505	<0.0001
5dry40 vs. 0dry40	-2.108	-2.395 to -1.822	<0.0001
5dry40 vs. 0low40	-2.451	-2.627 to -2.274	<0.0001
5dry40 vs. 0medium40	-2.508	-2.708 to -2.309	<0.0001
5dry40 vs. 0high40	-2.703	-2.896 to -2.510	<0.0001
5dry40 vs. n5dry40	-1.674	-1.964 to -1.383	<0.0001
5dry40 vs. n5low40	-2.533	-2.728 to -2.337	<0.0001
5dry40 vs. n5medium40	-2.601	-2.805 to -2.397	<0.0001
5dry40 vs. n5high40	-2.705	-2.890 to -2.520	<0.0001
5low40 vs. 5medium40	0.2579	-0.5505 to 1.066	0.9967
5low40 vs. 5high40	0.3569	-0.4396 to 1.153	0.9498
5low40 vs. 0dry40	0.9716	0.1536 to 1.790	0.0059
5low40 vs. 0low40	0.6293	-0.1569 to 1.415	0.2701
5low40 vs. 0medium40	0.5718	-0.2199 to 1.363	0.4328
5low40 vs. 0high40	0.3771	-0.4129 to 1.167	0.9229
5low40 vs. n5dry40	1.406	0.5870 to 2.226	<0.0001
5low40 vs. n5low40	0.5473	-0.2434 to 1.338	0.5033
5low40 vs. n5medium40	0.4792	-0.3135 to 1.272	0.7096
5low40 vs. n5high40	0.3752	-0.4130 to 1.163	0.9243
5medium40 vs. 5high40	0.09900	-0.2206 to 0.4186	0.9975
5medium40 vs. 0dry40	0.7137	0.3437 to 1.084	<0.0001
5medium40 vs. 0low40	0.3714	0.07843 to 0.6643	0.0020
5medium40 vs. 0medium40	0.3138	0.006575 to 0.6211	0.0402
5medium40 vs. 0high40	0.1192	-0.1837 to 0.4221	0.9809
5medium40 vs. n5dry40	1.149	0.7755 to 1.522	<0.0001
5medium40 vs. n5low40	0.2894	-0.01538 to 0.5942	0.0814
5medium40 vs. n5medium40	0.2213	-0.08873 to 0.5313	0.4524
5medium40 vs. n5high40	0.1173	-0.1808 to 0.4154	0.9809
5high40 vs. 0dry40	0.6147	0.2715 to 0.9578	<0.0001
5high40 vs. 0low40	0.2724	0.01410 to 0.5306	0.0282
5high40 vs. 0medium40	0.2148	-0.05957 to 0.4893	0.3031
5high40 vs. 0high40	0.02020	-0.2493 to 0.2897	>0.9999
5high40 vs. n5dry40	1.050	0.7031 to 1.396	<0.0001
5high40 vs. n5low40	0.1904	-0.08123 to 0.4620	0.4825

5high40 vs. n5medium40	0.1223	-0.1552 to 0.3997	0.9554
5high40 vs. n5high40	0.01827	-0.2459 to 0.2824	>0.9999
0dry40 vs. 0low40	-0.3423	-0.6607 to -0.02387	0.0226
0dry40 vs. 0medium40	-0.3998	-0.7315 to -0.06816	0.0047
0dry40 vs. 0high40	-0.5945	-0.9221 to -0.2668	<0.0001
0dry40 vs. n5dry40	0.4348	0.04151 to 0.8282	0.0159
0dry40 vs. n5low40	-0.4243	-0.7536 to -0.09493	0.0015
0dry40 vs. n5medium40	-0.4924	-0.8266 to -0.1582	<0.0001
0dry40 vs. n5high40	-0.5964	-0.9196 to -0.2732	<0.0001
0low40 vs. 0medium40	-0.05752	-0.3003 to 0.1853	0.9998
0low40 vs. 0high40	-0.2522	-0.4894 to -0.01492	0.0258
0low40 vs. n5dry40	0.7772	0.4552 to 1.099	<0.0001
0low40 vs. n5low40	-0.08198	-0.3216 to 0.1576	0.9939
0low40 vs. n5medium40	-0.1501	-0.3963 to 0.09613	0.6983
0low40 vs. n5high40	-0.2541	-0.4852 to -0.02300	0.0171
0medium40 vs. 0high40	-0.1946	-0.4494 to 0.06009	0.3410
0medium40 vs. n5dry40	0.8347	0.4996 to 1.170	<0.0001
0medium40 vs. n5low40	-0.02446	-0.2814 to 0.2325	>0.9999
0medium40 vs. n5medium40	-0.09258	-0.3557 to 0.1705	0.9923
0medium40 vs. n5high40	-0.1966	-0.4456 to 0.05245	0.2907
0high40 vs. n5dry40	1.029	0.6983 to 1.360	<0.0001
0high40 vs. n5low40	0.1702	-0.08153 to 0.4219	0.5418
0high40 vs. n5medium40	0.1021	-0.1560 to 0.3601	0.9801
0high40 vs. n5high40	-0.001927	-0.2455 to 0.2417	>0.9999
n5dry40 vs. n5low40	-0.8591	-1.192 to -0.5264	<0.0001
n5dry40 vs. n5medium40	-0.9273	-1.265 to -0.5897	<0.0001
n5dry40 vs. n5high40	-1.031	-1.358 to -0.7046	<0.0001
n5low40 vs. n5medium40	-0.06812	-0.3283 to 0.1921	0.9995
n5low40 vs. n5high40	-0.1721	-0.4180 to 0.07381	0.4850
n5medium40 vs. n5high40	-0.1040	-0.3564 to 0.1484	0.9728

Appendix I

This section provides the ANOVA Summary and the multiple comparison test for the coefficient of restitution data. All the data is binned by moisture content.

ANOVA summary					
F	56.83				
P value	<0.0001				
P value summary	****				
Significant diff. among means (P < 0.05)?	Yes				
R squared	0.7949				
Brown-Forsythe test					
F (DFn, DFd)	2.296 (3, 44)				
P value	0.0909				
P value summary	ns				
Are SDs significantly different (P < 0.05)?	No				
Bartlett's test					
Bartlett's statistic (corrected)	4.194				
P value	0.2413				
P value summary	ns				
Are SDs significantly different (P < 0.05)?	No				
ANOVA table	SS	DF	MS	F (DFn, DFd)	P value
Treatment (between columns)	0.2401	3	0.08003	F (3, 44) = 56.83	P<0.0001
Residual (within columns)	0.06196	44	0.001408		
Total	0.3020	47			
Data summary					
Number of treatments (columns)	4				
Number of values (total)	48				

Number of families	1		
Number of comparisons per family	6		
Alpha	0.05		
Tukey's multiple comparisons test	**Mean Diff.**	**95.00% CI of diff.**	**Adjusted P Value**
dry vs. low	-0.1483	-0.1892 to -0.1074	<0.0001
dry vs. medium	-0.1575	-0.1984 to -0.1166	<0.0001
dry vs. high	-0.1783	-0.2192 to -0.1374	<0.0001
low vs. medium	-0.009167	-0.05007 to 0.03174	0.9320
low vs. high	-0.03000	-0.07090 to 0.01090	0.2194
medium vs. high	-0.02083	-0.06174 to 0.02007	0.5307